Development of Scanning Electrochemical Microscopy for the Investigation of Photocatalysis at Semiconductor Surfaces

Sofia Margarida Martins Costa da Fonseca

A thesis submitted for the degree of
Doctor of Philosophy

University of Warwick
Department of Chemistry

September 2002

To my family,

I could not have done this without your continual love, support and encouragement.

Contents

Acknowledgements

I would like to thank Prof. Patrick Unwin and Prof. Terence Kemp for their supervision and continuous encouragement during the course of my studies at Warwick. Especially, without the enthusiasm and support of Prof. Patrick Unwin this work would not have been possible. I would also like to thank Dr. Anna Barker who has written the computer models, Dr. Julie Macpherson for her help and advice on microelectrodes preparation, Dr. Lou Gonsalves for showing me how to do the interferometry measurements and Dr. Samina Ahmed for her help in some initial actinometry experiments. Thanks must also go to everybody in the Electrochemistry and Interfaces group at Warwick for their friendship throughout my time in the group.

Additional thanks must go to M. Grant, L. Butcher and K. Westwood of mechanical workshops and P. Roskelly and K. Harris of electronic workshops for all their skilled and professional work.

I am eternally grateful to my parents and sister for all their love, support and encouragement during the past years. I am sure I could not have done this without our daily phone calls!

Finally, I would like to acknowledge the financial support from the Portuguese Government through a scholarship from Fundação para a Ciência e Tecnologia.

Declaration

I declare that the work contained in this thesis is entirely original and my own work, except where otherwise indicated.

The computer models presented in this thesis were written by Dr. Anna Barker. The experiments in chapter 6 were conducted in collaboration with Craig Wood as part of his MChem project at the University of Warwick.

Abstract

This thesis is concerned with the development and application of scanning electrochemical microscopy (SECM) to investigate interfacial photoelectrochemical processes occurring at supported TiO_2 surfaces. The new SECM approach, involving both amperometric and potentiometric electrodes, was used to monitor interfacial photoprocesses with high spatial resolution.

A new *in situ* photoelectrochemical approach to chemical actinometry has been developed and used to determine the light flux through a quartz fibre employed in the SECM system. In this system an ultramicroelectrode (UME) probe is positioned with high precision at a known distance close to a TiO_2-coated fibre and used to detect reactants or products of the ongoing photodegradation process. The microelectrochemical actinometry approach was developed using the well-known liquid phase potassium ferrioxalate actinometer. The approach involved recording the steady-state current for Fe(III) reduction at an SECM tip positioned close to the fibre. A step function in the light flux (off-on) was then applied and the resulting chronoamperometric behaviour due to the reduction of Fe(III) at the UME was recorded as a function of tip-fibre separation distance. A theoretical model has been developed to simulate experimental current-time profiles, which allowed the light flux through the quartz fibre to be quantified.

An experimental approach to investigating the photoelectrochemical reduction of oxygen at UV-illuminated TiO_2 surfaces, in aqueous aerated and oxygenated electrolyte solutions, in the absence and presence of hole scavengers, has been developed. In this new approach the chronoamperometric behaviour for oxygen reduction was recorded at an UME tip after stepping the light flux at a back-illuminated TiO_2 film on and off. The kinetics of the reduction process were interpreted through various theoretical models proposed in the literature. This experimental approach demonstrated a significant depletion of the oxygen concentration at the illuminated TiO_2 surface, which provides a new insight into the photomineralisation process, showing the important role of oxygen in controlling the kinetics.

Using an SECM potentiometric approach, the photomineralisation kinetics of a model organic pollutant, 4-chlorophenol (4-CP), in aerated and oxygenated aqueous solutions at supported TiO_2 films, were quantitatively investigated. A potentiometric Ag/AgCl UME, positioned at a known distance above the TiO_2 film, was used to monitor directly the Cl^- production from the photomineralisation of 4-CP. A theoretical model, employing a Langmuir-Hinshelwood type kinetic equation, has been developed to interpret the kinetics of the photomineralisation process and determine the associated quantum efficiency. A direct correlation between oxygen consumption at the illuminated TiO_2 surface and Cl^- formation in the photomineralisation process has been found.

SECM has also been used to monitor photoelectrochemical transfer kinetics at the TiO_2/aqueous interface using a well-known electron scavenger, methyl viologen. The TiO_2 film was in contact with a solution containing methyl viologen dication (MV^{2+}) as the redox mediator and sodium acetate as the hole scavenger. The chronoamperometric behaviour for MV^{2+} reduction was recorded at an UME tip after stepping the light flux at the TiO_2 film from off to on. The rate constants for the reduction process were obtained through a theoretical model based on zero-order kinetics. The substrate generation/ tip collection mode of the SECM was also used to detect the $MV^{\bullet+}$ radical cation produced at the TiO_2 surface at the UME tip.

List of Abbreviations

ADIFDM	Alternating direction implicit finite-difference method
AgQRE	Silver quasi-reference electrode
CdS	Cadmium sulfide
CFMED	Channel flow method with electrochemical detection
4-CP	4-chlorophenol
G/ C	Generation/ collection
GC	Gas chromatography
HPLC	High performance liquid chromatography
ITO	Indium-tin oxide
L-H	Langmuir-Hinshelwood
MV^{2+}	Methyl Viologen
$MV^{\bullet+}$	Methyl Viologen radical cation
Ox	Oxidised form of a redox couple
PEM	Photoelectrochemical microscopy
Red	Reduced form of a redox couple
RG	Insulator radius to electrode radius ratio
SCE	Saturated calomel electrode
SECM	Scanning Electrochemical Microscopy
SG/ TC	Substrate generation/ tip collection
SPECM	Scanning photoelectrochemical and electrochemical microscopy
TEOA	Triethanolamine
TG/ SC	Tip generation/ substrate collection
UME	Ultramicroelectrode
UV	Ultra-violet

List of Symbols

ϕ	Quantum yield
k_{CT}	Charge transfer process rate
k_R	Electron-hole recombination rate
n_s	Concentration of electrons at the semiconductor surface
n_p	Concentration of holes at the semiconductor surface
e^-	Electron
h^+	Hole
r_i	Initial disappearance rate of substrate S
$[S]_i$	Initial concentration of substrate S
k_S	Proportionality constant
K_S	Equilibrium adsorption constant of S on TiO_2
K_{O2}	Equilibrium adsorption constant of O_2 on TiO_2
I_0	Light intensity
θ_{O2}	Fraction of adsorbed sites covered by O_2
γ	Proportionality constant
r_g	Insulator radius
a	Radius of the UME
d	Tip-substrate separation distance
$i(\infty)$	Steady-state limiting current
F	Faraday's constant
D	Diffusion coefficient of a species
c^*	Bulk concentration of a species
n	Number of electrons transferred in a redox reaction
L	Normalised tip-substrate distance (d/a)
ε	Molar extinction coefficient
r	Radial co-ordinate in the axisymmetric cylindrical SECM geometry
z	Normal co-ordinate in the axisymmetric cylindrical SECM geometry
A	Absorbance
l	Path length of the spectrophotometric cell
K	Normalised rate constant
Γ_0	Flux of electrons and holes created by the absorption of light by TiO_2

Ω	Surface density of adsorbed oxygen
k_{zero}	Zero-order rate constant for the reduction of O_2
k_{half}	Half-order rate constant for the reduction of O_2
k_{lh}	Langmuir-Hinshelwood rate constant for the reduction of O_2
τ	Normalised time (tD/a^2)
j	Rate of oxygen reduction
NE	Number of grid points in the radial direction over the electrode
NG	Number of grid points in the radial direction over the glass sheath
NZ	Number of grid points in the normal direction
N	Density of sites at the TiO_2 surface
N_A	Avogadro's number
E_F	Fermi energy level of TiO_2
E_{redox}	Redox potential of a species

CHAPTER 1

INTRODUCTION

This chapter provides an overview of the properties of semiconductors as photocatatalysts and reviews the current status on the primary processes and kinetics of the TiO_2-sensitised photomineralisation of organic pollutants. The basic principles of scanning electrochemical microscopy (SECM) are described and an overview of SECM as a probe of surface photochemical processes is given. The aim of this thesis was to use SECM to obtain a more detailed understanding of the photoelectrochemical reactions occurring at a semiconductor surface.

1.1 Semiconductor Photocatalysis

Heterogeneous photoassisted catalysis, known as 'photocatalysis', is defined as the 'acceleration of a photoreaction by the presence of a catalyst'.[1] The use of semiconductors as photocatalysts for a variety of processes, such as environmental protection and amelioration, has been and continues to be an active field of research.[2,3,4,5,6] Semiconductor photocatalysis has a broad range of emerging potential applications for the treatment of water (contaminant destruction and removal, metal deposition and recovery, sterilisation and disinfection) and air (purification, decontamination, deodorisation, self-cleaning surfaces). Commercial products based on these processes have already entered the market.[7,8,9,10]

1.1.1 Band Gap Photoexcitation of Semiconductors

The electronic structure of a semiconductor can be described by the band theory model, in which the highest occupied band (the valence band) and the lowest unoccupied energy band (the conduction band) are separated by a band gap E_{bg}, a region devoid of energy levels in a perfect crystal.[11]

The initial process for heterogeneous photocatalysis of organic and inorganic compounds by semiconductors is the generation of electron-hole pairs in the semiconductor particles. The enlarged section of Figure 1.1 shows the excitation of an electron from the valence band to the conduction band initiated by the absorption of a photon of ultra-band gap energy, *i.e.* light is absorbed with energy equal to or greater than the band gap of the semiconductor. This leads to the generation of a hole, h^+, in the valence band and a corresponding electron, e^-, in the conduction band. The classical picture of a hole is that of a highly localised electron vacancy in the lattice of the irradiated semiconductor particle.[12] The electron, by virtue of its population of the conduction band, is much more delocalised and can be trapped at a surface defect site or by an adsorbed chemical trap.[13] Upon excitation, the fate of the separated electron and hole can follow several pathways.[11] Figure 1.1 illustrates some of the deexcitation pathways for the electrons and holes.

The electrons and holes can migrate to the semiconductor surface where they are able to undergo charge transfer reactions with adsorbed species. The electron transfer process is more efficient if the species are preadsorbed on the surface.[14] At the surface of the semiconductor, the photogenerated electrons can reduce an electron acceptor A, usually oxygen in an aerated solution (pathway C) and the photogenerated holes can oxidise an electron donor D (pathway D). The

probability and rate of the charge transfer processes for electrons and holes depend upon the respective positions of the band edges for the conduction and valence bands and the redox potential levels of the adsorbate species. This issue will be considered in section 1.1.3.

In competition with charge transfer to adsorbed species is electron and hole recombination. Recombination of the photogenerated electron-hole pair can occur in the bulk of the semiconductor (pathway B) or on the surface (pathway A) with the release of heat.

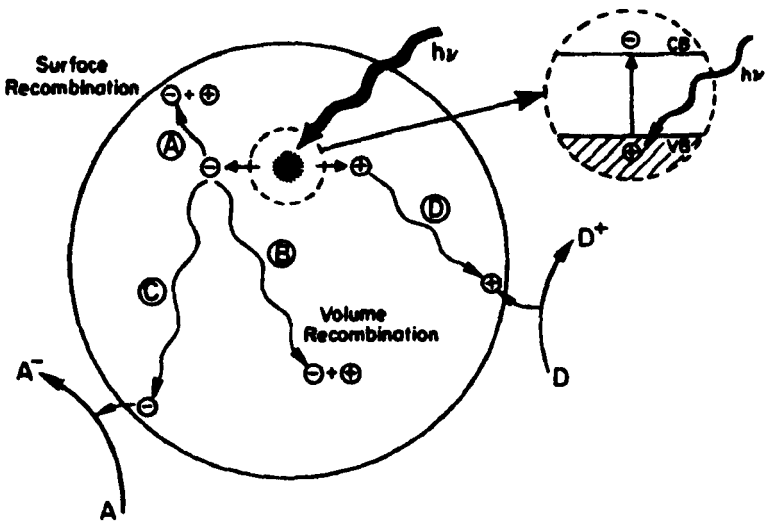

Figure 1.1 Schematic photoexcitation of a semiconductor followed by deexcitation events.[11]

1.1.2 Efficiency of Photocatalysis

The efficiency of the photocatalytic process is expressed as the quantum yield, which gives the relation between the number of molecules reacting in a given time and the number of quanta absorbed. Due to scattering of light by the semiconductor surface it is very difficult to measure the actual proportion of light absorbed. It is usually assumed that all the light is absorbed and the efficiency is quoted as an apparent quantum yield. The quantum yield for an ideal system, ϕ, is

given by a simple relationship where a combination of all the pathway probabilities for the electron and hole has been considered:

$$\phi \propto \frac{k_{CT}}{k_{CT} + k_R} \tag{1.1}$$

where ϕ is proportional to the rate of the charge transfer process (k_{CT}) and inversely proportional to the sum of the charge transfer rate (k_{CT}) and the electron-hole recombination rate (k_R) in the bulk and at the surface. It is considered that the diffusion of the products into the solution proceeds so rapidly that the reverse reaction of electrons recombining with donors and holes recombining with acceptors does not occur.

In the absence of recombination, the quantum yield would take on the ideal value of unity. In this idealised case, the rate of charge transfer would be dependent on the diffusion of charge carriers to the surface in the absence of excess surface charge. However, in a real system recombination does occur and the concentration of electrons (n_s) and holes (p_s) at the surface is not equal.[15] In order to obtain a more efficient charge transfer process, charge carrier traps are used to promote the trapping of electrons and holes at the surface of the semiconductor. For photooxidation processes on TiO_2, $n_s > p_s$, because the electron transfer to molecular oxygen trapped at defect sites is relatively slow. A decrease in the electron-hole recombination rate can be achieved by modifications made to the semiconductor surface, such as additions of metals, dopants, or combinations with other semiconductors.[11]

1.1.3 Band Edge Positions

The ability of a semiconductor to promote photoinduced electron transfer to adsorbed species at its surface is governed by the band energy positions of the

semiconductor and the redox potentials of the adsorbate.[11] Knowledge of the band positions for semiconductors is useful as it indicates the thermodynamic limitations for photoreactions that can be carried out with the charge carriers. In order to photoreduce a chemical species, the conduction band of the semiconductor must be more negative than the reduction potential of the chemical species; to photooxidise a chemical species, the potential of the valence band of the semiconductor must be more positive than the oxidation potential of the chemical species. Figure 1.2 shows the band gaps and band edges of several semiconductors at pH 0. The band edge positions of a semiconductor are influenced by the pH of the contacting solution. The band edge positions of TiO_2 are known to shift cathodically with pH (band positions change by ca. –0.059 V × ΔpH).[16,17]

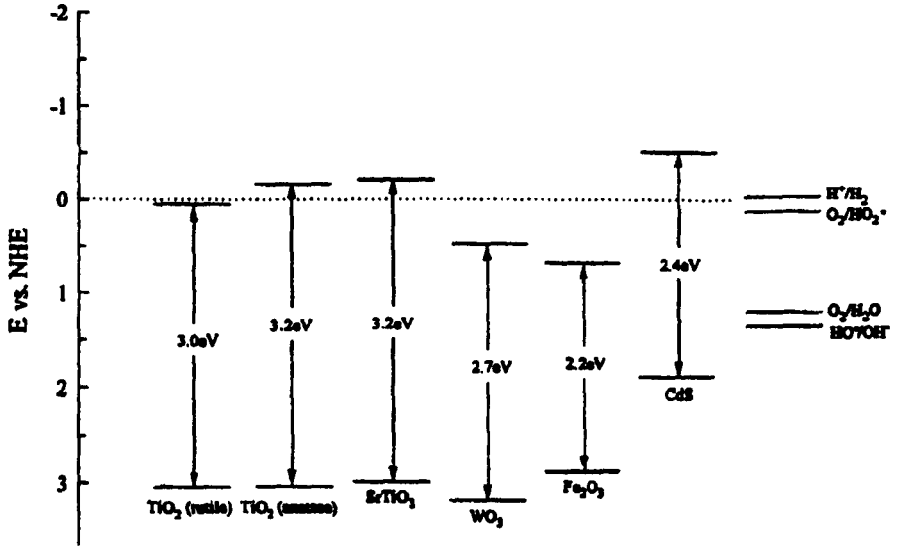

Figure 1.2 Valence and conduction band positions for various semiconductors, and useful, relevant redox couples at pH 0.[1]

Figure 1.2 shows that the redox potential of the photogenerated valence band hole of TiO_2 is positive enough to produce adsorbed $^{\bullet}OH$ radicals and

simultaneously, the redox potential of the photogenerated conduction band electron is negative enough to convert oxygen to superoxide anion ($O_2^{\bullet-}$ or its protonated form $HO_2^{\bullet}$). This gives TiO_2 the capability to photooxidise a large variety of organic pollutants, as will be considered in section 1.2.2.

1.2 Photocatalysis on TiO_2 Surfaces

Several simple oxide and sulfide semiconductors are available for photocatalysis. They include TiO_2, WO_3, $SrTiO_3$, Fe_2O_3, ZnO and ZnS. However, among these semiconductors TiO_2 has proven to be the most suitable for widespread environmental applications.[3,4,7] TiO_2 is biologically and chemically inert, it is stable with respect to photocorrosion, and it is inexpensive.[1] It is also able to completely oxidise a wide range of organic pollutants.[18]

1.2.1 TiO_2 as a Photocatalyst

TiO_2 photocatalysis has been applied to a variety of problems of environmental interest. It has been shown to be useful for the oxidation of organic[4,19,20] and inorganic[2,21] pollutants, for the destruction of microorganisms such as bacteria[22] and viruses,[23] for the inactivation of cancer cells,[24,25] for odour control,[26] for the photosplitting of water to produce hydrogen gas,[27,28,29,30] for the fixation of nitrogen,[31,32,33] and for the clean up of oil spills.[34,35,36]

Currently TiO_2 is considered the most effective semiconductor photocatalyst due to the following properties:[1,37]

i) highly photocatalytically active

ii) biologically and chemically inert

iii) photostable (*i.e.* not liable to photoanodic corrosion, for example)

iv) insoluble in aqueous solution

v) inexpensive

vi) able to oxidise completely a wide range of hazardous and toxic compounds.

TiO_2 is available in two different crystalline structures, rutile and anatase, and due to this difference in the lattice structure, different mass densities and electronic band structures are produced as shown in Figure 1.3.[11,38,39]

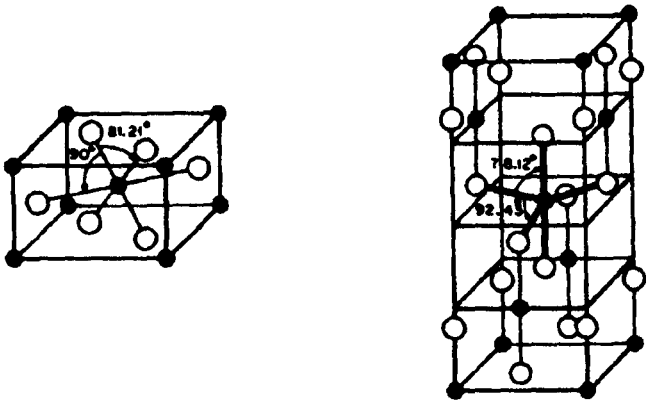

Ti — •
O — o

Rutile	Anatase
d_{Ti-Ti} = 3.57 Å	d_{Ti-Ti} = 3.79 Å
2.96 Å	3.04 Å
d_{Ti-O} = 1.949 Å	d_{Ti-O} = 1.934 Å
1.980 Å	1.980 Å
E_{bg} = 3.02 eV	E_{bg} = 3.23 eV
ρ = 4.250 g/cm^3	ρ = 3.894 g/cm^3
ΔG°_f = -212.6 kcal/mole	ΔG°_f = -211.4 kcal/mole

Figure 1.3 Unit cell structures of rutile and anatase TiO_2.[11]

The anatase form shows a higher photocatalytic activity because of the larger reduction potential of electrons at the conduction band edge due to its larger

band gap (3.23 vs 3.02 eV in rutile).[40,41] Also, a higher degree of surface hydroxylation is present in the anatase form.[42] Generally, the TiO_2-sensitised photocatalysis process involves the oxidation of surface hydroxide groups, which actively participate in the photodegradation process.[43] Thus, the higher degree of surface hydroxylation in anatase makes it more effective in the photodegradation of a wide range of hazardous compounds.

Currently Degussa P25 TiO_2 is accepted as the most effective research standard.[1,4] It is a non-porous 70:30 anatase-to-rutile mixture with a surface area of 55 $m^2\ g^{-1}$ and particle size of 30 nm in 0.1 μm diameter aggregates. It has a higher photocatalytic activity than any other readily available form of TiO_2. Fujishima's group has reported the development of transparent TiO_2 films with higher photocatalytic activity towards the decomposition of thin oil films than Degussa P25.[43,44] These TiO_2 films show useful self-cleaning, deodorising and antibacterial functions even under the weak UV light existing in typical indoor environments.[45,46,47,48]

1.2.2 Mechanism of TiO_2-Sensitised Photodegradation of Organic Pollutants

The TiO_2-sensitised photomineralisation of organic substrates by oxygen may be summarised as follows

$$\text{Organic pollutant} + O_2 \xrightarrow[h\nu \geq E_{bg}]{TiO_2} CO_2 + H_2O + \text{mineral acids} \qquad (1.2)$$

The energetics and primary processes associated with reaction (1.2) are illustrated in Figure 1.4. Laser flash photolysis experiments[49,50] have provided detailed information of the primary processes associated with the photodegradation process, together with their characteristic time domains, which are summarised in Table 1.1.[1,4]

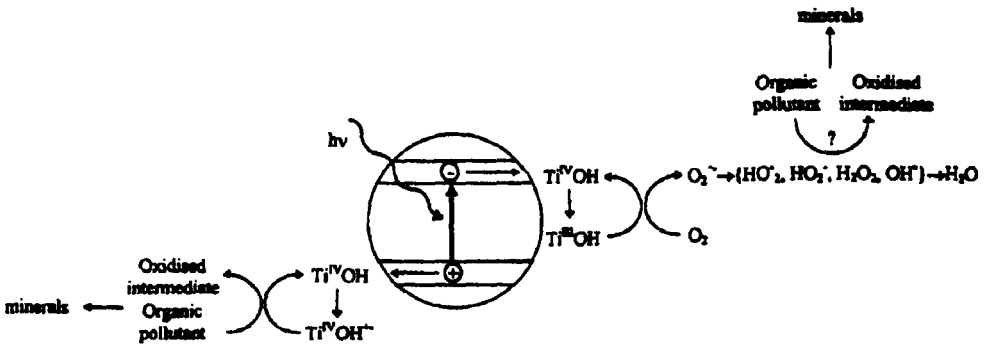

Figure 1.4 Energetics and major general processes for the photomineralisation of organic pollutants in aqueous solution by dissolved oxygen, sensitised by TiO_2 particles.[1]

Table 1.1 Primary processes and associated characteristic time domains in the TiO_2-sensitised photomineralisation of organic pollutants.[1,4] > TiOH represents the primary hydrated surface functionality of TiO_2, $\{> Ti^{IV}OH^{\bullet+}\}$ is the surface-trapped valence band hole (*i.e.*, surface-bound hydroxyl radical), and $\{> Ti^{III}OH\}$ is the surface-trapped conduction band electron.

Primary process	Characteristic time
Charge carrier generation	
$TiO_2 + h\nu \rightarrow h^+ + e^-$	fs (very fast)
Charge carrier trapping	
$h^+ + > Ti^{IV}OH \rightarrow \{> Ti^{IV}OH^{\bullet+}\}$	10 ns (fast)
$e^- + > Ti^{IV}OH \leftrightarrow \{> Ti^{III}OH\}$	100 ps (shallow trap; dynamic equilibrium)
$e^- + > Ti^{IV} \rightarrow > Ti^{III}$	10 ns (deep trap)
Charge carrier recombination	
$e^- + \{> Ti^{IV}OH^{\bullet+}\} \rightarrow > Ti^{IV}OH$	100 ns (slow)
$h^+ + \{> Ti^{III}OH\} \rightarrow > Ti^{IV}OH$	10 ns (fast)
Interfacial charge transfer	
$\{> Ti^{IV}OH^{\bullet+}\}$ + organic pollutant $\rightarrow > Ti^{IV}OH$ + oxidised pollutant	100 ns (slow)
$\{> Ti^{III}OH\} + O_2 \rightarrow > Ti^{IV}OH + O_2^{\bullet-}$	ms (very slow)

In general, for efficient degradation, the organic reactant, RH_2, must be adsorbed onto the photocatalyst surface, where oxidation of the adsorbate can occur either directly through interfacial electron transfer (direct hole oxidation, equation 1.3) or indirectly through an $^{\bullet}OH$ mediated attack (equations 1.4-1.6).

$$h^+ + RH_2 \rightarrow {}^{\bullet}RH + H^+ \quad (1.3)$$

$$h^+ + H_2O \rightarrow {}^{\bullet}OH_{ad} + H^+ \quad (1.4)$$

$$h^+ + OH^-_{ad} \rightarrow {}^{\bullet}OH_{ad} \quad (1.5)$$

$$RH_2 + {}^{\bullet}OH_{ad} \rightarrow {}^{\bullet}RH + H_2O \quad (1.6)$$

Minero *et al.*[51] have shown that the $^{\bullet}OH$ radical does not migrate far from the photogenerated active site on TiO_2, and that the degradation process must occur at the photocatalyst surface or within a few atoms of distance from the surface.

Okamoto *et al.*[52] demonstrated that the formation of hydrogen peroxide (H_2O_2) from superoxide ($O_2^{\bullet-}$) can generate $^{\bullet}OH$ radicals which will also participate in the photodegradation reactions. Molecular oxygen functions as an electron acceptor which is reduced by the electrons of the conduction band to produce superoxide anions (equation 1.7; e_{tr}^- is a trapped conduction band electron).

$$e_{tr}^- + O_2 \rightarrow O_2^{\bullet-} \quad (1.7)$$

In acidic media, the superoxide radical anion protonates to give the hydroperoxide radical, $HO_2^{\bullet}$ (equation 1.8). Reactions 1.9-1.11 provide the pathways for H_2O_2 formation:[4,53,54]

$$O_2^{\bullet-} + H^+ \rightarrow HO_2^{\bullet} \quad (1.8)$$

$$HO_2^{\bullet} + HO_2^{\bullet} \rightarrow H_2O_2 + O_2 \quad (1.9)$$

$$HO_2^{\bullet} + O_2^{\bullet-} \rightarrow HO_2^- + O_2 \quad (1.10)$$

$$HO_2^- + H^+ \rightarrow H_2O_2 \quad (1.11)$$

Hydroxyl radicals can thus be formed via the following reactions (equations 1.12-1.14):[52,53]

$$H_2O_2 + e^- \rightarrow {}^{\bullet}OH + OH^- \quad (1.12)$$

$$H_2O_2 + O_2^{\bullet-} \rightarrow {}^{\bullet}OH + OH^- + O_2 \quad (1.13)$$

$$H_2O_2 \xrightarrow{h\nu} 2\ {}^{\bullet}OH \quad (1.14)$$

There is a significant body of literature showing that oxidation can occur either by mediated $^{\bullet}OH$ radical oxidation[55,56,57,58,59,60] or by direct hole oxidation.[61,62,63,64,65,66,67] Whether direct or mediated reaction occurs will depend on the nature of the organic substrate.[68] The direct oxidation pathway is shown to be more important for strongly adsorbing substrates[68] and at very high substrate concentrations.[69,70]

1.2.3 The Role of Oxygen in TiO_2 Photocatalysis

Oxygen acts as an electron acceptor, scavenging electrons from the conduction band and thus reducing the recombination rate. This process is of particular interest since Gerischer and Heller have suggested that electron transfer to oxygen may be the rate-limiting step in semiconductor photocatalysis.[71,72,73] When the rate of oxygen reduction is not sufficiently fast to match the rate of reaction of holes, an excess of electrons will accumulate on the TiO_2 particles, and the rate of electron-hole recombination will increase. In order to improve the kinetics of the photodegradation process, catalytic sites must be placed on the TiO_2 surface; these sites can be of the form of islands of Pd^0. Gerischer and Heller were able to show that incorporation of Pd^0 in the TiO_2 surface increases the

quantum efficiency of the photoassisted oxidation of 10^{-2} M aqueous 2,2-dichloropropionate 3-fold at 0.01 wt % Pd and 7-fold at 2 wt % Pd.[72]

Lewis and co-workers[74] have developed a flux-matching model of semiconductor photocatalysis based on their work with single-crystal rutile TiO_2 photoelectrodes. In this model, three major carrier decay pathways were identified, namely electron-hole recombination, oxygen reduction by photogenerated electrons and hole transfer to the organic, water or other hole acceptor species in the solution. All this three processes are closely related and none can be stated as being rate-determining. However, they were also able to show that the presence of a Pt catalyst on the surface of the TiO_2 photocatalyst should lead to an enhancement in the rate of the photodegradation process.

It is becoming apparent that molecular oxygen and the superoxide radical anion play an important role in the oxidation of several types of organic reactants.[44,64,75,76,77] Studies of 4-chlorophenol (4-CP) degradation in a TiO_2 slurry suggested that oxygen plays a specific role during photooxidation in addition to scavenging the trapped electrons.[78,79,80] It was found that 4-CP degradation only occurs to a small extent (20%) in the presence of an alternative electron acceptor capable of scavenging the trapped electrons as readily as oxygen, while complete photomineralisation is achieved in a similar time frame when oxygen is present.

Gerischer and Heller[75] have shown that both electrons and oxygen molecules actually participate in the photocatalytic air oxidation of four aliphatic reactants, a hydrocarbon, an alcohol, a ketone and a carboxylic acid. They proposed that molecular oxygen has two roles: it accepts the electron generated in a TiO_2 particle and is reduced to a superoxide radical ($O_2^{\bullet-}$), and it combines with the organic radical, generated upon the hole or $^{\bullet}OH$ radical reaction with the

aliphatic (equation 1.15), to produce an organoperoxy radical ($ROO^{\bullet}$; equation 1.16).

$$RH + h^{+} (\text{or } {}^{\bullet}OH) \rightarrow R^{\bullet} + H^{+} (\text{or } H_2O) \qquad (1.15)$$

$$R^{\bullet} + O_2 \rightarrow ROO^{\bullet} \qquad (1.16)$$

The organoperoxy radical reacts with the superoxide radical to form an unstable tetraoxide (equation 1.17) that decomposes to products. Oxygen plays an essential role in these oxidation reactions.

$$ROO^{\bullet} + O_2^{\bullet -} \rightarrow ROOOO^{-} \qquad (1.17)$$

Fujishima and co-workers[44] have also shown that oxygen and the superoxide radical are involved in the TiO_2 photocatalytic degradation of gas-phase acetaldehyde. In their study of the mechanism of the TiO_2 photocatalytic decomposition of ethanol in aqueous solution, using a microelectrode technique, they were able to show that molecular oxygen participates in the photooxidation reactions.[76] Thus, oxygen plays a major role in the oxidation of the organic substrate.

1.2.4 Kinetics of the Photomineralisation Process

The rate of photomineralisation of an organic substrate, S, sensitised by TiO_2 depends on several factors such as: (i) crystalline form and concentration of TiO_2 particles; (ii) concentration of dissolved oxygen; (iii) nature and concentration of the organic substrate; (iv) intensity of the illuminating source; (v) temperature and pH of the polluted medium; (vi) the presence of interfering adsorbing species and (vii) the effect of mass transport.

The pH of an aqueous solution significantly affects the particle size, surface charge and band edge positions of TiO_2.[81] However, a weak dependence

of the reaction rate on solution pH is usually found.[82,83,84] Changes in rate of photocatalytic activity from one end of the pH range to the other are usually small, often less than one order of magnitude.[12] Also, the photodegradation process is not highly sensitive to minor variations in temperature.[12] The photoassisted degradation rate of aliphatic alcohols was found to be temperature insensitive, indicating that the potentially temperature dependent steps, such as adsorption, desorption, surface migration or rearrangement do not appear to be rate-limiting in this case.[85,86]

Several kinetic models describing mechanisms of photooxidation reactions have been proposed,[57,87,88,89,90,91] but in general, the initial rate of photocatalytic degradation of an organic substrate S matches the Langmuir-Hinshelwood (L-H) kinetic model:[1,4,12]

$$r_i = -\frac{d[S]_i}{dt} = \frac{k_S K_S [S]_i}{1 + K_S [S]_i} \tag{1.18}$$

where r_i is the initial disappearance rate of substrate S, $[S]_i$ is the initial concentration of the organic substrate, K_S is the Langmuir adsorption constant of species S on the TiO_2 surface and k_S is a proportionality constant which provides a measure of the intrinsic reactivity of the photoactivated surface with S.

The coefficient k_S is proportional to I_a^m, where I_a is the intensity of light (photons s^{-1}) and m is a power term which is equal to 0.5 or unity at high or low light intensity respectively.[57] The coefficient k_S is also proportional to the fraction of oxygen adsorbed on TiO_2, θ_{O_2}, which can be expressed by the following equation:

$$\theta_{O_2} = \frac{K_{O_2}[O_2]}{1 + K_{O_2}[O_2]} \tag{1.19}$$

where K_{O_2} is the Langmuir adsorption coefficient for O_2, which appears to be non-competitively adsorbed on TiO_2 due to its exclusive adsorption at Ti^{III} sites; hydroxyl radicals and organic substrates are adsorbed at Ti^{IV}-lattice oxygen sites.[92] Thus equation (1.18) can be expressed more completely as follows:

$$r_i = \frac{\gamma K_{O_2}[O_2] I_a^m K_S [S]_i}{(1 + K_{O_2}[O_2])(1 + K_S[S]_i)} \qquad (1.20)$$

where γ is a proportionality constant.

Equation (1.20) is often found to be applicable to batch suspension systems,[93,94] *i.e.* those in which the semiconductor is dispersed in an aqueous solution containing the organic substrate for photomineralisation. Many flow systems[95] have also been developed in which the semiconductor is immobilised on an inert support and the aqueous solution containing the organic substrate for photomineralisation is passed over it. In these flow systems, equation (1.20) usually still applies, but often with the reaction rate exhibiting a dependence on the flow rate, indicating a mass transfer dependence which is not found with batch systems.[96] Ahmed *et al.*,[97,98] using the channel flow method with electrochemical detection (CFMED) to study the photomineralisation of four chlorophenols, have shown that mass transport is a key parameter controlling the photodegradation kinetics at supported semiconductor surfaces.

1.2.5 Controlled Periodic Illumination Effect in TiO_2 Photocatalysis

The low quantum yields for the oxidation of aqueous pollutants on illuminated TiO_2 interfaces currently prevent the application of photocatalysis for large scale water decontamination.[4] One solution that has been proposed to address this problem is the use of controlled periodic illumination instead of

continuous illumination.[99,100,101] Sczechowski *et al.*[99,102] demonstrated a means of increasing the aqueous phase photoefficiency of formate ion oxidation by using a controlled periodic illumination of a TiO_2 catalyst suspension. They proposed that intermediate species, such as hydroxyl radical and superoxide anion, that are involved in the photocatalytic oxidation of organics can also participate in reactions that result in the recombination of electron-hole pairs or other redox processes that do not oxidise the organic. The build up of these intermediates due to continuous illumination of the particles will favour these undesirable reactions. Controlled periodic illumination may reduce the build up of intermediates and increase the photoefficiency. By illuminating the particles for short intervals, a limited number of electron-hole pairs will be generated, and when the particles are in the dark, the redox reactions leading to oxidation of the organics can take place. After most of the intermediates are consumed, the particles can be illuminated again for another short period. Using this light-dark cycling, they reported a 5-fold increase in the photoefficiency of formate oxidation. However, there was not enough information to support any specific mechanism for the enhancement seen in their work.

Upadhya and Ollis[103] performed a detailed modelling of the experimental work by Sczechowski *et al.* They proposed a transient kinetic model which assumed that the surface coverage of the formate ion (or hydroxyl radicals) is constant during the reaction or that the rate of formate adsorption at least equals the rate of reaction. Adsorption of oxygen on the surface and/or the transfer of conduction band electrons to adsorbed oxygen was assumed to be the rate-limiting step. Thus, use of periodic illumination and darkness provides the dark time intervals required to allow redevelopment of appreciable surface oxygen coverage

or to allow completion of electron transfer to adsorbed oxygen (and completion of follow-on reactions). The work of Upadhya and Ollis provided reasonable agreement between the photoefficiency trends in experimental and model simulation.

Buechler *et al.*[104] have also investigated the photocatalytic oxidation of formate ion at illuminated TiO_2 particles using the controlled periodic illumination effect. The key result from their study was the observation that the formate ion concentration contributed to limiting the photocatalytic rate. At the highest formate ion concentrations, there was little or no controlled periodic illumination effect. However, at lower formate ion concentrations, an apparent controlled periodic illumination effect was observed. The apparent improvement in the efficiency of the photocatalytic process due to the controlled periodic illumination effect was attributed either to mass transport limitations of formate ion and/or oxygen to the catalyst surface or to slow adsorption/reaction steps. They argued that the model proposed by Upadhya and Ollis[103] was only accurate for systems which were limited by the adsorption or reaction of oxygen, and that the formulation of the model failed to account for the enhancement caused by controlled periodic illumination when the photocatalytic rate was limited by adsorption of the formate ion.

In a recent paper, Hoffmann and co-workers[105] have reported on the quantum yields of the photocatalytic oxidation of formate in aqueous TiO_2 suspensions under continuous and periodic illumination. They found that the quantum yields measured under periodic illumination do not exceed those attained by continuous illumination at the same average absorbed photon flux. They argued that the alleged performance enhancements induced by discontinuous

illumination reported by other groups were actually based on quantum yields (or efficiencies) determined under widely different average photon fluxes. Based on their results, Hoffmann and co-workers concluded that no advantage arises from the use of periodic illumination over the continuous regime.

1.2.6 Redox Reactions in Heterogeneous Photocatalysis

There is a large body of work on interfacial electron transfer reactions at colloidal semiconductor particles (diameter of 50-500 Å), which form transparent aqueous dispersions.[106,107,108] These colloidal systems provide an excellent medium in which to investigate electron transfer reactions across a semiconductor/liquid interface, since their dynamic behaviour can be monitored directly by time-resolved techniques such as flash photolysis.[109,110,111]

The elementary steps in the heterogeneous electron transfer induced by light from a semiconductor particle to an appropriate acceptor molecule in solution are: (i) excitation of the semiconductor particle and charge carrier diffusion to the interface; (ii) charge carrier trapping on the particle surface; (iii) encounter complex formation of the electron (or hole) acceptor with the semiconductor particle; (iv) interfacial electron transfer.[106,112]

Grätzel and co-workers[109] studied the dynamics of interfacial electron transfer reactions with colloidal TiO_2 particles, employing methyl viologen (MV^{2+}) as an electron acceptor. Excitation of colloidal TiO_2 leads to electron-hole pair production, with the conduction band electron being subsequently transferred to the MV^{2+} acceptor in solution. The growth of the $MV^{+\bullet}$ absorption reflects the kinetics of this interfacial charge transfer reaction and was followed by using laser photolysis techniques. The reaction kinetics were found to be pseudo-first order

with respect to MV^{2+} concentration, and it was shown that the electron transfer involved bulk diffusion of the acceptor to the semiconductor particle and did not proceed via MV^{2+} adsorbed to the surface of TiO_2. Grätzel and co-workers[109] have also shown that as the pH increases, the rate constant for interfacial electron transfer to MV^{2+} also increases. This results from a cathodic shift in the potential of electrons on the particles (the conduction band potential of TiO_2 is known to be shifted by 59 mV upon changing the pH by one unit,[16,17] but the redox potential of the $MV^{2+}/MV^{+\bullet}$ couple is pH independent), which increases the thermodynamic driving force for reaction. The interfacial electron transfer step controls the rate at lower pH when the overvoltage available to drive the reaction is small. At higher pH, mass transfer effects become increasingly important and determine the overall reaction rate.

Bard and co-workers[113] have also investigated the reduction of MV^{2+} in TiO_2 suspensions using electrochemical techniques. They developed an electrochemical method of probing the behaviour of TiO_2 particles by collection of photogenerated charge (either on the particles or in products formed in solution) on an inert collector electrode immersed in the irradiated suspension. Methyl viologen and sodium acetate were used, respectively, as the electron and hole trapping agents. The anodic photocurrent from illuminated TiO_2 suspensions arises from the production of electron-hole pairs followed by depletion of holes by reaction with acetate and collection of electrons at the electrode. The current is limited by the accumulation of electrons on the particles which increases the rate of electron-hole recombination. The role of MV^{2+} is the removal of electrons from electron-hole recombination sites with the production of an oxidisable species, $MV^{+\bullet}$. The reduced form, $MV^{+\bullet}$, is then oxidised at the collector electrode, thus

enhancing the anodic photocurrents observed. The role of acetate ion is rapid removal of photogenerated holes in an irreversible fashion. Its presence prevents "short circuiting" of the particle by MV^{2+} (*i.e.*, by the reaction $MV^{+\bullet} + h^+ \rightarrow MV^{2+}$), thus allowing the observation of a net photocurrent. A pH effect on the photocurrent was also observed. As the pH of the TiO_2 suspension was increased, the rate of MV^{2+} reduction also increased due to the cathodic shift of the conduction band electrons, which increases the driving force or overpotential for reduction.

Darwent and co-workers[111] also reported a similar pH effect for electron transfer from TiO_2 colloids to an aromatic azo dye, methyl orange.

1.3 Scanning Electrochemical Microscopy

The scanning electrochemical microscope (SECM) was first introduced in 1989 by Bard and co-workers[114] and is one of a family of scanned probe microscopes. The SECM employs an ultramicroelectrode (UME)[115,116,117] probe immersed in solution near a conductive, semiconductive, or insulating substrate such that the electrochemical response of the UME is governed by mass transfer between the interface and UME, as well as by chemical reactions occurring at the interface. The technique can probe both the topography and the reactivity of a surface with a resolution governed by the dimensions of the UME tip, typically of the order of 1-25 μm diameter.

The SECM has been used widely to investigate localised surface reactivity at a variety of solid/liquid interfaces, ranging from studies on adsorption/desorption phenomena and surface diffusion rates[118] to dissolution/growth processes at a variety of materials including metals,[119,120,121]

semiconductors,[122,123] ionic single crystals[124,125,126,127,128] and polymers.[129] It has also provided a quantitative understanding of processes occurring at liquid/liquid[130,131,132] and liquid/gas[133,134] interfaces. In addition SECM has proved to be a powerful probe of biologically important materials,[135,136,137,138] and its use in monitoring electroassisted or photoassisted reactions on semiconductor surfaces has also been reported.[139,140,141,142,143]

Several reviews have been published covering the diverse range of applications of the SECM.[144,145,146,147,148,149]

1.3.1 Basic Principles

The tip used in SECM is usually a disc-shaped UME which consists of a small metal wire (such as platinum or gold), sealed in a glass capillary which is then polished back to expose the wire, resulting in an electrode of micrometer dimensions (Figure 1.5). The geometry of the tip (electrode plus insulating glass capillary) is characterised by the *RG* value:

$$RG = r_g / a \tag{1.21}$$

where r_g is the radius of the glass capillary plus the electrode and a is the radius of the electrode. Usually a typical value of $RG = 10$ is employed.

The tip and substrate are part of an electrochemical cell that usually contains an electroactive mediator, which may be oxidised or reduced at the UME, as well as a supporting electrolyte. The functions of the supporting electrolyte are to both decrease the electrical resistance of the solution and to ensure that mass transport of the electroactive mediator (if charged) to and from the electrode predominantly occurs by diffusion rather than by migration. Usually the tip is an amperometric electrode acting as the working electrode in a

conventional dynamic electrochemical circuit which includes a reference electrode and sometimes an auxiliary electrode, if large currents are to be passed. Because of the low currents associated with UMEs, due to their small size, a two-electrode set-up usually suffices. The current that flows at the tip electrode upon electrolysis of the mediator is usually amplified by a current to voltage converter and recorded via a data acquisition card on a personal computer as a function of tip-substrate distance and/or time.

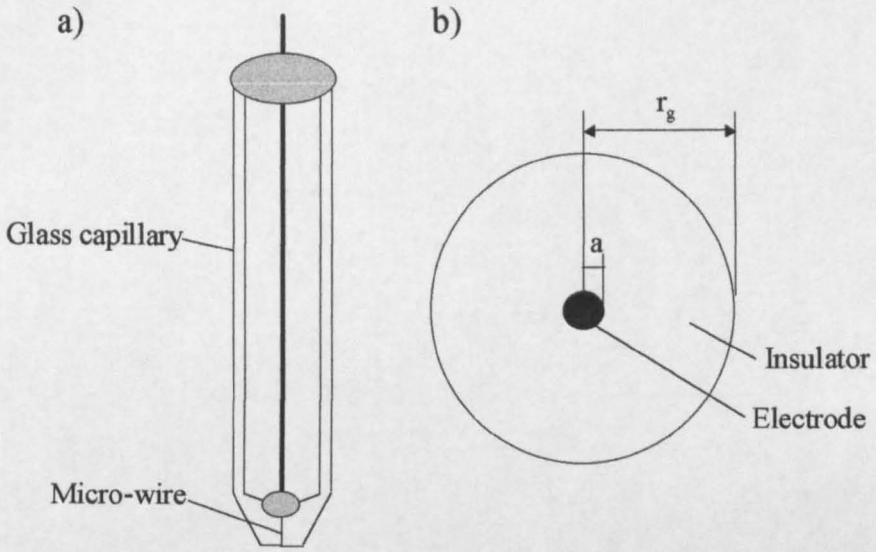

Figure 1.5 Schematic diagram of a glass-coated UME: a) side view, b) end view.

A typical SECM set-up is shown in Figure 1.6. The UME is attached to piezoelectric elements which allow it to be moved and positioned relative to the sample surface in all three Cartesian axial directions, with sub-micron level resolution. If the sample to be studied is a conductor or a semiconductor it can be connected as a second electrode through the use of a bipotentiostat.[150] Insulating samples are not part of the electrochemical cell circuit and are simply positioned underneath the tip.

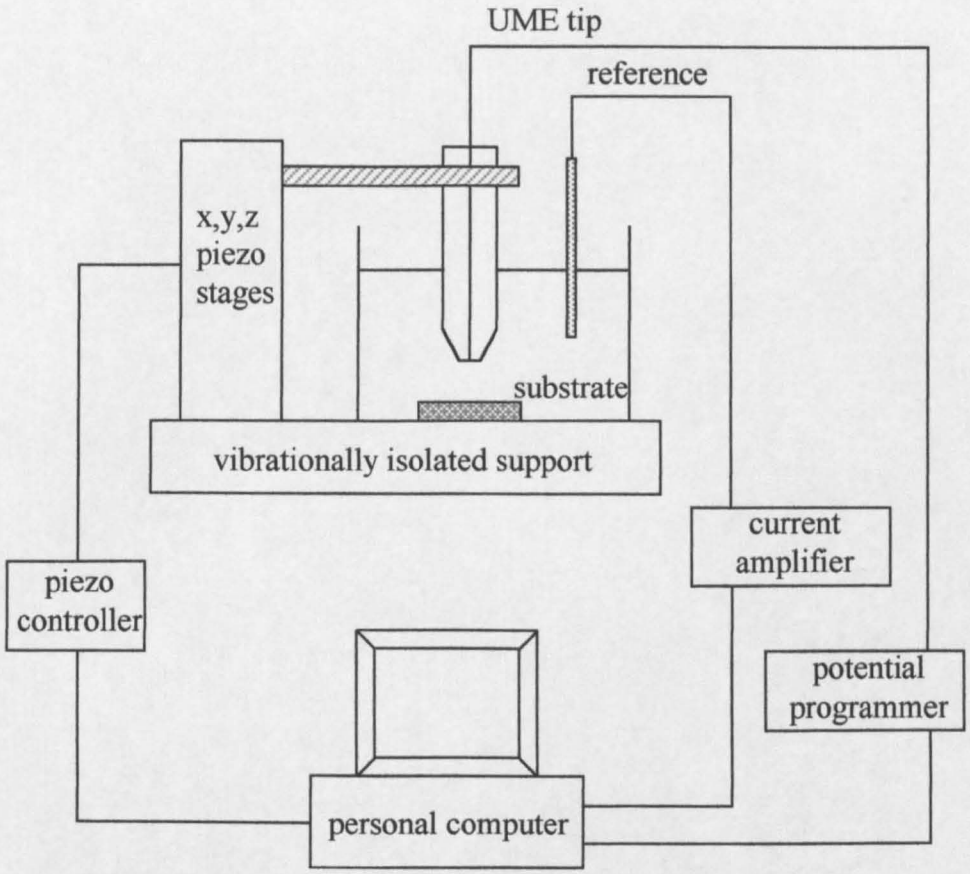

Figure 1.6 Schematic diagram showing a typical SECM set-up.

1.3.2 The Feedback Mode

The most common operating mode of the SECM is the feedback mode,[114,151] where the current response of an UME positioned close to a surface depends on the tip-interface distance and the interaction between an electrogenerated species, produced at the tip, and the interface. For instance, consider a solution containing the reduced form of a redox couple, Red, which can be oxidised at the electrode to produce the oxidised form, Ox. If the potential at the SECM tip is sufficient to oxidise species Red to Ox at a diffusion-limited rate, the current will rapidly assume a steady-state value, which is proportional to the concentration of species Red. Far from the substrate (*i.e.*, where *d*, the tip-

substrate separation ≥ 10 a), the diffusion layer near the tip electrode is roughly hemispherical (Figure 1.7(a)). The corresponding steady-state current attained at the tip, $i(\infty)$, for a disc-shaped UME, is given by[152,153]

$$i(\infty) = 4nFDac^* \tag{1.22}$$

where n is the number of electrons transferred in the redox reaction, F is the Faraday constant, a is the electrode radius, and D and c^* are the diffusion coefficient and bulk concentration of the electroactive mediator, respectively.

When the UME is brought close to an interface, the flux of the mediator towards the electrode is modified by the presence of the interface, compared to the case where the UME is in bulk solution. The effect on the tip current depends on the reactivity of the interface and the tip-interface distance. When the tip is brought near (typically $d < a$ for a pronounced effect) an inert, electrically insulating substrate, diffusion of Red to the tip is hindered and the tip current, i, is lower than that observed in the bulk solution, $i < i(\infty)$ (Figure 1.7(b)). The closer the tip approaches to the substrate, the smaller i becomes. At the limit when the distance between tip and substrate, d, approaches zero, i also approaches zero. This effect is termed negative feedback.[114,154]

When the tip is brought near a redox-active or conductive substrate that is held at a potential for the diffusion-controlled reduction of Ox back to Red, the flux of Red to the tip is enhanced due to the regeneration of Red at the substrate. This redox cycle, shown in Figure 1.7(c), results in an increased current at the electrode compared to that measured for the bulk solution, $i > i(\infty)$. In the limit as d approaches zero, the tip will move into a regime where electron tunnelling can occur and the tip current will get very large. This effect is termed positive feedback.[114,154]

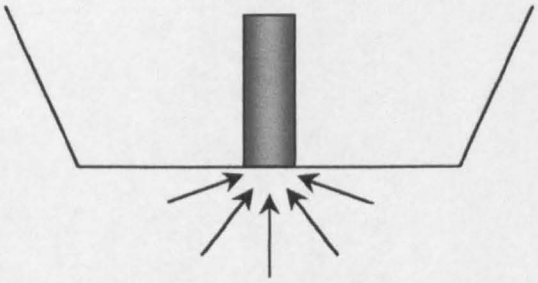

Figure 1.7(a) Schematic of the steady-state hemispherical diffusion profile for an UME positioned in bulk solution.

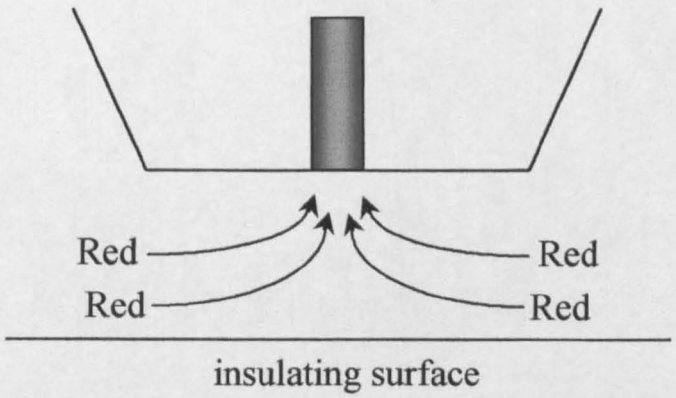

Figure 1.7(b) Negative feedback: hindered diffusion to an UME positioned close to an inert surface.

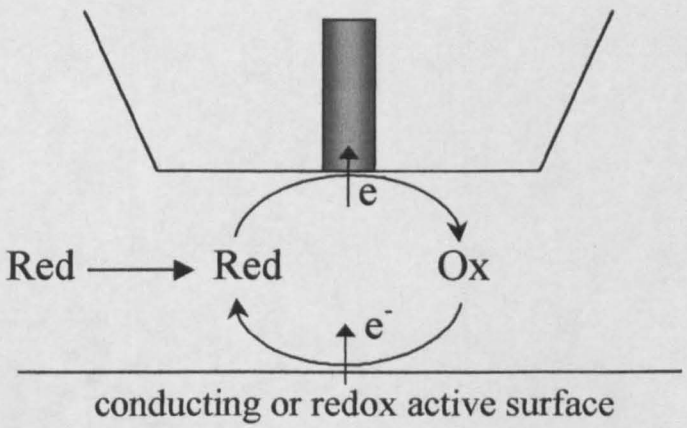

Figure 1.7(c) Positive feedback: diffusion to an UME positioned close to a conducting or redox-active surface.

The magnitude of the negative and positive feedback effects are dependent on the tip-substrate separation, and the positive feedback response also depends on the rate of the interfacial redox reaction.

To measure the kinetics of reactions that occur at an interface, it is possible to construct approach curves, which show the variation of the steady-state current as a function of the tip-interface distance, d. Plots of the theoretical normalised current ratio, $i / i(\infty)$, against the normalised tip-interface separation, d/a, for the limiting cases of negative and positive feedback are shown in Figure 1.8. These limiting cases correspond, respectively, to surface reaction kinetics where the rate is zero, and where the rate of the redox reaction occurring at the substrate is controlled by mass transport. When the redox reaction at the substrate is characterised by finite kinetics, approach curves lie between these two limiting cases and can be fitted to simulated working curves. These are very useful in finding the rate of heterogeneous charge transfer at an interface.[144,150,155]

By scanning the tip in the x-y plane and measuring current changes (the constant height mode) or, less frequently, by maintaining a constant current and measuring the changes in d (constant current mode), one can obtain topographic images of conducting and insulating substrates.[156] The resolution of such images is governed by the tip radius, a, and the tip-substrate distance, d. The SECM feedback mode can also be used to image the reactivity of a surface, when the topography is known.[157] By using a solution which contains two separate mediators, it is possible to record both the topography and the reactivity of a sample in subsequent imaging scans.[158,159]

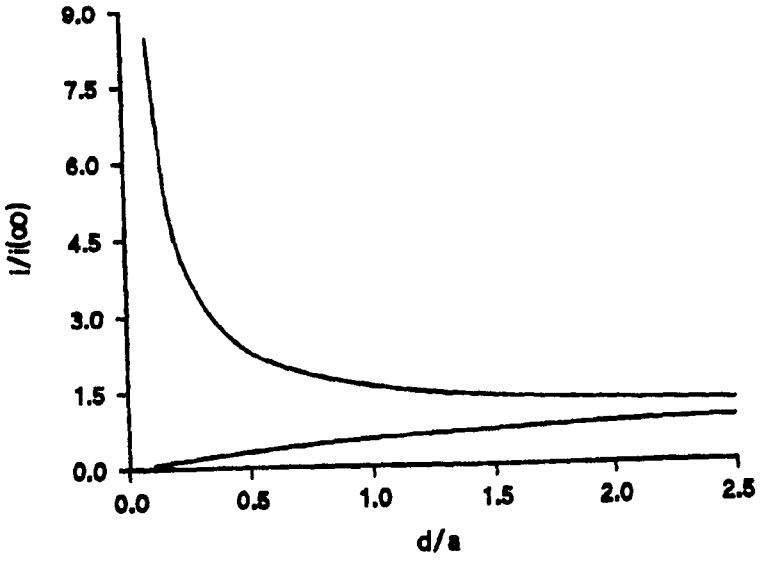

Figure 1.8 Plot of theoretical approach curves for positive (upper curve) and negative (lower curve) feedback of the SECM. Data from J. Kwak and A. J. Bard, *Anal. Chem.*, **1989**, 61, 1221.

1.3.3 The Generation/Collection Mode

In generation/collection (G/C) experiments, one working electrode is used to generate a species that is collected at the second electrode. There are two significantly different G/C SECM arrangements, namely the substrate generation/tip collection (SG/TC) mode[160,161,162,163,164] and the tip generation/substrate collection (TG/SC) mode.[165,166,167,168]

In the TG/SC mode, the tip is used to generate a reactant that is detected at a larger substrate (collector) electrode positioned directly below the tip, typically at a distance $d \leq 2a$. For example, the reaction $Ox + ne^- \rightarrow Red$ occurs at the tip, and the reverse reaction occurs at the substrate (Figure 1.9(a)). With this electrode configuration, a competition is established between (i) the diffusion of Red from the tip to the substrate, with the subsequent regeneration and feedback diffusion of Ox, and (ii) the chemical decomposition of Red to products (if Red is unstable). The TG/SC mode is somewhat similar to the feedback mode of the SECM, but the

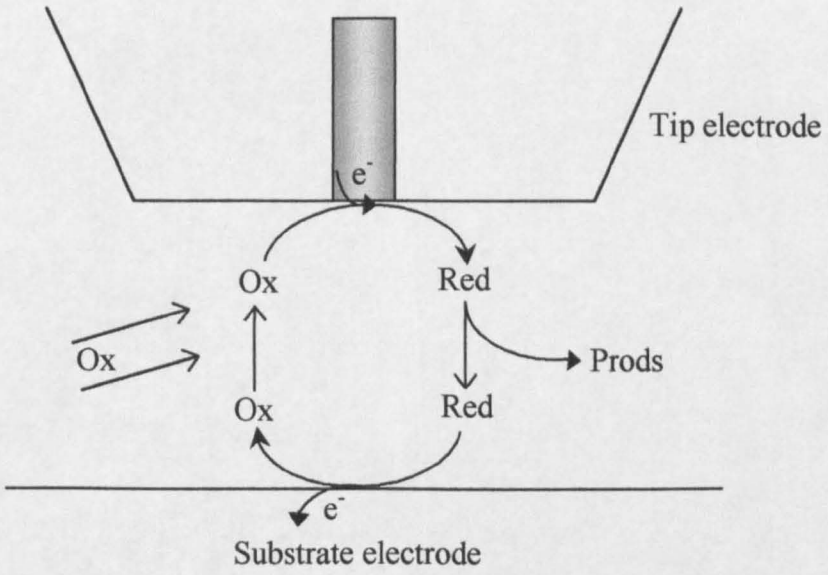

Figure 1.9(a) The TG/SC mode.

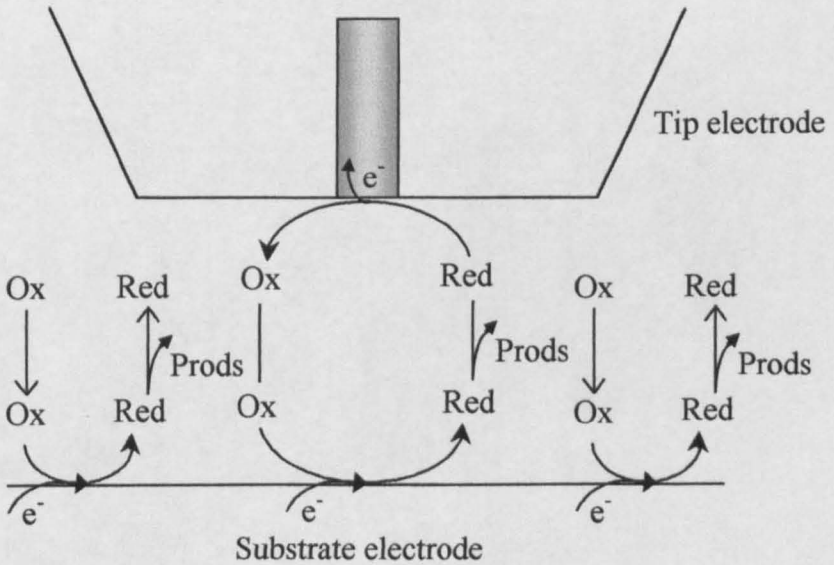

Figure 1.9(b) The SG/TC mode.

former mode includes simultaneous measurements of both tip (i_T) and substrate (i_S) currents. The kinetics of coupled chemical reactions in solution are probed by varying the tip-substrate distance while measuring i_T and i_S. For an uncomplicated process (stable Red), the collection efficiency, i_S/ i_T, is more than 0.99 if L (= d/a) is not very large ($L \leq 2$).[162] Under these conditions, the tip-generated species predominantly diffuses to the larger substrate electrode rather than escaping from the tip-substrate gap. For a process with a coupled chemical reaction (unstable Red), the collection efficiency may be much less than unity, and important kinetic information can be extracted from the i_S/ i_T dependence on the tip-substrate distance. The TG/SC mode is usually used in studies of homogeneous chemical reactions, allowing the determination of very fast homogeneous rate constants (in excess of 1×10^8 M^{-1} s^{-1})[166] under steady-state conditions.

In the SG/TC mode, species Red is electrogenerated at the substrate electrode and the reverse process, in which Red is oxidised to Ox, occurs at the tip (Figure 1.9(b)). The substrate electrode is generally large (up to millimeter dimensions), with a disk of micrometer dimensions serving as the collector electrode.[163,164] Unlike the feedback (and TG/SC) mode, where the overall redox process is essentially confined to the thin layer of solution between the tip and the substrate, in SG/TC experiments, the tip is positioned within a diffusion layer generated by the substrate, which will grow in size with time. If the tip is an amperometric sensor, the reaction occurring on its surface may significantly disturb the substrate diffusion layer. This and also other problems (*e.g.*, physical perturbation of the substrate diffusion layer by the tip, no true steady-state being achieved when the substrate is large and low collection efficiency) have been considered to limit the applicability of the SG/TC mode.[149] However, a

quantitative model for the transient SG/TC response has been developed[164] and the method has been used to measure the lifetime of substrate-generated species.[163] This mode of operation is often simplest when the tip is a potentiometric sensor. Such a passive sensor does not consume analyte and disturbance to the concentration profile of electroactive species generated (or consumed) at the substrate is minimal. As with the feedback and TG/SC modes discussed above, the tip-substrate separation is a key experimental variable. The SG/TC mode can be used for monitoring many heterogeneous processes such as corrosion[142,169] and enzymatic reactions.[170,171] It is also useful for measurements of concentration profiles and fluxes of either electrochemically inactive species (*e.g.*, alkali metal ions)[172] or species undergoing irreversible oxidation/reduction (*e.g.*, glucose).[173]

1.4 Scanning Electrochemical Microscopy as a Probe of Interfacial Photochemical Processes

Ultramicroelectrodes have emerged as powerful tools for investigating a variety of interfacial phenomena at the local level, particularly when operated as probes in the SECM. Fujishima and co-workers[54,76,174,175] have reported the separate monitoring of both oxidation and reduction reactions above TiO_2 sites and metal sites, respectively, using a microelectrode technique. In a refinement of their previous work, they monitored the electrochemically assisted and/or photoassisted reactions on a TiO_2-ITO (indium-tin oxide) composite film using SECM.[176] Polycrystalline TiO_2 was coated onto half of a macroscopic ITO glass substrate, leaving the ITO exposed on the other half of the sample, which was placed in an aqueous solution containing 5 mM $K_4Fe(CN)_6$ and K_2SO_4 as

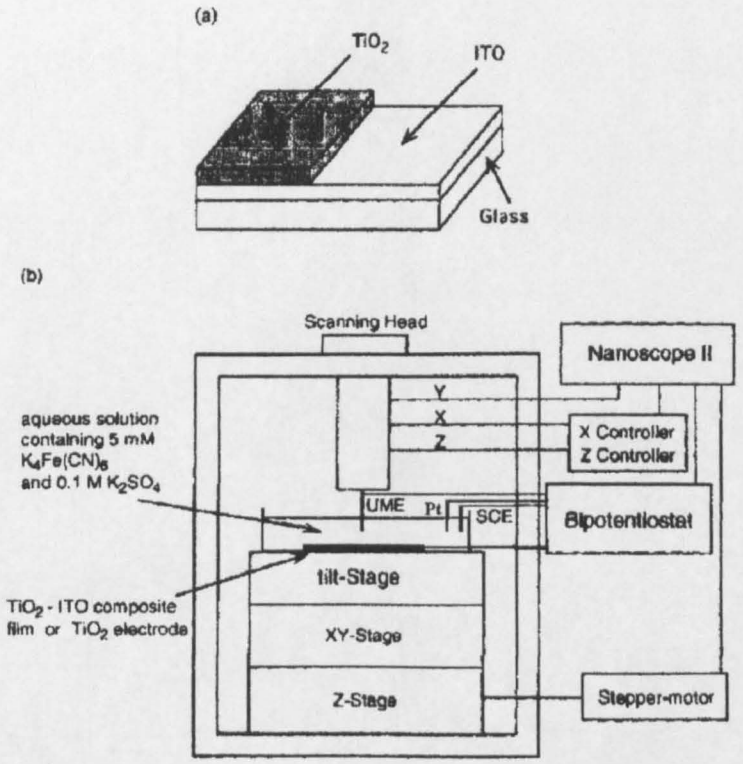

Figure 1.10 (a) Structure of the TiO_2-ITO composite film. (b) Schematic diagram of the experimental set-up.[176]

supporting electrolyte. The schematic diagram of the experimental set-up, taken from their work, is shown in Figure 1.10. They employed 30 μm and 3 μm diameter Pt-Ir UME tips as SECM probes (located far away and in close vicinity to the TiO_2 film) to investigate the negative and positive feedback effects above the TiO_2 surface in the dark and under UV illumination, respectively. In the dark, the microelectrode response is consistent with negative feedback behaviour: the TiO_2 surface acts as an insulating substrate. Under illumination, there was a small decrease in the oxidation current at the UME when it was placed at a relatively large distance above the TiO_2 portion of the surface: ferrocyanide was photooxidised by photogenerated holes, thereby decreasing the amount that could be oxidised at the microelectrode. However, when it was placed very close to the TiO_2 surface, the oxidation current at the UME increased significantly after

turning on the UV light, and that current increase became even larger when the exposed ITO portion was covered by epoxy resin. This current response behaviour is due to positive feedback: ferricyanide produced electrochemically at the UME is reduced back at the illuminated TiO_2 surface by photogenerated electrons. This work demonstrated the utility of the SECM technique for studying the mechanisms of photocatalytic reactions on TiO_2 surfaces by showing that both oxidation and reduction reactions can occur simultaneously on an illuminated TiO_2 film.

In a recent report, Haram and Bard[177] have also demonstrated that SECM can be used to probe the kinetics of photoelectrochemical transfer reactions at semiconductor/solution interfaces. They employed a polycrystalline cadmium sulfide (CdS) thin film in contact with a solution containing methyl viologen radical cation ($MV^{\bullet+}$) as the redox mediator and triethanolamine (TEOA) as the hole scavenger. In the absence of illumination, SECM approach curves to CdS films deposited on glass showed negative feedback, as the substrate could not reduce tip generated MV^{2+}, *i.e.*, the film behaved as an insulator. However, upon illumination, MV^{2+} can be reduced to $MV^{\bullet+}$ at the CdS surface by photogenerated electrons, resulting in an increase in current at the microelectrode, giving positive feedback. The amount of feedback was a measure of the rate of generation of $MV^{\bullet+}$. Apparent pseudo-first-order rate constants for the photoelectron transfer reaction were estimated by fitting experimental approach curves to theory. A schematic of the experimental set-up used by Haram and Bard is shown in Figure 1.11.

Kemp *et al.*[178] investigated the kinetics of photomineralisation of aqueous 2,4-dichlorophenol, and monitored the generation of chloride ions during the

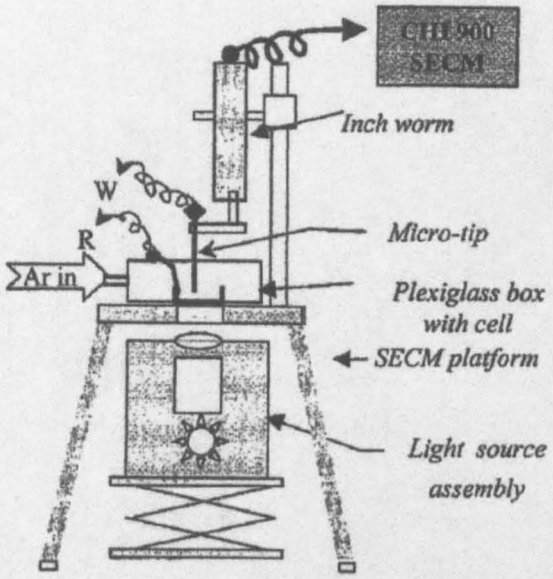

Figure 1.11 Schematic diagram of the experimental set-up used for photoelectron transfer-SECM measurements.[177]

photodegradation process, using a potentiometric Ag/AgCl UME positioned at micrometer distances above a UV-illuminated TiO_2 film. Experiments were performed at several tip-substrate distances, and the concentration of chloride was recorded as a function of time after turning on and turning off the UV irradiation. A schematic diagram of the experimental set-up employed is given in Figure 1.12. The measured quantum yield was in close agreement with that deduced for the same reaction with the TiO_2 suspended in solution.[179] This suggests that, with the experimental set-up adopted, light was not significantly shielded from the surface by the probe. However, to confirm this, the authors proposed the use of a new type of photoelectrochemical probe, developed by Smyrl *et al.*,[141] in which the surface was illuminated using an optical fibre surrounded by a ring UME.

Smyrl and co-workers[141,180] developed a new instrumental technique that combines the characteristics of scanning electrochemical microscopy (SECM) and scanning photoelectrochemical microscopy (PEM).[181] To combine both techniques, *i.e.*, scanning photoelectrochemical and electrochemical microscopy

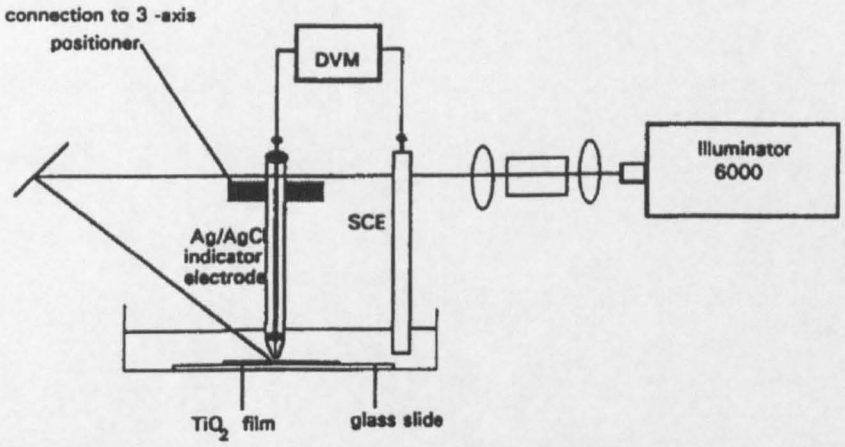

Figure 1.12 Schematic diagram of the experimental arrangement employed to monitor Cl^- close to the surface of a TiO_2 film during photomineralisation. DVM and SCE denote digital voltmeter and saturated calomel electrode, respectively.[178]

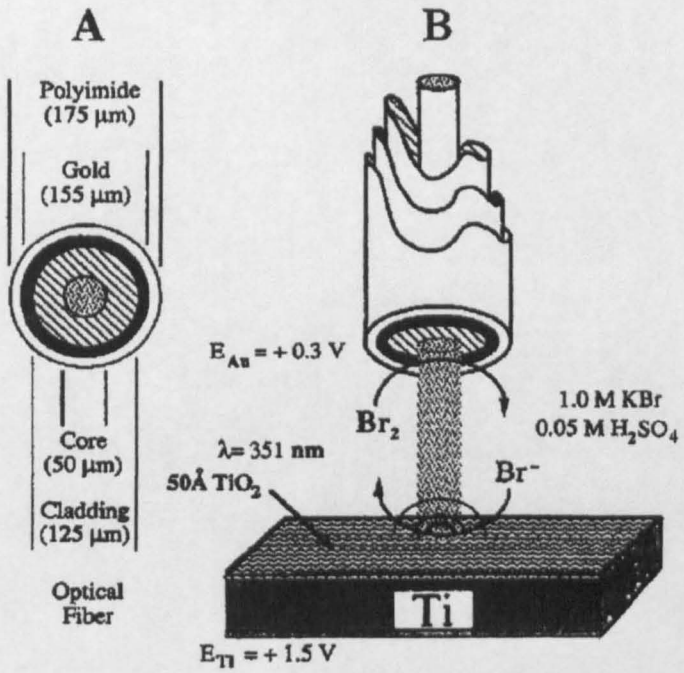

Figure 1.13 Diagram of the gold-coated optical fibre used to study reactions at the surface of a Ti/TiO_2 substrate.[180]

(SPECM), an optical fibre coated with gold and encased in an outer polymer film was used. The gold ring served as a microelectrode to carry out the electrochemical reactions, while the core of the fibre acted as a local illumination source. They used SPECM to identify pitting precursor sites on a titanium sample

with a 50 Å oxide layer in an acidic KBr solution.[180] Figure 1.13 shows a schematic of the gold coated optical fibre tip and the side view of the SPECM experiment. The resolution of the SPECM probe is largely a function of the size of the gold ring, the illumination spot size, and the probe/sample separation distance. By reducing the size of both the optical fibre and the concentric gold ring, it is possible to improve the spatial resolution. Improvements in the imaging capabilities of SPECM have been made by Shi *et al.*,[182] who prepared optical fibre microelectrodes with a total tip diameter less than 5 μm.

1.5 Aims

The general goal of this thesis is to use the SECM technique to obtain a more detailed understanding of photoelectrochemical reactions occurring at supported TiO_2 surfaces. A new SECM approach, involving both amperometric and potentiometric electrodes, has been developed and used to monitor interfacial photoprocesses with high spatial resolution.

In this chapter an overview of the current status of the environmentally relevant TiO_2-sensitised photomineralisation of organic pollutants was provided. This is followed by an overview of experimental details in chapter 2. Since the aim of this work is to develop an electrochemical method to monitor interfacial photochemical processes, a knowledge of the light flux intensity reaching the TiO_2 surface is required. Chapter 3 concerns the development of a new *in situ* microelectrochemical actinometer system *via* the amperometric detection mode of the SECM. The liquid phase potassium ferrioxalate actinometer was chosen. A theoretical model has been developed to determine the intensity of the light flux reaching the TiO_2 surface.

Oxygen plays a key role in photomineralisation processes catalysed by illuminated TiO_2. Thus, in chapter 4, a new approach to monitoring the photoelectrochemical reduction of oxygen was developed, in which the chronoamperometric behaviour for oxygen reduction was recorded after stepping the light flux at a TiO_2 film on and off. The kinetics of the reduction process are interpreted through various theoretical models proposed in the literature.

It would be interesting to know if there is a link between the rate of oxygen consumption and the rate of product formation in the photomineralisation process sensitised by TiO_2. Hence, in chapter 5, the TiO_2 mediated photodegradation of a model pollutant, 4-chlorophenol, was studied. The generation of chloride ions during the photomineralisation process was monitored using a potentiometric microelectrode positioned very close to the TiO_2 surface. The production of chloride ions was modelled using the Langmuir-Hinshelwood kinetic equation for heterogeneous catalytic processes.

Finally, in chapter 6, the photoelectrochemical transfer kinetics at the TiO_2/aqueous interface was studied using the methyl viologen ($MV^{2+/\bullet+}$) redox couple. Using both the feedback mode and SG/TC mode it is shown how competing pathways involved in the reaction of MV^{2+} at the TiO_2 surface can be identified.

References

1. A. Mills and S. Le Hunte, *J. Photochem. Photobiol. A: Chem*, **1997**, 108, 1.

2. M. Schiavello (Ed.), *Photocatalysis and Environment*, Kluwer Academic Publishers, Dordrecht, 1988.

3. D. F. Ollis and H. Al-Ekabi (Eds.), *Photocatalytic Purification and Treatment of Water and Air*, Elsevier, New York, 1993.

4. M. R. Hoffmann, S. T. Martin, W. Choi and D.W. Bahnemann, *Chem. Rev.*, **1995**, 95, 69.

5. D. F. Ollis, *C. R. Acad. Sci. Paris, Série IIC, Chimie / Chemistry*, **2000**, 3, 405.

6. A. Fujishima, T. N. Rao and D. A. Tryk, *J. Photochem. Photobiol. C: Photochem. Rev.*, **2000**, 1, 1.

7. A. Fujishima, K. Hashimoto and T. Watanabe, *TiO_2 Photocatalysis: Fundamentals and Applications*, BKC, Tokyo, 1999.

8. A. Heller, *Acc. Chem. Res.*, **1995**, 28, 503.

9. D. A. Tryk, A. Fujishima and K. Honda, *Electrochim. Acta*, **2000**, 45, 2363.

10. A. Mills and S.-K. Lee, *J. Photochem. Photobiol. A: Chem*, **2002**, 152, 233.

11. A. L. Linsebigler, G. Lu and J. T. Yates Jr., *Chem. Rev.*, **1995**, 95, 735.

12. M. A. Fox and M. T. Dulay, *Chem. Rev.*, **1993**, 93, 341.

13. N. Serpone, D. Lawless, R. Terzian and D. Meisel in *Electrochemistry in Colloids and Dispersions*, R. A. Mackay and J. Texter (Eds), VCH Publishers, Inc., New York, 1992, p399.

14. R. W. Matthews, *J. Catal.*, **1988**, 113, 549.

15. H. Gerischer in *Photocatalytic Purification and Treatment of Water and Air*, D. F. Ollis and H. Al-Ekabi (Eds.), Elsevier, New York, 1993.

16. A. J. Nozik, *Ann. Rev. Phys. Chem.*, **1978**, 29, 189.

17. T. Watanabe, A. Fujishima, O. Tatsuoki and K. Honda, *Bull. Chem. Soc. Jpn.*, **1976**, 49, 8.

18. E. Pelizzetti, C. Minero and V. Maurino, *Adv. Colloid Interface Sci.*, **1990**, 32, 271.

19. P. V. Kamat, *Chem. Rev.*, **1993**, 93, 267.

20. A. Mills, R. H. Davies and D. Worsley, *Chem. Soc. Rev.*, **1993**, 22, 417.

21. J. M. Herrmann, C. Guillard and P. Pichat, *Catal. Today*, **1993**, 17, 7.

22. J. C. Ireland, P. Klostermann, E. W. Rice and R. M. Clark, *Appl. Environ. Microbiol.*, **1993**, 59, 1668.

23. J. C. Sjogren and R. A. Sierka, *Appl. Environ. Microbiol.*, **1994**, 60, 344.

24. R. X. Cai, Y. Kubota, T. Shuin, H. Sakai, K. Hashimoto and A. Fujishima, *Cancer Res.*, **1992**, 52, 2346.

25. R. Cai, K. Hashimoto, Y. Kubota and A. Fujishima, *Chem Lett.*, **1992**, 427.

26. K. Suzuki in *Photocatalytic Purification and Treatment of Water and Air*, D. F. Ollis and H. Al-Ekabi (Eds.), Elsevier, New York, 1993.

27. K. E. Karakitsou and X. E. Verykios, *J. Phys. Chem.*, **1993**, 97, 1184.

28. M. Grätzel, *Acc. Chem. Res.*, **1981**, 14, 376.

29. D. Duonghong, E. Borgarello and M. Grätzel, *J. Am. Chem. Soc.*, **1981**, 103, 4685.

30. E. Borgarello, J. Kiwi, E. Pelizzetti, M. Visca and M. Grätzel, *Nature*, **1981**, 289, 158.

31. M. Khan, D. Chatterjee, M. Krishnaratnam and M. Bala, *J. Mol. Catal.*, **1992**, 72, 13.

32. M. Khan and N. N. Rao, *J. Photochem. Photobiol. A: Chem*, **1991**, 56, 101.

33. M. Schiavello, *Electrochim. Acta*, **1993**, 38, 11.

34. H. Gerischer and A. Heller, *J. Electrochem. Soc.*, **1992**, 139, 113.

35. N. B. Jackson, C. M. Wang, Z. Luo, J. Schwitzgebel, J. G. Ekerdt, J. R. Brock and A. Heller, *J. Electrochem. Soc.*, **1991**, 138, 3660.

36. M. Nair, Z. H. Luo and A. Heller, *Ind. Eng. Chem. Res.*, **1993**, 32, 2318.

37. A. Mills and J. Wang, *J. Photochem. Photobiol. A: Chem.*, **1998**, 118, 53.

38. J. K. Burdett, T. Hughbands, J. M. Gordon, J. W. Richardson Jr. and J. V. Smith, *J. Am. Chem. Soc.*, **1987**, 109, 3639.

39. A. Fahmi, C. Minot, B. Silvi and M. Causa, *Phys. Rev. B*, **1993**, 47, 11717.

40. K. Tanaka, M. F. V. Capule and T. Hisanaga, *Chem. Phys. Lett.*, **1991**, 187, 73.

41. K.-M. Schindler and M. J. Kunst, *J. Phys. Chem.*, **1990**, 94, 8222.

42. J. Augustynsky, *Electrochim. Acta*, **1993**, 38, 43.

43. A. Fujishima and T. N. Rao, *Proc. Indian Acad. Sci. (Chem. Sci.)*, **1997**, 109, 471.

44. I. Sopyan, M. Watanabe, S. Murasawa, K. Hashimoto and A. Fujishima, *J. Photochem. Photobiol. A: Chem*, **1996**, 98, 79.

45. N. Negishi, T. Iyoda, K. Hashimoto and A. Fujishima, *Chem. Lett.*, **1995**, 841.

46. H. Matsubara, M. Takada, S. Koyama, K. Hashimoto and A. Fujishima, *Chem. Lett.*, **1995**, 767.

47. Y. Kikuchi, K. Sunada, T. Iyoda, K. Hashimoto and A. Fujishima, *J. Photochem. Photobiol. A: Chem*, **1997**, 106, 51.

48. I. Sopyan, S. Murasawa, K. Hashimoto and A. Fujishima, *Chem. Lett.*, **1994**, 723.

49. S. T. Martin, H. Herrmann, W. Choi and M. R. Hoffmann, *Trans. Faraday Soc.*, **1994**, 90, 3315.

50. S. T. Martin, H. Herrmann and M. R. Hoffmann, *Trans. Faraday Soc.*, **1994**, 90, 3323.

51. C. Minero, F. Catozzo and E. Pelizzetti, *Langmuir*, **1992**, 8, 481.

52. K. Okamoto, Y. Yamamoto, H. Tanaka, M. Tanaka, *Bull. Chem. Soc. Jpn.*, **1985**, 58, 2015.

53. E. Pelizzetti and C. Minero, *Electrochim. Acta*, **1993**, 38, 47.

54. H. Sakai, R. Baba, K. Hashimoto, A. Fujishima and A. Heller, *J. Phys. Chem.*, **1995**, 99, 11896.

55. V. Augugliaro, L. Palmisano, A. Sclafani, C. Minero and E. Pelizzetti, *Toxicol. Environ. Chem.*, **1988**, 16, 89.

56. C. S. Turchi and D. F. Ollis, *J. Catal.*, **1989**, 119, 480.

57. C. S. Turchi and D. F. Ollis, *J. Catal.*, **1990**, 122, 178.

58. R. Terzian, N. Serpone, R. B. Draper, M. A. Fox and E. Pelizzetti, *Langmuir*, **1991**, 7, 3081.

59. D. Lawless, N. Serpone and D. Meisel, *J. Phys. Chem.*, **1991**, 95, 5166.

60. G. Mills and M. R. Hoffmann, *Environ. Sci. Technol.*, **1993**, 27, 1681.

61. R. B. Draper and M. A. Fox, *Langmuir*, **1990**, 6, 1396.

62. Y. Mao, C. Schoneich and K. D. Asmus, *J. Phys. Chem.*, **1991**, 95, 80.

63. E. R. Carraway, A. J. Hoffmann and M. R. Hoffmann, *Environ. Sci. Technol.*, **1994**, 28, 786.

64. L. Cermenati, P. Pichat, C. Guillard and A. Albini, *J. Phys. Chem. B*, **1997**, 101, 2650.

65. O. d'Hennezel, P. Pichat and D. F. Ollis, *J. Photochem. Photobiol. A: Chem*, **1998**, 118, 197.

66. K. Ishibashi, A. Fujishima, T. Watanabe and K. Hashimoto, *J. Photochem. Photobiol. A: Chem*, **2000**, 134, 139.

67. X. Li, J. W. Cubbage and W. S. Jenks, *J. Photochem. Photobiol. A: Chem*, **2001**, 143, 69.

68. J. M. Kesselman, O. Weres, N. S. Lewis and M. R. Hoffmann, *J. Phys. Chem. B*, **1997**, 101, 2637.

69. S. Goldstein, G. Czapski and J. J. Rabani, *J. Phys. Chem.*, **1994**, 98, 6586.

70. L. Sun and J. R. Bolton, *J. Phys. Chem.*, **1996**, 100, 4127.

71. H. Gerischer and A. Heller, *J. Electrochem. Soc.*, **1992**, 139, 113.

72. C. M. Wang, A. Heller and H. Gerischer, *J. Am. Chem. Soc.*, **1992**, 114, 5230.

73. H. Gerischer and A. Heller, *J. Phys. Chem.*, **1991**, 95, 5261.

74. J. M. Kesselman, G. A. Shreve, M. R. Hoffmann and N. S. Lewis, *J. Phys. Chem.*, **1994**, 98, 13385.

75. J. Schwitzgebel, J. G. Ekerdt, H. Gerischer and A. Heller, *J. Phys. Chem.*, **1995**, 99, 5633.

76. K. Ikeda, H. Sakai, R. Baba, K. Hashimoto and A. Fujishima, *J. Phys. Chem. B*, **1997**, 101, 2617.

77. K. Vinodgopal, U. Stafford, K. A. Gray and P. V. Kamat, *J. Phys. Chem.*, **1994**, 98, 6797.

78. U. Stafford, K. A. Gray, P. V. Kamat and A. Varma, *Chem. Phys. Lett.*, **1993**, 205, 55.

79. K. A. Gray, U. Stafford, M. S. Dieckmann and P. V. Kamat in *Photocatalytic Purification and Treatment of Water and Air*, D. F. Ollis and H. Al-Ekabi (Eds.), Elsevier, New York, 1993, p 455.

80. R. W. Matthews, *J. Catal.*, **1988**, 111, 264.

81. B. Siffert and J. M. Metzger, *Colloids Surf.*, **1991**, 53, 79.

82. J. Sabate, M. A. Anderson, M. A. Aguado, J. Guminez, S. Cervera-March and C. G. Hill, *J. Mol. Catal.*, **1992**, 71, 57.

83. T. L. Rose and C. Nanjundiah, *J. Phys. Chem.*, **1985**, 89, 3766.

84. G. T. Brown and J. R. Darwent, *J. Phys. Chem.*, **1984**, 88, 4855.

85. P. Pichat, M.-N. Mozzanega, J. Disdier and J.-M. Herrmann, *Nouv. J. Chim.*, **1982**, 11, 559.

86. N. R. Blake and G. L. Griffin, *J. Phys. Chem.*, **1988**, 92, 5697.

87. A. Hong, M. E. Zappi, C. H. Kuo and D. Hill, *J. Environ. Eng.*, **1996**, 122, 58.

88. J. C. Crittenden, Y. Zhang, D. W. Hand and D. L. Perram, *Water Environ. Res.*, **1996**, 68, 270.

89. L. Rideh, A. Wehrer, D. Ronze and A. Zoulalian, *Catal. Today*, **1999**, 48, 357.

90. C. Minero, *Catal. Today*, **1999**, 54, 205.

91. H. T. Chang, N.-M. Wu and F. Zhu, *Water Res.*, **2000**, 34, 407.

92. R. Terzian, N. Serpone, C. Minero and E. Pelizzetti, *J. Catal.*, **1991**, 128, 352.

93. J. Cunningham and P. Sedlak, *J. Photochem. Photobiol. A: Chem.*, **1994**, 77, 255.

94. J.-C. D' Oliveira, G. Al-Sayyed and P. Pichat, *J. Environ. Sci. Technol.*, **1990**, 24, 990.

95. M. Bideau, B. Claudel, C. Dubien, L. Faure and H. Kazouan, *J. Photochem. Photobiol. A: Chem.*, **1995**, 91, 137.

96. C. S. Turchi and D. F. Ollis, *J. Phys. Chem.*, **1988**, 92, 6852.

97. S. Ahmed, C. E. Jones, T. J. Kemp and P. R. Unwin, *Phys. Chem. Chem. Phys.*, **1999**, 1, 5229.

98. S. Ahmed, T. J. Kemp and P. R. Unwin, *J. Photochem. Photobiol. A: Chem.*, **2001**, 141, 69.

99. J. G. Sczechowski, C. A. Koval and R. D. Noble, *J. Photochem. Photobiol. A: Chem.*, **1993**, 74, 273.

100. N. S. Foster, C. A. Koval, J. G. Sczechowski and R. D. Noble, *J. Electroanal. Chem.*, **1996**, 406, 213.

101. K. J. Buechler, C. H. Nam, T. M. Zawistowski, R. D. Noble and C. A. Koval, *Ind. Eng. Chem. Res.*, **1999**, 38, 1258.

102. J. G. Sczechowski, C. A. Koval and R. D. Noble in *Photocatalytic Purification and Treatment of Water and Air*, D. F. Ollis and H. Al-Ekabi (Eds.), Elsevier, New York, 1993.

103. S. Upadhya and D. F. Ollis, *J. Phys. Chem. B*, **1997**, 101, 2625.

104. K. J. Buechler, T. M. Zawistowski, R. D. Noble and C. A. Koval, *Ind. Eng. Chem. Res.*, **2001**, 40, 1097.

105. C. J. G. Cornu, A. J. Colussi and M. R. Hoffmann, *J. Phys. Chem. B*, **2001**, 105, 1351.

106. M. Grätzel and A. J. Frank, *J. Phys. Chem.*, **1982**, 86, 2964.

107. G. T. Brown, J. R. Darwent and P. D. I. Fletcher, *J. Am. Chem. Soc.*, **1985**, 107, 6446.

108. J. R. Darwent, *J. Chem. Soc., Faraday Trans. 1*, **1984**, 80, 183.

109. D. Duonghong, J. Ramsden and M. Grätzel, *J. Am. Chem. Soc.*, **1982**, 104, 2977.

110. J. Moser and M. Grätzel, *J. Am. Chem. Soc.*, **1983**, 105, 6547.

111. G. T. Brown and J. R. Darwent, *J. Chem. Soc., Faraday Trans. 1*, **1984**, 80, 1631.

112. A. Hagfeldt and M. Grätzel, *Chem. Rev.*, **1995**, 95, 49.

113. M. D. Ward, J. R. White and A. J. Bard, *J. Am. Chem. Soc.*, **1983**, 105, 27.

114. A. J. Bard, F.-R. F. Fan, J. Kwak and O. Lev, *Anal. Chem.*, **1989**, 61, 132.

115. R. M. Wightman, *Science*, **1988**, 240, 415.

116. R. J. Forster, *Chem. Soc. Rev.*, **1994**, 289.

117. C. G. Zoski, *Electroanal.*, **2002**, 14, 1041.

118. P. R. Unwin and A. J. Bard, *J. Phys. Chem.*, **1992**, 96, 5035.

119. D. Mandler and A. J. Bard, *J. Electrochem. Soc.*, **1989**, 136, 3143.

120. D. Mandler and A. J. Bard, *J. Electrochem. Soc.*, **1990**, 137, 1079.

121. J. V. Macpherson, C. J. Slevin and P. R. Unwin, *J. Chem. Soc. Faraday Trans.*, **1996**, 92, 3799.

122. D. Mandler and A. J. Bard, *J. Electrochem. Soc.*, **1990**, 137, 2468.

123. D. Mandler and A. J. Bard, *Langmuir*, **1990**, 6, 1489.

124. J. V. Macpherson and P. R. Unwin, *J. Phys. Chem.*, **1994**, 98, 1704.

125. J. V. Macpherson and P. R. Unwin, *J. Phys. Chem.*, **1995**, 99, 3338.

126. J. V. Macpherson and P. R. Unwin, *J. Phys. Chem.*, **1995**, 99, 14824.

127. J. V. Macpherson and P. R. Unwin, *J. Phys. Chem.*, **1996**, 100, 19475.

128. J. V. Macpherson, P. R. Unwin, A. C. Hillier and A. J. Bard, *J. Am. Chem. Soc.*, **1996**, 118, 6445.

129. C. Kranz, H. E. Gaub and W. Schuhmann, *Adv. Mater.*, **1996**, 8, 634.

130. A. L. Barker, M. Gonsalves, J. V. Macpherson, C. J. Slevin and P. R. Unwin, *Anal. Chim. Acta*, **1999**, 385, 223.

131. M. V. Mirkin, *Mikrochim. Acta*, **1999**, 130, 127.

132. S. Amemiya, Z. Ding, J. Zhou and A. J. Bard, *J. Electroanal. Chem.*, **2000**, 483, 7.

133. C. J. Slevin, J. V. Macpherson and P. R. Unwin, *J. Phys. Chem. B*, **1997**, 101, 10851.

134. C. J. Slevin, S. Ryley, D. J. Walton and P. R. Unwin, *Langmuir*, **1998**, 14, 5331.

135. B. Liu, W. Cheng, S. A. Rotenberg and M. V. Mirkin, *J. Electroanal. Chem.*, **2001**, 500, 590.

136. C. Lee, J. Kwak and A. J. Bard, *Proc. Natl. Acad. Sci. USA*, **1990**, 87, 1740.

137. M. Tsionsky, Z. G. Cardon, A. J. Bard and R. B. Jackson, *Plant Physiol.*, **1997**, 113, 895.

138. J. V. Macpherson, D. O'Hare, P. R. Unwin and C. P. Winlove, *Biophys. J.*, **1997**, 73, 2771.

139. B. R. Horrocks, M. V. Mirkin and A. J. Bard, *J. Phys. Chem.*, **1994**, 98, 9106.

140. S. B. Basame and H. S. White, *J. Phys. Chem.*, **1995**, 99, 16430.

141. N. Casillas, P. James and W. H. Smyrl, *J. Electrochem. Soc.*, **1995**, 142, L16.

142. N. Casillas, S. Charlebois, W. H. Smyrl and H. White, *J. Electrochem. Soc.*, **1994**, 141, 636.

143. S. Meltzer and D. Mandler, *J. Chem. Soc. Faraday Trans*, **1995**, 91, 1019.

144. A. J. Bard and M. V. Mirkin (Eds.), *Scanning Electrochemical Microscopy*, Marcel Dekker, New York, 2001.

145. M. V. Mirkin and B. R. Horrocks, *Anal. Chim. Acta*, **2000**, 406, 119.

146. M. V. Mirkin, *Anal. Chem.*, **1996**, 68, 177A.

147. P. R. Unwin and J. V. Macpherson, *Chem. Ind.*, **1995**, 21, 874.

148. M. Arca, A. J. Bard, B. R. Horrocks, T. C. Richards and D. A. Triechel, *Analyst*, **1994**, 119, 719.

149. A. J. Bard, F.-R. F. Fan and M. V. Mirkin in *Electroanalytical Chemistry*, Vol. 18, A. J. Bard (Ed.), Marcel Dekker, New York, 1994, p. 243.

150. A. J. Bard, M. V. Mirkin, P. R. Unwin and D. O. Wipf, *J. Phys. Chem.*, **1992**, 96, 1861.

151. J. Kwak and A. J. Bard, *Anal. Chem.*, **1989**, 61, 1221.

152. Y. Saito, *Rev. Polarogr.*, **1968**, 15, 177.

153. J. Newman, *J. Electrochem. Soc.*, **1966**, 113, 501.

154. A. J. Bard, G. Denuault, C. Lee, D. Mandler and D. O. Wipf, *Acc. Chem. Res.*, **1990**, 23, 357.

155. D. O. Wipf and A. J. Bard, *J. Electrochem. Soc.*, **1991**, 138, 469.

156. F.-R. F. Fan in *Scanning Electrochemical Microscopy*, A. J. Bard and M. V. Mirkin (Eds.), Marcel Dekker, New York, 2001, p. 111.

157. D. O. Wipf and A. J. Bard, *J. Electrochem. Soc.*, **1991**, 138, L4.

158. M. Gonsalves, A. L. Barker, J. V. Macpherson, P. R. Unwin, D. O'Hare and C. P. Winlove, *Biophys. J.*, **2000**, 78, 1578.

159. M. Gonsalves, J. V. Macpherson, D. O'Hare, C. P. Winlove and P. R. Unwin, *Biochim. Biophys. Acta*, **2000**, 1524, 66.

160. R. C. Engstrom, M. Weber, D. J. Wunder, R. Burgess and S. Winquist, *Anal. Chem.*, **1986**, 58, 844.

161. R. C. Engstrom, T. Meaney, R. Tople and R. M. Wightman, *Anal. Chem.*, **1987**, 59, 2005.

162. F. Zhou, P. R. Unwin and A. J. Bard, *J. Phys. Chem.*, **1992**, 96, 4917.

163. R. D. Martin and P. R. Unwin, *J. Chem. Soc. Faraday Trans.*, **1998**, 94, 753.

164. R. D. Martin and P. R. Unwin, *Anal. Chem.*, **1998**, 70, 276.

165. P. R. Unwin and A. J. Bard, *J. Phys. Chem.*, **1991**, 95, 7814.

166. D. A. Treichel, M. V. Mirkin and A. J. Bard, *J. Phys. Chem.*, **1994**, 98, 5751.

167. C. Demaille, P.R. Unwin and A. J. Bard, *J. Phys. Chem.*, **1996**, 100, 14137.

168. F. Zhou and A. J. Bard, *J. Am. Chem. Soc.*, **1994**, 116, 393.

169. S. B. Basame and H. S. White, *J. Phys. Chem. B*, **1998**, 102, 9812.

170. B. R. Horrocks, M. V. Mirkin, D. T. Pierce, A. J. Bard, G. Nagy and K. Toth, *Anal. Chem.*, **1993**, 65, 1213.

171. B. R. Horrocks and M. V. Mirkin, *J. Chem. Soc. Faraday Trans.*, **1998**, 94, 1115.

172. C. E. M. Berger, B. R. Horrocks and H. K. Datta, *Electrochim. Acta*, **1999**, 44, 2677.

173. G. Wittstock and W. Schuhmann, *Anal. Chem.*, **1997**, 69, 5059.

174. H. Sakai, R. Baba, K. Hashimoto and A. Fujishima, *J. Electroanal. Chem.*, **1994**, 379, 199.

175. K. Ikeda, H. Sakai, R. Baba, K. Hashimoto and A. Fujishima, *Chem. Lett.*, **1995**, 979.

176. H. Maeda, K. Ikeda, K. Hashimoto, K. Ajito, M. Morita and A. Fujishima, *J. Phys. Chem. B*, **1999**, 103, 3213.

177. S. K. Haram and A. J. Bard, *J. Phys. Chem. B*, **2001**, 105, 8192.

178. T. J. Kemp, P. R. Unwin and L. Vincze, *J. Chem. Soc. Faraday Trans.*, **1995**, 91, 3893.

179. A. Mills and S. Morris, *J. Photochem. Photobiol. A: Chem*, **1993**, 70, 183.

180. P. James, N. Casillas and W. H. Smyrl, *J. Electrochem. Soc.*, **1996**, 143, 3853.

181. R. Peat, A. Riley, D. E. Williams and L. M. Peter, *J. Electrochem. Soc.*, **1989**, 136, 3352.

182. G. Shi, L. F. Garfias-Messias and W. H. Smyrl, *J. Electrochem. Soc.*, **1998**, 145, 2011.

CHAPTER 2

EXPERIMENTAL

This chapter surveys the experimental techniques employed in the studies described in this thesis. Details are given of the fabrication of UMEs, the apparatus and procedures for general electrochemical and SECM measurements, and the solutions and chemicals used. The preparation and surface characterisation of a thin TiO_2 film are also covered.

2.1 Microelectrode Fabrication Procedures

2.1.1 Glass Coated Microdisc Electrodes

Glass coated microdisc electrodes of 25 μm diameter were prepared by the following procedure.[1,2,3] A borosilicate glass capillary (2 mm outer diameter, 1.16 mm inner diameter, Clark Electromedical Instruments, Reading) was drawn to a fine tip using a gravity-operated, vertically mounted pipette puller (model PB7, Narishige, Tokyo, Japan). The capillary tip was then cut to the desired length and sealed in the flame of a Bunsen burner. A 10 mm length of platinum or silver wire of 25 μm diameter (Goodfellow, Cambridge) was then placed in the tip end of the capillary and the air was pumped out using a vacuum pump for at least 15 minutes.

Under reduced pressure a resistively heated (20 V *ac* applied) nichrome wire coil (Annealed Ni80Cr20, 0.75 mm diameter, Goodfellow) was used to heat evenly the tip of the capillary. The result of this was to seal the wire in the glass with the exclusion of air bubbles, which may compromise the electrode response.

Electrical contact to the sealed wire was achieved by first inserting a slug of solder (60:40 tin:lead alloy, RS Components), and then a tinned copper wire (RS Components) into the capillary. The solder, which served as a contact between the metal electrode and the copper wire, was melted by placing the tip of a hot (440 °C) soldering iron against the outside of the capillary. The connecting wire was secured using Araldite Rapid (Ciba-Geigy, Cambridge). Figure 2.1 shows a schematic diagram of the completed electrode.

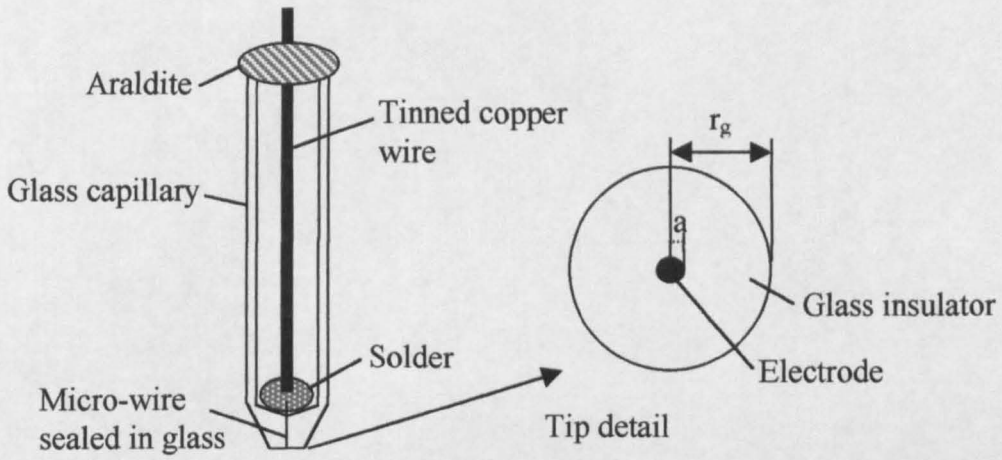

Figure 2.1 Schematic diagram of a glass sealed microdisc electrode.

The electrode was polished flat using a 600 grit polishing pad (Buehler, Coventry) until the wire was exposed. The required tip geometry was achieved by polishing the tip into a cone shape using the 600 grit polishing pad. This stage is crucial in the production of SECM UMEs, requiring the fabrication of a flat, planar electrode plus surrounding insulating glass surface, characterised by an RG = r_g/a value of *ca.* 10. Final polishing of the electrode using 0.05 μm alumina (Buehler) on a wet polishing cloth (Kemet, Maidstone) yielded smooth electrode surfaces. The RG value and smoothness were determined by optical microscopy

using an Olympus BH2 light microscope. Electrodes were polished with 0.05 μm alumina before each use.

2.1.2 Ag/AgCl microelectrodes

Ag/AgCl microelectrodes were obtained by chloridising a 25 μm diameter Ag microdisc electrode. The Ag electrode was coated with an AgCl film by slow anodic oxidation, in 0.1 mol dm^{-3} KCl, applying a potential of *ca.* 0.20 V vs. saturated calomel electrode (SCE, Radiometer Analytical S.A., Lyon, France).

Calibration curves of the measured electrode potential vs. chloride ion concentration were obtained by titrating 150 cm^3 KCl (0.1 mol dm^{-3}) into a 50 cm^3 solution of KNO_3 (0.1 mol dm^{-3}), with solutions buffered to pH 7.[4] The calibrating solution was stirred continuously with a magnetic stirrer (Stuart Scientific) and the potentials across the Ag/AgCl electrodes were recorded against SCE using a voltmeter (23XT, Wavetek Ltd., UK). The Ag/AgCl microelectrodes were calibrated with chloride concentrations between 10^{-5} and 10^{-1} mol dm^{-3}. A Nernstian relationship between the potential and the chloride ion concentration was observed from 10^{-4} to 10^{-1} mol dm^{-3}, with a gradient of 55 ± 1 mV per decade change in chloride. A typical calibration curve is shown in Figure 2.2.

2.2 Apparatus and Instrumentation

2.2.1 Electrochemical Measurements

UME voltammetry and amperometry measurements were made using a two-electrode set-up, with the microelectrode operating as the working electrode and a silver wire (Goodfellow) as a quasi-reference electrode (AgQRE). The UME potential was controlled with a purpose-built triangular wave/pulse

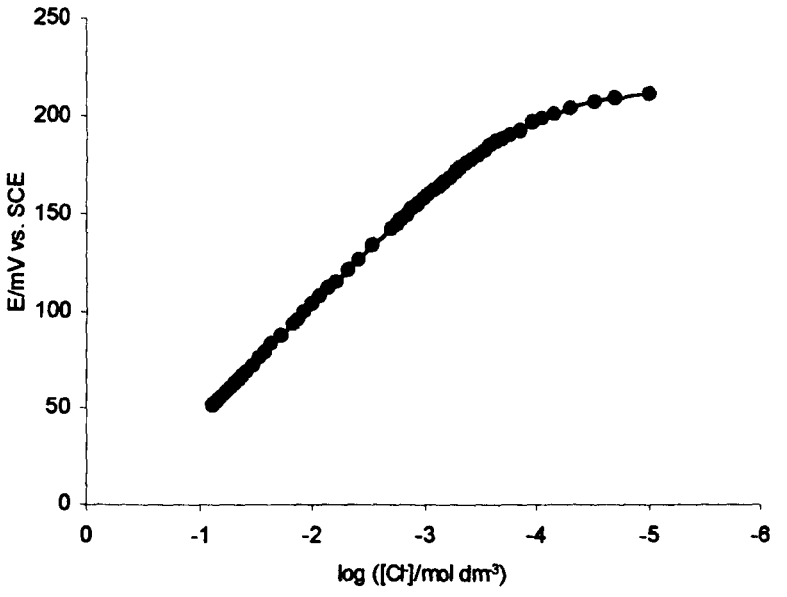

Figure 2.2 Calibration curve of potentiometric response vs. log [Cl^-] for an Ag/AgCl UME (a = 12.5 μm). The linear portion exhibits Nernstian behaviour from 10^{-4} – 10^{-1} mol dm^{-3}, with a slope of 55 mV per 10-fold change in [Cl^-].

generator (Colburn Instruments) and the current was measured using a home-built current follower (gains 10^{-5} to 10^{-9} A/V). The current-potential behaviour (voltammogram) and chronoamperometric characteristics were recorded through a data acquisition card (NI-DAQ Lab PC card, National Instruments, Austin, TX, USA) on a personal computer using home-written software (written by Dr. N. J. Evans in Microsoft Quick Basic).

Potentiometric measurements employed an Ag/AgCl microelectrode as the indicator electrode and a saturated calomel reference electrode. The potentials were determined using a voltage follower, built in-house, and recorded with the PC.

2.2.2 Non-electrochemical Techniques

Visual inspections of the UMEs, optical fibre and TiO_2 substrates were carried out using an Olympus BH2 light microscope (overall magnification × 50 to × 1000) equipped with a 3-CCD colour video camera (model KY-F55BE, JVC Professional, London, UK) coupled to a computerised data acquisition system (Image Grabber/PCI, Neotech, London, UK).

Interferometry measurements, to determine the thickness of the TiO_2 film, were made on a WYKO NT2000 Optical Profiler (Veeco Instruments, UK) in vertical scanning interferometry (VSI) mode, using a white light source.

Spectrophotometric experiments were performed using a JASCO V – 550 UV/VIS spectrophotometer coupled to a personal computer.

Chronoamperometric measurements in the millisecond range were performed using a Nicolet 310 oscilloscope (Madison, WI, USA).

2.3 SECM Set-up

The electrochemical cell consisted of a fully detachable Teflon base, cylindrical glass body and Teflon lid, with a total volume of about 25 cm^3. The cell base contained two holes: a central hole, through which a glass capillary containing a TiO_2-coated optical fibre could be secured vertically, and a drain. The optical fibre was an all-silica sensor grade fibre (F-MCC-T, Newport) with a core diameter of 200 μm surrounded by a concentric cladding and polyimide coating producing a total diameter of 250 μm. A piece of optical fibre (*ca.* 2 m long) was secured into a pulled glass capillary with Araldite Rapid in such a way that one end of the fibre (*ca.* 3 mm) emerged through the pulled end of the capillary. The fibre tip was then polished on a polishing wheel using a series of

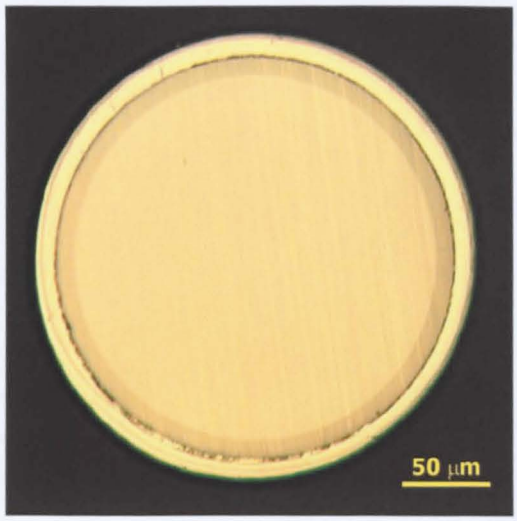

Figure 2.3 Optical micrograph of the polished surface of the optical fibre.

polishing pads (15, 9, 6, 3, 1 μm, Buehler, Ultra-prep Diamond lapping discs) until a flat, smooth fibre surface was obtained. An optical micrograph of the polished surface of a fibre is shown in Figure 2.3. To image the light intensity profile through the optical fibre a 20 μm stainless steel pinhole (N52-869, Edmund Scientific Ltd., UK) was mounted on a photodiode (N54-037, Edmund Scientific Ltd., UK) which was secured in a cell base. Details of this experiment will be given in section 3.3.2. The coating of the surface of the optical fibre with TiO_2 will be described in the next section.

The cell body contained an optical window (30 mm diameter) so that video microscopy could be used to monitor the position of the UME relative to the optical fibre tip. The zoom microscope was equipped with a CCD camera attachment that offered a maximum on-screen resolution of 2.2 μm per pixel. The cell was mounted flat on an aluminium support, which was screwed onto a Newport CSD series bread board.

The position of the electrode in the x and y directions (parallel to the surface of the fibre) was controlled with sub-micrometre resolution by attaching the electrode to a set of x-y translation stages (M-015.00, Physik Instrumente, Waldbronn, Germany), comprising two dc-mike drives (M223.21, Physik Instrumente) with optical encoders (MT25, Heidenhain, Germany). A signal processor (C-852, Physik Instrumente) and a two-axis controller card (C-842.20, Physik Instrumente) were used to control the dc-mike drives. Sub-micrometre control in the z direction (normal to the surface of the fibre) was achieved using a piezoelectric positioner (piezoelectric element, P-173.07 and controller, P-267 / P-277, Physik Instrumente). The UME was mounted on the z axis piezo driver with an aluminium holder containing an adjustable screw and a Teflon collar around the screw. The x, y stages were controlled by a PC, which also controlled the piezo-positioner through a Lab-PC-1200 card (National Instruments, TX, USA), using software written in-house by Dr N. J. Evans. The stages were mounted on a vibrationally isolated bench and the cell shielded using a home-built Faraday cage.

A high-powered xenon lamp (Illuminator 6000, Eurosep Instruments, Cergy-Pontoise, France) was used as the source of UV irradiation. The determination of the light flux intensity will be considered in chapter 3. The light was focused using two UV fused silica plano-convex lenses (SPX016 and SPX031, Newport) and an infrared quartz filter filled with $CuSO_4$ solution was used to dissipate heat during irradiation. This also defined the wavelength range of the illumination source as between 200 and 800 nm. Interfacial photoelectrochemical reactions were driven by illuminating the TiO_2 coated surface from the back by placing the other end of the optical fibre in front of the

focuser, ensuring that maximum output of UV illumination reached the TiO_2 surface. A shutter was used to switch the light on and off and the timescale was 0.11 s. This value was determined from the transient shown in Figure 2.4, which was obtained with the pinhole – photodiode arrangement that will be described in section 3.3.2. A schematic of the experimental set-up is given in Figure 2.5 while Figure 2.6(a) and (b) show, respectively, a photograph of the experimental arrangement and a detail of the UME and optical fibre alignment.

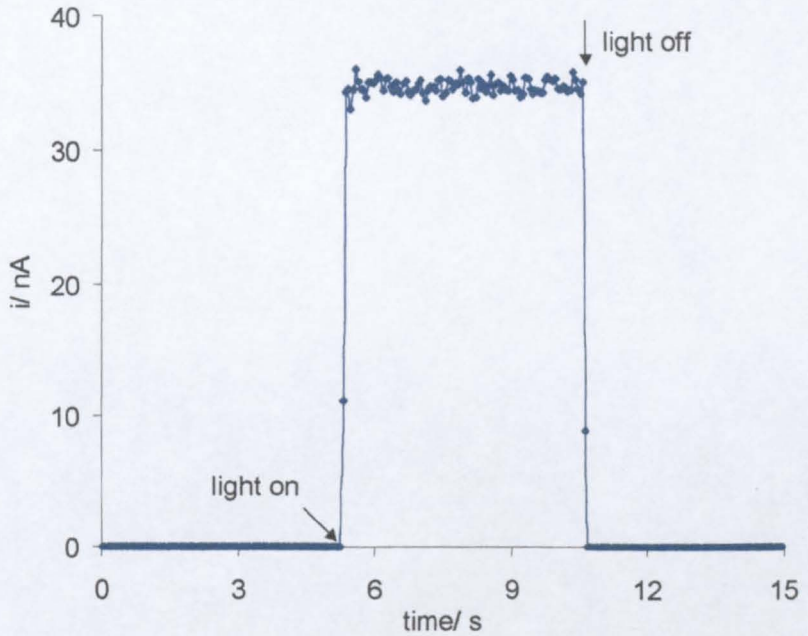

Figure 2.4 Chronoamperometric response of the photodiode after switching the illumination on and off with a shutter.

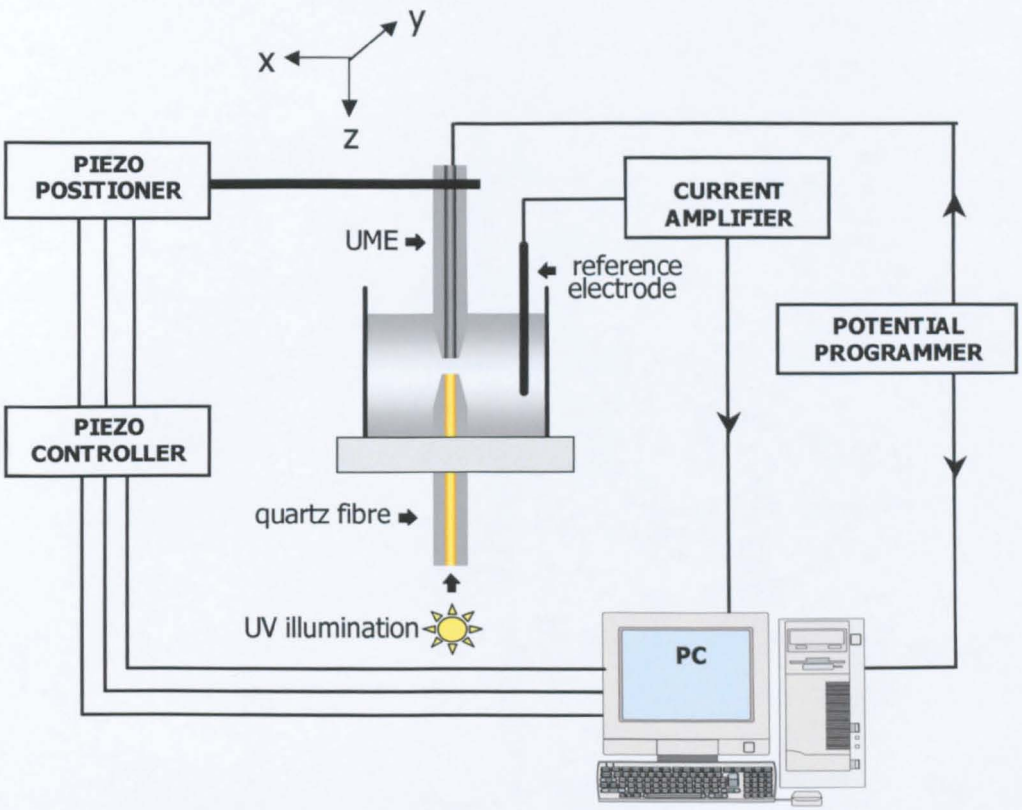

Figure 2.5 Schematic diagram of the SECM photoelectrochemical experimental set-up.

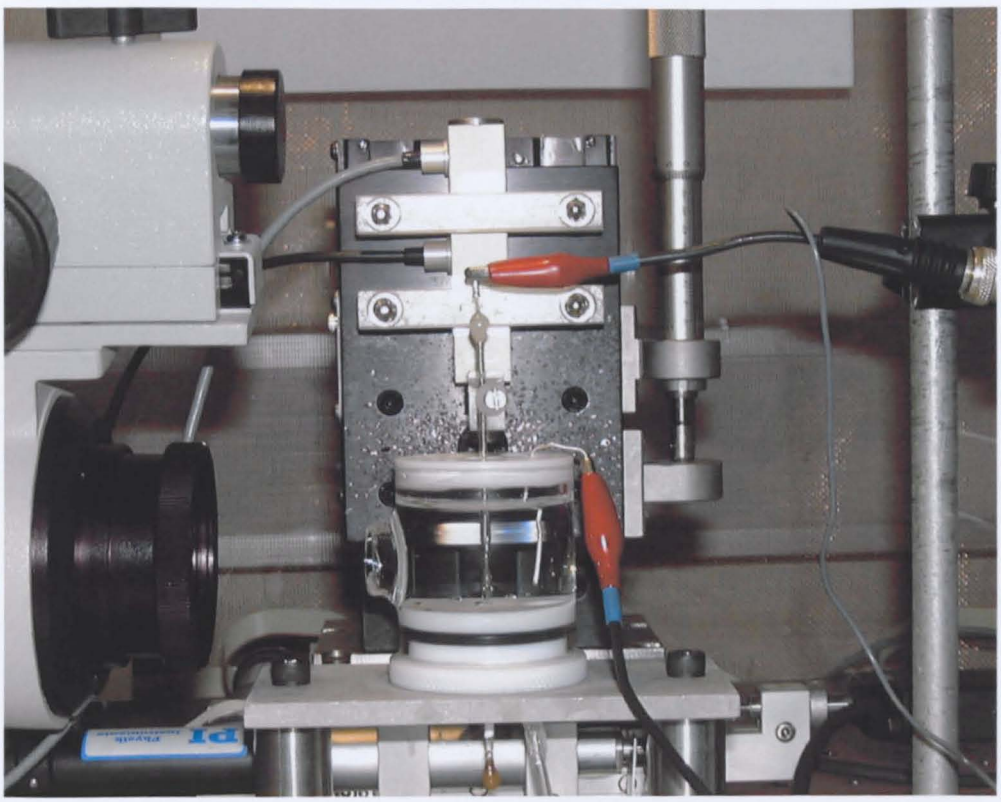

Figure 2.6(a) Photograph of the SECM experimental set-up.

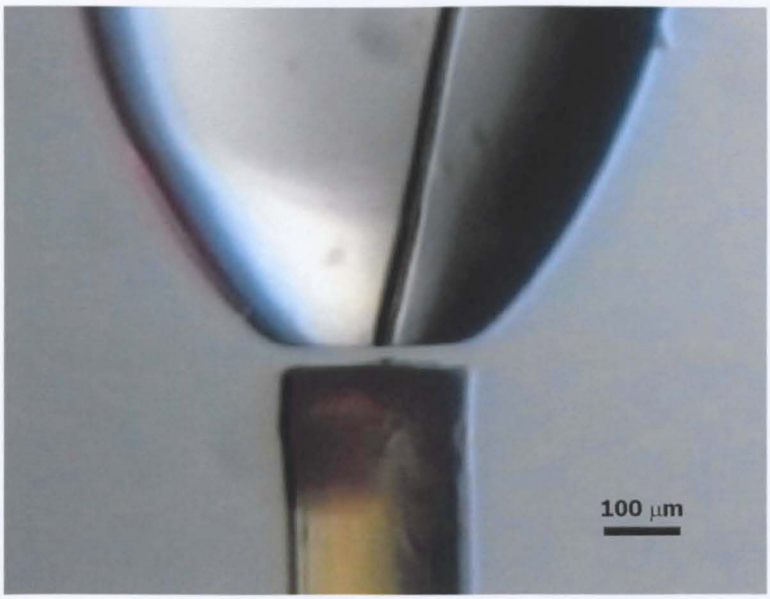

Figure 2.6(b) Optical micrograph showing the alignment of the UME and optical fibre.

2.4 Preparation and Characterisation of a Thin TiO_2 Film

The TiO_2 film was prepared from a 14% suspension of Degussa P25 TiO_2 powder, where 0.7 g of TiO_2 was mixed with 5 cm^3 Milli-Q reagent water (Millipore Corp., resistivity ≥ 18 MΩ cm), sonicated for 1 hr. using a sonicator (Decon F 5200b) and stirred for 3 hrs. with a magnetic stirrer (Janke and Kunkel IKA Labortechnik). The optical fibre was coated with the TiO_2 suspension with the aid of a paintbrush until an even, complete coating was achieved. The TiO_2 film was dried in an oven at 100°C for 12 hrs. resulting in a mechanically stable film. A typical optical micrograph, taken using an Olympus BH2 microscope, is shown in Figure 2.7. It is apparent from the Figure that the TiO_2 coating covers the entire surface area with a fairly flat and compact film on which to perform SECM measurements.

The thickness of the TiO_2 film was assessed by interferometry. Half of the TiO_2 coating was removed from the fibre and an interferometry measurement was performed. The sample was scanned in VSI mode over 20 μm in the *z* direction at

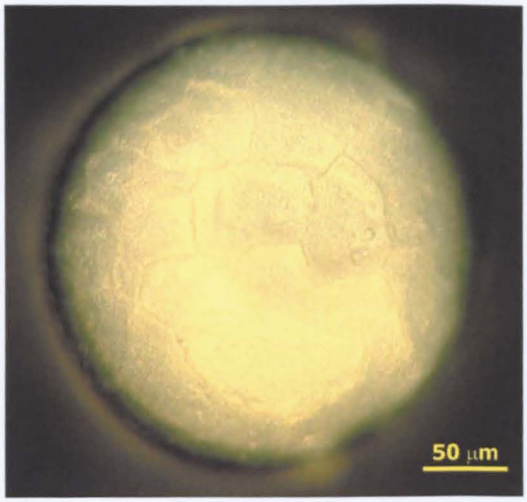

Figure 2.7 Optical micrograph of the TiO_2 coated fibre surface.

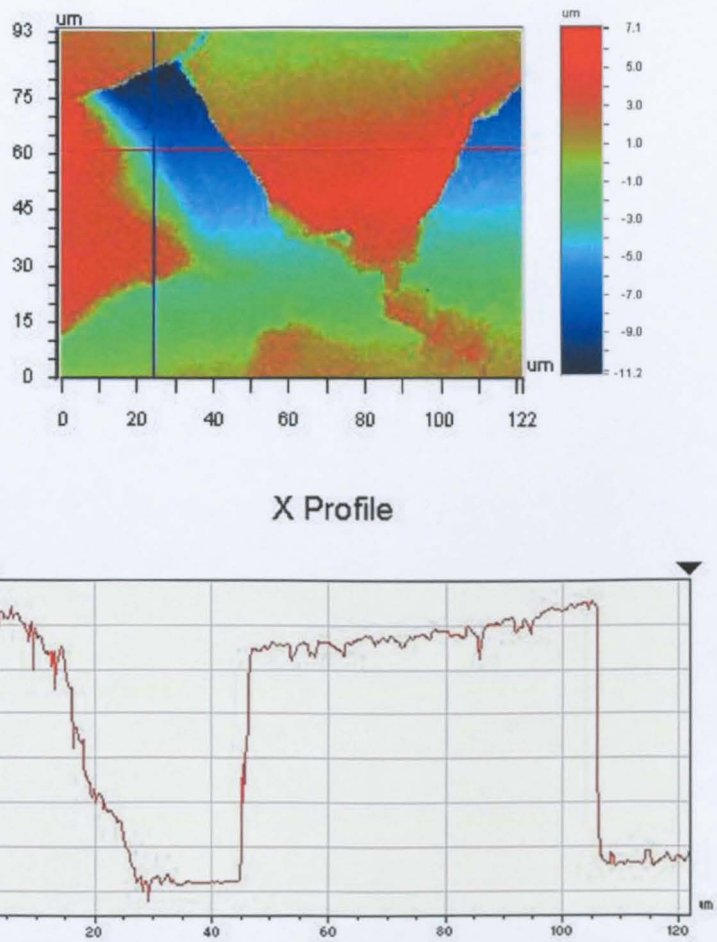

Figure 2.8 Interferometry map of a partially coated area of the optical fibre and TiO_2 film height across a linear portion in the *x*-direction.

a scan rate of 1 μm s^{-1}. Figure 2.8 shows the interferometry map obtained and a line profile which highlights height changes quantitatively. The TiO_2 films were typically found to be 12 ± 1 μm thick.

The transmittance spectra of a TiO_2 film of similar thickness was also performed and is given in Figure 2.9. The light with wavelengths below 400 nm is absorbed by the TiO_2 film as expected. For many of the studies that follow later in this thesis, particularly chlorophenol solutions, this means that direct photolysis is not problematic.

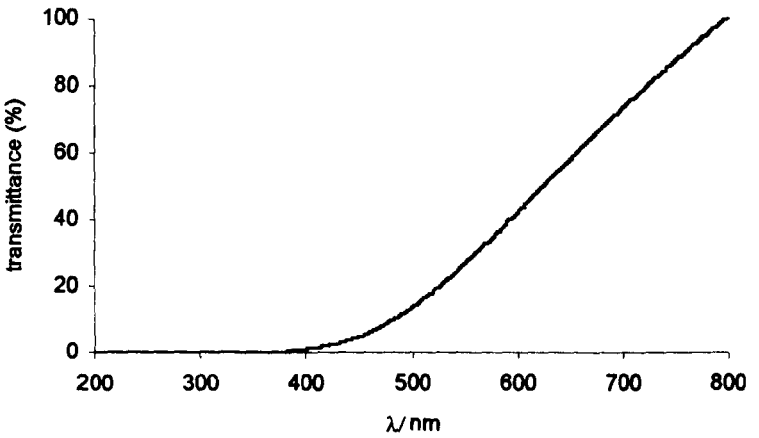

Figure 2.9 Transmittance spectra of a TiO_2 film.

2.5 Solutions and Chemicals

All solutions were prepared using Milli-Q reagent water (Millipore Corp., resistivity ≥ 18 MΩ cm). The grades and suppliers of the chemicals employed are identified in Table 2.1. The compositions of the solutions used will be outlined in the text in the chapters that follow. Solutions were prepared freshly each time immediately prior to use. Particular care was taken when preparing the potassium ferrioxalate solutions to avoid any reduction of ferrioxalate caused by the room

light. The solutions were prepared under ambient conditions, and the measurements were made at room temperature (23 ± 1°C).

Solution pH was measured using a pH meter (Radiometer, model PHM-201, with pH electrode PHC-3005-8), calibrated with appropriate buffers (pH 4 citrate buffer, pH 7 phosphate buffer and pH 10 carbonate buffer, Radiometer Analytical S.A.).

Table 2.1 Chemical grades and suppliers.

Chemical	Grade	Supplier
4-chlorophenol	99%	Aldrich
Methyl viologen dichloride	98%	Aldrich
Nitrogen	99.9%	BOC
Oxygen	99.9%	BOC
Oxygen	50% O_2 / N_2	BOC
Potassium chloride	Analar	BDH
Potassium nitrate	Analar	BDH
Potassium trioxalatoferrate(III)	Analar	Johnson Matthey
Sodium acetate	Analar	Fisher Scientific
Sodium perchlorate	99.99%	Aldrich
Sulfuric acid	98%, S.G. 1.84	Fisher Scientific
TiO_2	Anatase:rutile, 70:30	Degussa AG
Triethanolamine	98%	Aldrich

References

1. J. V. Macpherson, PhD Thesis, University of Warwick, 1996.

2. A. J. Bard, F.-R. Fan and M. V. Mirkin in *Electroanalytical Chemistry*, vol. 15, A. J. Bard (Ed.), Marcel Dekker, New York, 1994, 267.

3. C. Lee, C. J. Miller and A. J. Bard, *Anal. Chem.*, **1991**, 63, 78.

4. N. J. Gray and P. R. Unwin, *Analyst*, **2000**, 125, 889.

CHAPTER 3

A MICROELECTROCHEMICAL ACTINOMETER FOR SCANNING ELECTROCHEMICAL MICROSCOPY STUDIES OF PHOTOCHEMICAL PROCESSES

A new *in situ* photoelectrochemical approach to chemical actinometry has been developed and used to determine the light flux through a quartz fibre employed in the scanning electrochemical microscopy (SECM) system developed for studying the kinetics of interfacial photochemical processes. In this system an ultramicroelectrode (UME) probe is positioned with high precision at a known distance close to a TiO_2-coated fibre and used to detect reactants or products of the ongoing photodegradation process. The microelectrochemical actinometry approach was developed using the well-known liquid phase potassium ferrioxalate actinometer in order to quantify the light flux through the quartz fibre. The approach involves recording the steady-state current for Fe(III) at an SECM tip positioned close to the fibre. A step function in the light flux (off-on) is then applied and the resulting chronoamperometric behaviour due to the reduction of Fe(III) at the 25 μm diameter Ag UME is recorded as a function of tip-fibre separation distance. A theoretical model has been developed to simulate experimental current-time profiles, which enabled measurements of the light flux initiating the photoprocess.

3.1 Introduction

An important step in studying any photoprocess involves an accurate actinometry study. Hitherto, several photochemical actinometry systems (both gas

and liquid phase)[1] have been explored but, to date, potassium ferrioxalate, $[K_3Fe(C_2O_4)_3]$ actinometry, developed by Hatchard and Parker,[2] has received most attention as the best solution phase chemical actinometer. When an aqueous solution of ferrioxalate in sulphuric acid is photolysed in the range from 250-577 nm, the Fe(III)-complex undergoes reduction producing an Fe(II)-complex according to the following stoichiometry:[1]

$$\left[Fe^{III}(C_2O_4)_3\right]^{3-} \xrightarrow{h\upsilon} \left[Fe^{II}(C_2O_4)_2\right]^{2-} + C_2O_4^{-} \qquad (3.1)$$

$$\left[Fe^{III}(C_2O_4)_3\right]^{3-} + C_2O_4^{-} \rightarrow \left[Fe^{III}(C_2O_4)_3\right]^{2-} + (C_2O_4)^{2-} \qquad (3.2)$$

$$\left[Fe^{III}(C_2O_4)_3\right]^{2-} \rightarrow \left[Fe^{II}(C_2O_4)_2\right]^{2-} + 2CO_2 \qquad (3.3)$$

The overall stoichiometry indicates that for every Fe(III) ion lost, there is a corresponding gain of one Fe(II) ion. The Fe(II) produced is then detectable as Fe(II)-phenanthroline complex at 510 nm, using visible absorption spectroscopy. Details of this process have been described elsewhere.[2]

The SECM system developed employs a quartz fibre which is used to back-illuminate a thin TiO_2 film, deposited from a colloidal suspension. The experiments that will be performed require an accurate knowledge of the light flux intensity delivered though the optical fibre, however the widely used conventional photochemical system of ferrioxalate actinometry[1] was found to be unsuitable for such a microscopic scale approach. Thus a microelectrochemical actinometer system has been developed in which the chronoamperometric behaviour resulting from the disappearance of $Fe(C_2O_4)_3^{3-}$ following illumination was monitored in real time *via* the reduction of Fe(III) at the tip UME, placed with high precision above the fibre surface.

Ferrioxalate actinometry has usually been employed in batch photoreactors, but a recent study of this actinometry system utilised a flow reactor with conventional spectrophotometric quantification.[3] An *in situ* photoelectrochemical approach, employing the ferrioxalate actinometer system, has also been developed and used to quantify the light flux in a channel flow cell.[4] Fujishima's group[5,6] have developed an electrochemical actinometry system using an azo monolayer film, which facilitates a simpler *in situ* measurement of the light flux in photochemical and photoelectrochemical systems.

The aim of the work described in this chapter is to devise a straightforward *in situ* electrochemical actinometer system, capable of determining the absolute output available from the UV-source, using an SECM set-up.

3.2 Theory

In the SECM-ferrioxalate actinometry system, a 'step function' (off-on) in the light flux through the fibre was applied and the change in hindered diffusion current for Fe(III) reduction (initially at steady-state) was monitored. This process is modelled theoretically considering the appropriate SECM configuration as shown in Figure 3.1.

For the SECM theoretical model, it is necessary to define the diffusion of the Fe(III) complex in the SECM geometry. For this particular process the effect of light is to cause the homogeneous decomposition of Fe(III) to Fe(II), thus the following equation applies:

$$\frac{\partial c}{\partial t} = D\left(\frac{\partial^2 c}{\partial r^2} + \frac{1}{r}\frac{\partial c}{\partial r} + \frac{\partial^2 c}{\partial z^2}\right) - k(r,z)c \qquad (3.4)$$

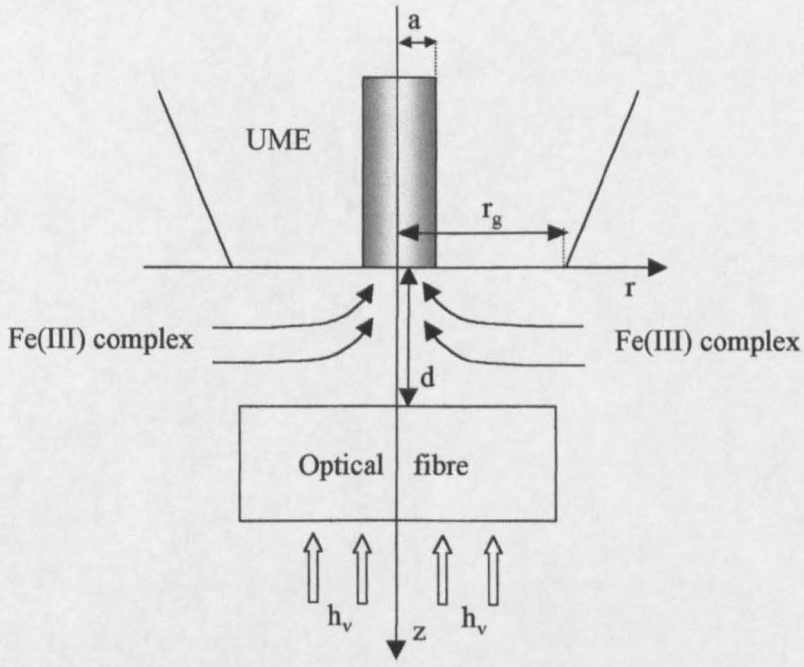

Figure 3.1 Schematic of the SECM configuration employed for the ferrioxalate actinometry study with the co-ordinate system used for the theoretical model. The co-ordinates r and z are measured from the centre of the UME in the radial and normal directions, respectively. The UME is characterised by an electrode radius a, and r_g is the distance from the centre of the electrode to the edge of the surrounding insulating glass sheath. The optical fibre is located at a distance d.

where c is the concentration of Fe(III), which has a diffusion coefficient D, and r and z are the radial and normal co-ordinates defining the axisymmetric cylindrical SECM geometry.[7] The rate coefficient $k(r,z)$ defines the light-induced decomposition process. In the dark this has the value zero and the problem amounts to the negative feedback simulation first described by Kwak and Bard.[8]

Upon illumination we have to recognise that the rate coefficient may depend on the r, z co-ordinate since the local light intensity, $I(r, z)$, affects the rate of decomposition process:

$$k(r,z) = I(r,z)\phi\,\varepsilon \tag{3.5}$$

where ϕ is the quantum yield for the photodecomposition process and ε is the molar extinction coefficient for potassium ferrioxalate. By carrying out SECM

measurements in a thin gap arrangement, $I(r, z)$ will be relatively invariant with z, and equivalent to the flux impinging at the quartz/aqueous interface, since there is only a small volume of solution to absorb the light. To simplify this further, we also initially assume that the intensity is uniform in r. Thus

$$I(r,z) \approx I_0 \tag{3.6}$$

where I_0 is the intensity of the incident light which we are attempting to measure.

Combining equations (3.4), (3.5) and (3.6), the following equation is obtained:

$$\frac{\partial c}{\partial t} = D\left(\frac{\partial^2 c}{\partial r^2} + \frac{1}{r}\frac{\partial c}{\partial r} + \frac{\partial^2 c}{\partial z^2}\right) - I_0 \phi \varepsilon c \tag{3.7}$$

This is the equation which was solved subject to the following boundary conditions:

$$0 < r \le a, z = 0 \qquad c = 0 \tag{3.8}$$

$$a < r \le r_g, z = 0 \qquad \frac{\partial c}{\partial z} = 0 \tag{3.9}$$

$$0 < r \le r_g, z = d \qquad \frac{\partial c}{\partial z} = 0 \tag{3.10}$$

$$r = 0, \ 0 < z < d \qquad \frac{\partial c}{\partial r} = 0 \tag{3.11}$$

$$r = r_g, \ 0 < z < d \qquad c = c^* \tag{3.12}$$

where c^* is the bulk concentration. The light flux is initially zero and then stepped to a value I_0 at $t = 0$.

The problem can be cast into dimensionless form using the following equations:

$$\tau = \frac{tD}{a^2} \tag{3.13}$$

$$Z = z/a \tag{3.14}$$

$$R = r/a \tag{3.15}$$

$$K' = \frac{I_0 \phi \varepsilon a^2}{D} \tag{3.16}$$

$$C = c/c^* \tag{3.17}$$

The problem was solved using the ADI finite difference method.[7] For a given tip/substrate separation, this allowed the calculation of the current-time behaviour following illumination with a given K' value. If ε and ϕ are known, then K' allows I_0 to be calculated.

For the ferrioxalate system, ϕ is close to unity and ε depends on the wavelength range used. Thus using the mean value of ε, applicable to the wavelength range of interest, the light flux density was calculated.

In this model (model A) it was assumed that the light intensity was uniform in r, but as will be shown in section 3.3.2, that is not actually the case and a new model (model B) was developed to account for the non-uniformity of the light distribution across the fibre. A 10^{th} order polynomial equation $f(R)$ was fitted to the light intensity profile through the fibre, measured with a mobile pinhole-photodiode arrangement. In this case, K' in equation (3.16) is now given by

$$K' = \frac{I_0 \phi \varepsilon a^2}{D} f(R) \tag{3.18}$$

where R is the normalised distance.

3.3 Experimental Results and Discussion

3.3.1 Determination of the Molar Extinction Coefficient of the Ferrioxalate Complex

In order to determine the molar extinction coefficient, UV absorption spectra of solutions of the ferrioxalate complex were recorded over a concentration range of 6.0×10^{-4} – 1.8×10^{-3} mol dm^{-3} in 0.1 N H_2SO_4. The spectra were analysed in terms of the Beer-Lambert law:

$$A = \varepsilon c^* l \tag{3.19}$$

where A is the absorbance, ε is the molar extinction coefficient (M^{-1} cm^{-1}), c^* is the bulk concentration of the ferrioxalate solutions and l is the path length of the spectrophotometric cell.

The absorbance *vs.* concentration plots for the wavelength range 250-400 nm demonstrated the required linear dependence and the gradient of each plot yielded the molar extinction coefficient as a function of wavelength. Since the UV absorption characteristics of ferrioxalate strongly depend on the wavelength range of interest, ε was determined as a function of wavelength, as shown in Figure 3.2. A mean value of the molar extinction coefficient of 1.60×10^{6} mol^{-1} cm^2 was obtained and used to determine the light flux intensity. This is a reasonable approach, because the output of the UV lamp, reported elsewhere,[3] is fairly uniform over the wavelength range of Figure 3.2.

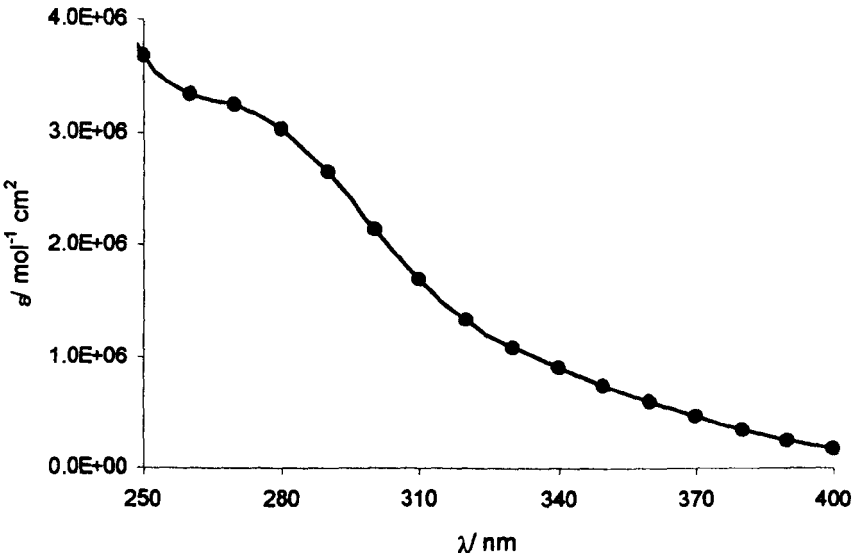

Figure 3.2 Dependence of the molar extinction coefficient for the ferrioxalate complex on wavelength.

3.3.2 Light Intensity Profile Through the Optical Fibre

The light intensity distribution through the optical fibre was imaged using a simple scanned probe approach. A 20 μm pinhole was mounted on a photodiode, which was secured in a cell base, and the fibre was scanned over it in the *x-y* plane, allowing the light intensity distribution to be imaged. For these experiments the SECM instrument was used, but with the photodiode replacing the UME probe. The photodiode converts the light intensity to current, which was measured using a home-built current follower. A typical contour plot obtained is shown in Figure 3.3. The light flux is non-uniform, but there is a relatively high intensity across most of the fibre area. The light intensity profile across the optical fibre is shown in Figure 3.4. An equation was fitted to this profile, which was then used in one of the models developed (model B).

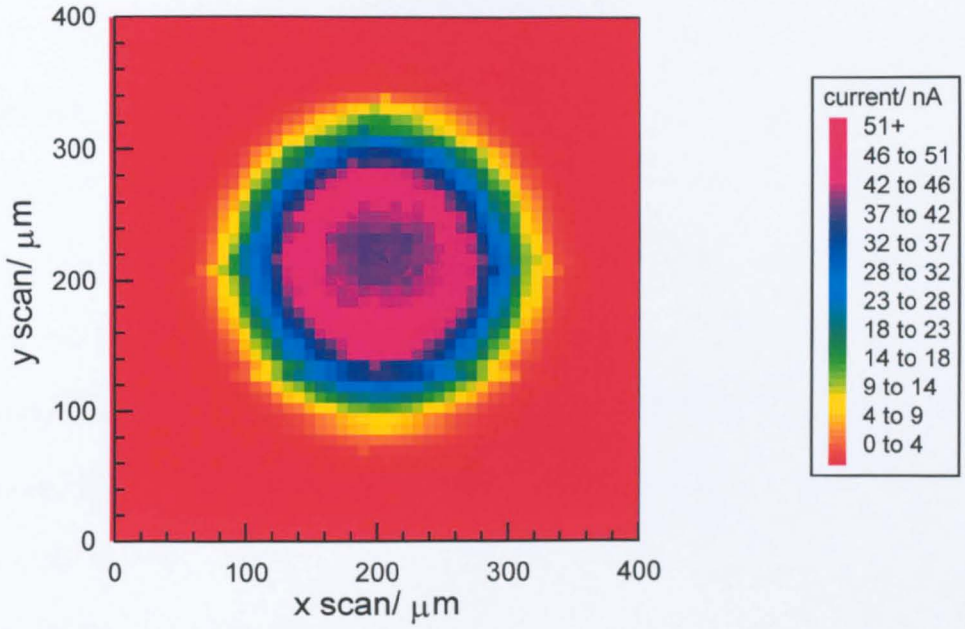

Figure 3.3 Contour plot showing the light intensity distribution through the optical fibre.

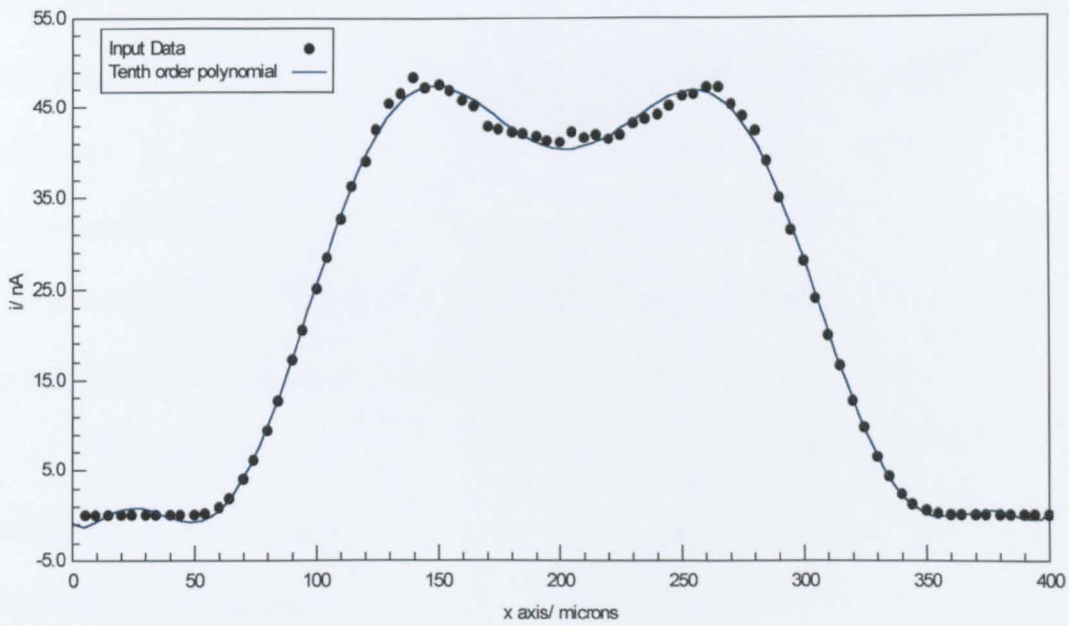

Figure 3.4 Light intensity profile across the fibre and fitted polynomial equation.

3.3.3 Electrode-Fibre Alignment Measurements

SECM imaging of the optical fibre in the dark *via* the reduction of potassium ferrioxalate was also performed, in order to precisely align the UME probe over the fibre. An aqueous solution of 6.0×10^{-3} mol dm^{-3} potassium ferrioxalate in 0.1 N H_2SO_4 was employed for this purpose, taking special care to avoid any reduction of ferrioxalate caused by the room light.[9] The solution was bubbled with nitrogen for 30 minutes and during measurements a gentle stream of nitrogen was passed over the solution surface. This effectively excluded oxygen from the solution, which would otherwise interfere with the electrochemical response for the reduction of Fe(III) at the tip electrode and would also affect the photolysis of ferrioxalate.[10]

The SECM tip (25 μm diameter Ag UME) was first carefully aligned normal to the surface of the optical fibre (in the z-direction), using the piezoelectric translation stages, at a distance $d > 10a$, where the diffusion-controlled limiting current, $i(\infty)$, should follow the diffusion-limited current equation for microdisc electrodes (equation 1.22). A current-potential voltammogram was recorded in bulk solution and is shown in Figure 3.5. From the limiting current, the diffusion coefficient of ferrioxalate was determined as D $= 5.25\times10^{-6}$ cm^2 s^{-1} using equation 1.22.

The tip was then moved close to the fibre surface to a distance $d < a$, where the diffusion-limited current became hindered. This indicated that negative feedback was achieved, which revealed the optical fibre to be an insulating substrate. The current allowed the tip-substrate separation to be readily obtained *via* the hindered diffusion theory of Kwak and Bard.[8] SECM images were obtained by holding the UME tip at a constant *z* position (normal to the fibre

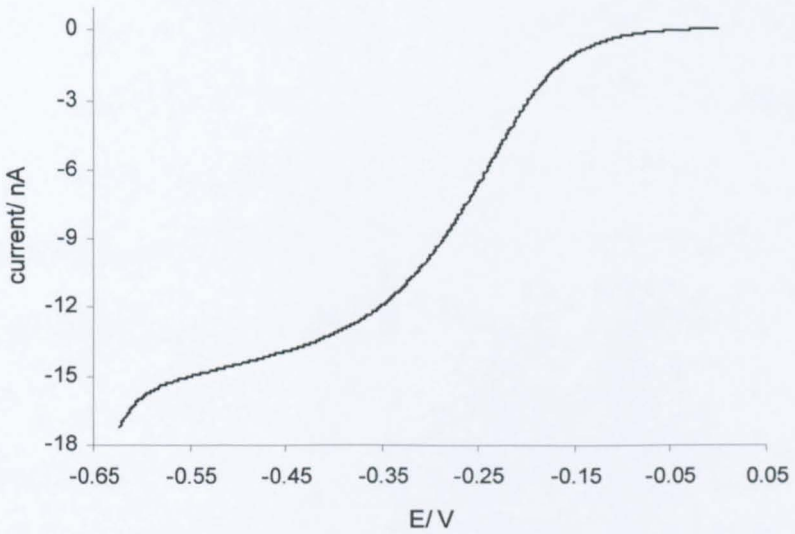

Figure 3.5 Steady-state voltammogram for the reduction of 6.0×10^{-3} mol dm^{-3} potassium ferrioxalate solution at a 25 μm diameter Ag UME.

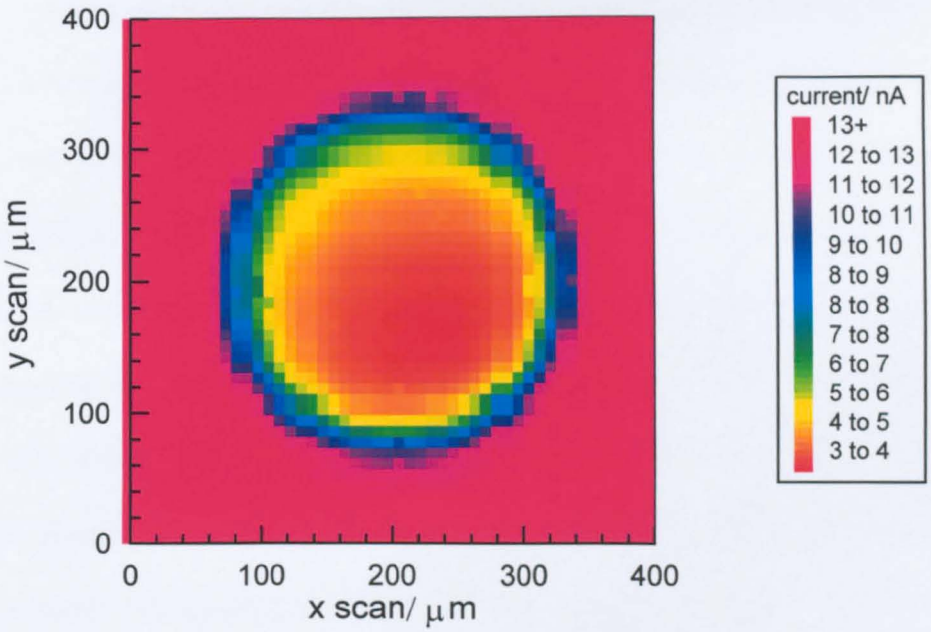

Figure 3.6 Contour plot showing the surface of an optical fibre obtained *via* SECM imaging of the reduction of potassium ferrioxalate, as described in the text.

surface) and scanning in the *x-y* plane (parallel to the fibre surface) over the area of interest. The tip was held at a potential of –0.55 V, sufficient to promote the diffusion-limited one-electron reduction of Fe(III). A typical contour plot obtained is shown in Figure 3.6. The edges of the fibre are readily defined because the current rises to the bulk solution value in this position. In this way, SECM imaging allowed the tip UME and the optical fibre to be aligned very precisely in the *x-y* plane, before subsequent chronoamperometric measurements.

3.3.4 Determination of the Light Flux Intensity

Chronoamperometric phototransients for the reduction of Fe(III) were recorded at the tip UME as a function of tip-substrate distance by holding the tip at a potential of -0.55 V, sufficient to allow the diffusion-limited reduction of Fe(III). After the tip current reached a steady-state (hindered diffusion) value in the dark, the light was suddenly switched on and the change in current with time was recorded. A typical transient for a tip-substrate separation distance of 5.4 μm (deduced from the steady-state limiting dark current[8]) is shown in Figure 3.7. As described, the current was first recorded in the dark and then the effect of stepping the light flux on and off was followed. When the UV-lamp was turned on, the current decreased because Fe(III) was consumed by photo-reduction to Fe(II) in the illuminated zone, thus depleting the flux of Fe(III) reaching the electrode. After a brief period of illumination (a few seconds), the reduction current tends to reach a plateau. The fact that this is non-zero means that the photolytic process occurs fairly slowly compared to the timescale of diffusion from the edge of the tip-substrate gap to the electrode. When the lamp was switched off, the current response at the UME promptly shifted back to the initial dark value, showing that

in the absence of light, Fe(III) in the tip-substrate domain is replenished by diffusion from the edge of the tip-substrate gap. These processes are illustrated schematically in Figure 3.8.

Experimental results such as the transient depicted in Figure 3.7 were compared with the best-fit theoretical simulations in order to measure the light flux intensity. The two theoretical models developed, the one that assumes that the light intensity distribution is uniform across the fibre (model A) and the one that assumes that the light intensity distribution is non-uniform (model B), were considered and are compared in Figure 3.9(a) and 3.9(b). For each case the normalised rate constant (K') was adjusted to achieve the best fit between the simulation and experiment. This allowed the light flux intensity (I_0) to be determined from the theoretical approach described in section 3.2. The K' values for the two models are fairly similar (within 5%) because, as can be seen in Figure 3.3, there is a relatively high (and uniform) intensity across most of the fibre area.

In Figure 3.10(a) and 3.10(b) experimental results at two other different tip-substrate distances are compared with the best fit theoretical simulations using model A. There is a better fit between the experimental data and the model simulation for the closest tip-substrate distance, but the K' values are fairly similar for the three distances and the mean value of the normalised rate constant was used to determine the light flux intensity. Using equation (3.16) and considering that the diffusion coefficient D for potassium ferrioxalate is 5.25×10^{-6} cm^2 s^{-1}, the extinction coefficient ε is 1.60×10^{6} mol^{-1} cm^2, the quantum yield ϕ for the photo-decomposition process is unity, the radius a of the UME is 12.5×10^{-4} cm and the normalised rate constant K' is 0.0345 for model A and 0.0355 for model B, the

light flux intensity I_0 was calculated and the values 4.36×10^{16} cm^{-2} s^{-1} and 4.49×10^{16} cm^{-2} s^{-1} were obtained for models A and B, respectively.

The light flux intensity was determined regularly to check the output from the xenon lamp. There was a slight decrease in intensity with utilisation period (*ca.* 2 years), and in the last actinometry performed the intensity had dropped to 1.79×10^{16} cm^{-2} s^{-1}.

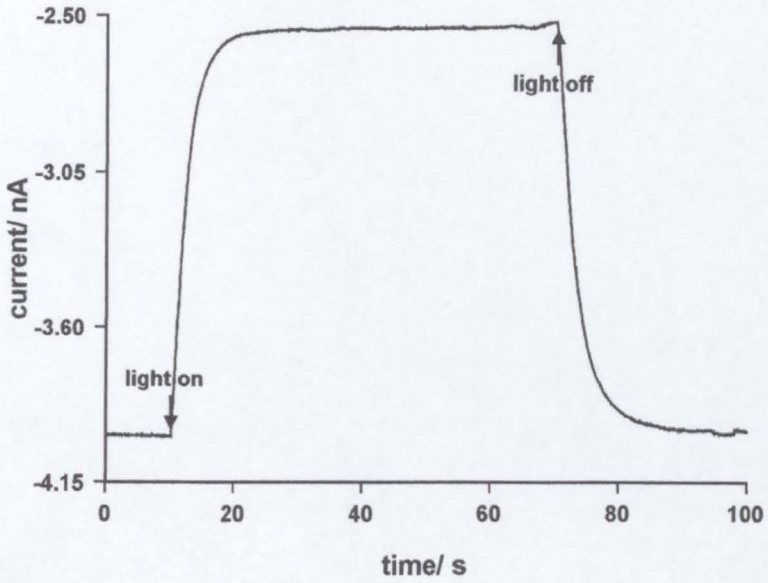

Figure 3.7 Chronoamperometric behaviour for Fe(III) photoelectrochemical reduction with the UME positioned 5.4 μm away from the optical fibre.

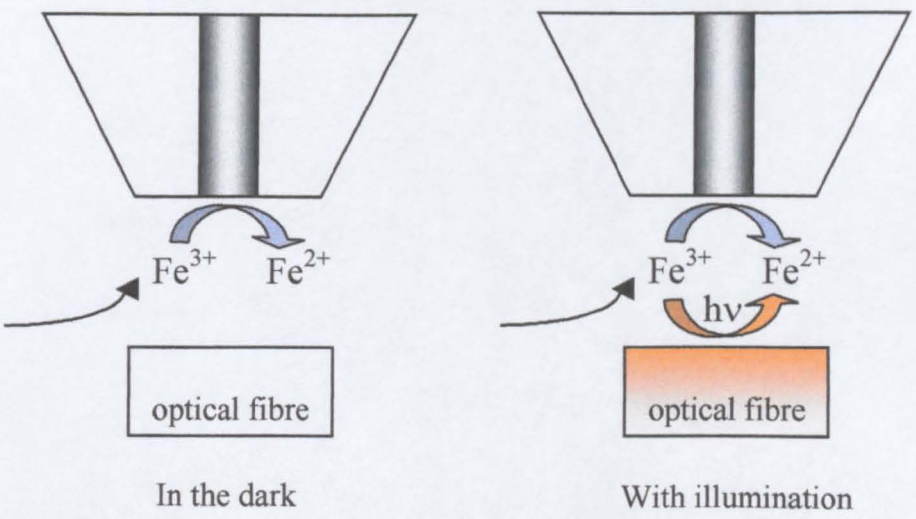

Figure 3.8 Schematic representation showing the reduction of potassium ferrioxalate at the tip UME.

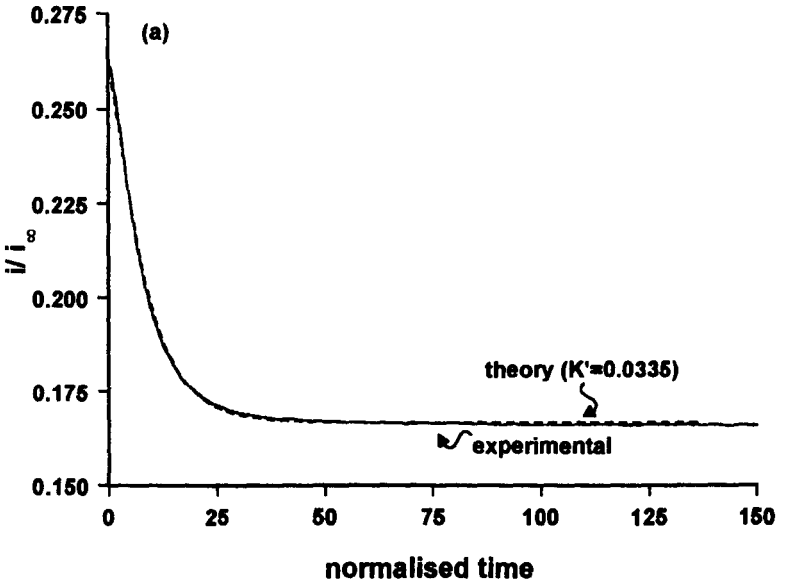

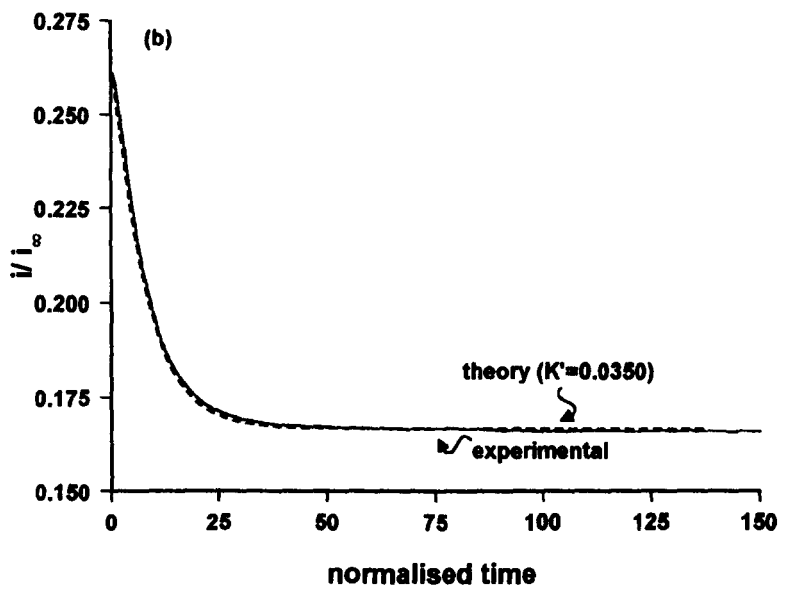

Figure 3.9 Normalised experimental data (normalised time = $t\,D\,/\,a^2$), after stepping the light on, for Fe(III) reduction compared with the best fit theoretical simulations for d = 5.4 μm using (a) model A and (b) model B.

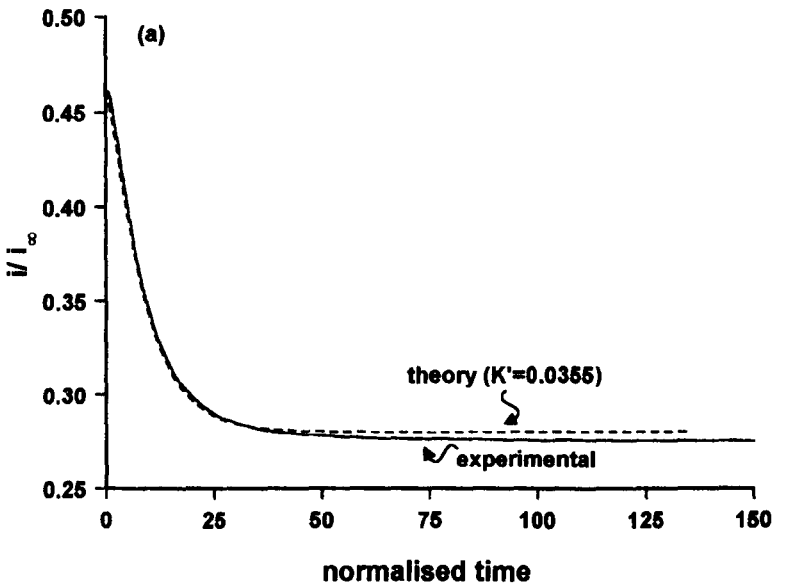

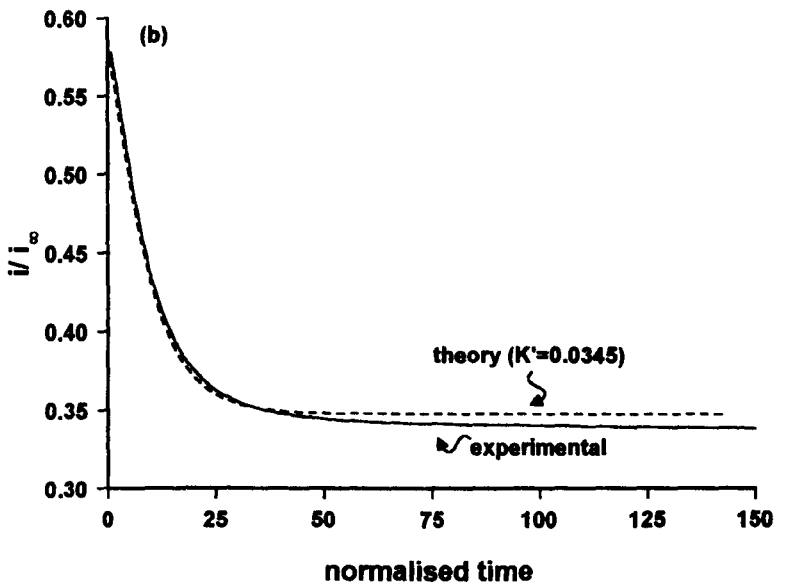

Figure 3.10 Normalised experimental data (normalised time = $t\,D\,/\,a^2$), after stepping the light on, for Fe(III) reduction compared with the best fit theoretical simulations using model A for (a) d = 10.3 μm and (b) d = 13.9 μm.

3.4 Conclusions

An SECM system has been developed to investigate the kinetics of photochemical processes at the microscopic level. An accurate knowledge of the light flux initiating the photoprocess is required, however the widely used conventional photochemical system of ferrioxalate actinometry was found to be unsuitable for such a microscopic scale approach, and thus a microelectrochemical actinometer system has been developed in which the chronoamperometric behaviour of the phototransients, due to the reduction of Fe(III), in the dark and light, were recorded at a 25 μm diameter Ag UME as a function of tip-fibre separation distance. A theoretical model has been developed to simulate experimental profiles, which enabled measurement of the light flux initiating the photoprocess. This *in situ* ferrioxalate microelectrochemical actinometer offers a new approach of investigating photoelectrochemical systems where the light flux on such a microscopic scale can be determined electrochemically.

References

1. J. F. Rabek, *Experimental Methods in Photochemistry and Photophysics*, Part 2, A Wiley – Interscience Pub, 1982.

2. C. G. Hatchard and C. A. Parker, *Proc. R. Soc. London, Ser. A*, **1956**, 235, 518.

3. L. Vincze, T. J. Kemp and P. R. Unwin, *J. Photochem. Photobiol., A: Chem.*, **1999**, 123, 7.

4. S. Ahmed, PhD Thesis, University of Warwick, 2000.

5. Z. F. Liu, K. Morigaki, K. Hashimoto and A. Fujishima, *Anal. Chem.*, **1992**, 64, 134.

6. K. Morigaki, Z. F. Liu, K. Hashimoto and A. Fujishima, *Ber. Bunsenges. Phys. Chem.*, **1993**, 97(7), 860.

7. P. R. Unwin and A. J. Bard, *J. Phys. Chem.*, **1991**, 95, 7814.

8. J. Kwak and A. J. Bard, *Anal. Chem.*, **1989**, 61, 1221.

9. G. Gauglitz and S. Hubig, *J. Photochem.*, **1981**, 17, 13.

10. C. A. Parker, *Trans. Faraday Soc.*, **1954**, 50, 1213.

CHAPTER 4

PHOTOELECTROCHEMICAL REDUCTION OF OXYGEN AT TiO_2 FILMS: KINETICS AND MECHANISM

This chapter describes how SECM has been used to monitor the photoelectrochemical reduction of oxygen at UV-illuminated TiO_2 surfaces. Oxygen plays a key role in photomineralisation processes catalysed by illuminated TiO_2. It acts as an electron scavenger in the photodegradation process following the reduction pathway and it can also participate in the photooxidation reactions. However, the kinetics and mechanism of the oxygen reduction reaction have not been investigated quantitatively at the microscopic level. Thus, a new approach to monitoring the photoelectrochemical reduction of oxygen was developed, in which the chronoamperometric behaviour for oxygen reduction was recorded at an UME tip after stepping the light flux at a TiO_2 film on and off. The kinetics of the reduction process are interpreted through various theoretical models proposed in the literature.

4.1 Introduction

A key point in mechanistic studies of TiO_2-sensitised photomineralisation processes concerns the role of oxygen. It has been the focus of attention in theoretical and experimental studies under steady-state conditions,[1,2,3] periodically illuminated systems[4] and electrochemically-assisted photocatalysis.[5] Oxygen acts as an electron scavenger, reducing the electron-hole recombination rate, and there is also evidence that activated oxygen species ($O_2^{\bullet-}$ and $HO_2^{\bullet}$) and molecular oxygen are involved in the oxidation reaction pathway.[6,7,8] Theoretical studies by

Gerischer and Heller[1,2] have suggested that the rate of electron transfer from TiO_2 to oxygen may be slow compared to the electron-hole pair generation rate, and that the interfacial electron transfer could be the rate limiting step in photocatalysis. However, while there is experimental evidence for this,[3] other investigations have suggested that electron transfer to oxygen is not rate limiting in photocatalytic degradation processes.[9,10]

An alternative approach to evaluating the rate limiting step in TiO_2 photocatalysis was the application of a flux-matching condition by Lewis and co-workers.[11] The overall rate of the interfacial process was considered to be predetermined by the fact that at steady-state, the flux of holes across the solid/liquid interface must be balanced by an equivalent flux of electrons. Using single crystal TiO_2 photoelectrodes, Lewis and co-workers compared the magnitudes of photooxidation current densities for aqueous solutions in the absence of oxygen, to oxygen reduction current densities in air-saturated solutions. The data successfully explained why recombination in TiO_2-sensitised photomineralisation might be significant, but the authors also cautioned against extending the data obtained on TiO_2 single crystals to particulate systems.

The aim of this chapter is to determine the kinetics of oxygen reduction in a particulate TiO_2 film, at the microscopic level, using SECM. The new approach developed in this study employs a microelectrode to amperometrically monitor the reduction of oxygen at illuminated TiO_2 surfaces.

4.2 Electrochemistry of Oxygen Reduction

The mechanism and kinetics of the cathodic reduction of oxygen have been widely studied on many electrode materials and the literature discussing the

reaction is extensive.[12,13,14,15] There is general consensus that the reaction occurs by a series of parallel reaction pathways,[16] which are shown in Figure 4.1. The direct reduction results in the formation of H_2O (in acidic medium) or OH^- (in alkaline solution) *via* a single four-electron process (Equations 4.1 and 4.2), while the indirect reduction occurs in two two-electron steps to produce H_2O (Equations 4.3 and 4.4) or OH^- (Equations 4.5 and 4.6).

$$O_2 + 4H^+ + 4e^- \rightarrow 2H_2O \quad (4.1)$$

$$O_2 + 2H_2O + 4e^- \rightarrow 4OH^- \quad (4.2)$$

$$O_2 + 2H^+ + 2e^- \rightarrow H_2O_2 \quad (4.3)$$

$$H_2O_2 + 2H^+ + 2e^- \rightarrow 2H_2O \quad (4.4)$$

$$O_2 + H_2O + 2e^- \rightarrow HO_2^- + OH^- \quad (4.5)$$

$$HO_2^- + H_2O + 2e^- \rightarrow 3OH^- \quad (4.6)$$

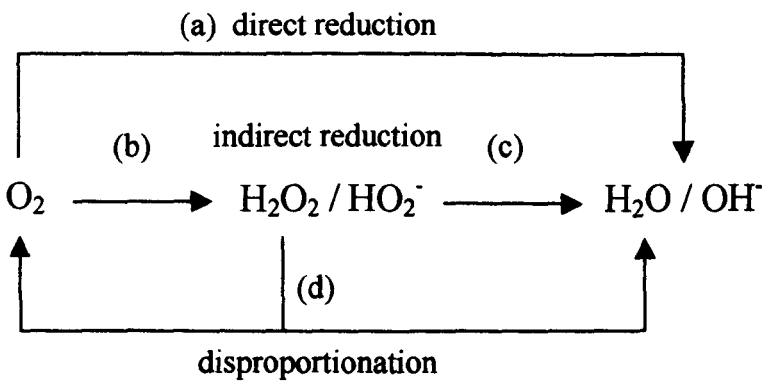

Figure 4.1 Schematic representation of the oxygen reduction pathways.

Pletcher and Sotiropoulos[16,17] investigated the cathodic reduction of oxygen in neutral and basic aqueous electrolyte solutions, as well as in purified water and other media of low ionic strength, employing a Pt rotating-disc

electrode and Pt, Ag and Au UMEs. They found that at Ag and Au microelectrodes the limiting currents, calculated using Equation 1.22, were proportional to the disc radius as expected for a simple $4e^-$ reduction. However, at Pt the value of n (number of electrons transferred), estimated from the limiting currents, was found to decrease at the smaller microdiscs and at a 5 μm radius electrode, $n \approx 3$. It was proposed that the variation in the limiting current arises because the reduction of oxygen at Pt occurs in $2 \times 2e^-$ steps, which occur at similar potentials, but are separated by a relatively fast chemical step (most likely, protonation of HO_2^-). In these circumstances, the $2e^-$ product will tend to escape from the electrode under conditions of rapid mass transport, *i.e.* at small microelectrodes, but the full $4e^-$ reduction will otherwise be observed.

4.3 Theory

4.3.1 Development of Mechanistic Models for the Photoelectrochemical Reduction of Oxygen

Following the basic idea demonstrated by Lewis and co-workers,[11] the surface electron and hole processes are considered in terms of the simplified schematic shown in Figure 4.2.

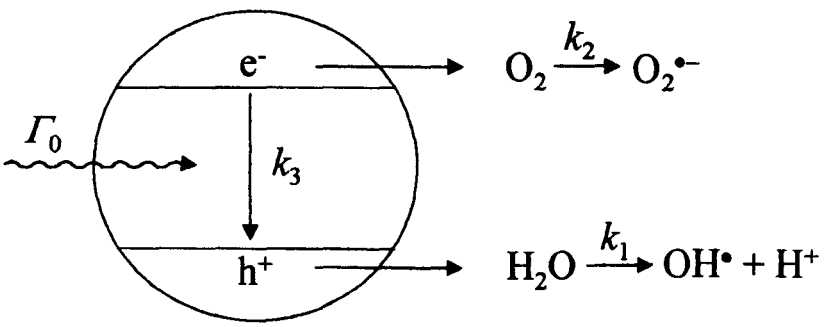

Figure 4.2 Schematic representation of surface electron and hole processes in a TiO_2 particle.

Expressions for electron and hole concentrations, under steady-state conditions, can be obtained by writing the flux of electrons transferred to oxygen as the product of the electron concentration, (e^-), the oxygen concentration close to the TiO_2/aqueous interface, $[O_2]_i$, and the rate constant for interfacial electron transfer, k_2; writing the flux of holes being transferred to water as the hole concentration, (h^+), multiplied by the rate constant for interfacial hole transfer, k_1; and by writing the flux of electrons and holes that recombine in the particle as a bimolecular process with a rate constant k_3. Thus, at steady-state, the balances for the photogenerated electrons, e^-, and holes, h^+, are given by:

$$\frac{d(e^-)}{dt} = 0 = \Gamma_0 - k_2(e^-)[O_2]_i - k_3(e^-)(h^+) \tag{4.7}$$

$$\frac{d(h^+)}{dt} = 0 = \Gamma_0 - k_1(h^+) - k_3(e^-)(h^+) \tag{4.8}$$

and

$$(e^-) = \frac{\Gamma_0}{k_2[O_2]_i + k_3(h^+)} \tag{4.9}$$

$$(h^+) = \frac{\Gamma_0}{k_1 + k_3(e^-)} \tag{4.10}$$

where Γ_0 is the flux of electrons and holes created by the absorption of light by TiO_2. The fluxes of electrons and holes across the TiO_2/aqueous interface balance, so that the rate of oxygen reduction (or water oxidation), j, is given by:

$$j = \frac{k_1 k_2 [O_2]_i}{2k_3}\left[\left(1 + \frac{4\Gamma_0 k_3}{k_1 k_2 [O_2]_i}\right)^{1/2} - 1\right] \tag{4.11}$$

When $\frac{4\Gamma_0 k_3}{k_1 k_2 [O_2]_i} >> 1$, *i.e.*, when recombination is significant, equation (4.11) simplifies to:

$$j = \left(\frac{k_1 k_2 \Gamma_0 [O_2]_i}{k_3} \right)^{1/2} \tag{4.12}$$

Equation (4.12) predicts that the rate of oxygen reduction should be half-order in both the interfacial concentration of oxygen and the light flux intensity.

Several cases were considered to describe electron transfer to oxygen. Equation (4.7) represents the case where electron transfer to oxygen occurs in solution, but it is also important to consider that oxygen may adsorb at the TiO_2 surface prior to electron transfer. If adsorption is rapid (as implicitly assumed in most photomineralisation kinetic studies), the concentration of surface-bound oxygen will depend on the isotherm which describes the adsorption process, and the rate law for the reduction of oxygen becomes:

$$j = \left(\frac{k_1 k_2' \Gamma_0 \Omega}{k_3} \right)^{1/2} \tag{4.13}$$

where Ω represents the surface density of adsorbed oxygen. The rate constant for the electron transfer process is now denoted by k_2' to indicate both a change in the nature of the reaction and in the units of the rate constant.

The Langmuir isotherm is usually employed for the adsorption of oxygen in photomineralisation studies. Applying this isotherm to equation (4.13), the following expression is obtained:

$$j = \left(\frac{k_1 k_2' \Gamma_0 \Omega_{max}}{k_3} \right)^{1/2} \left(\frac{K_{O_2} [O_2]_i}{1 + K_{O_2} [O_2]_i} \right)^{1/2} \tag{4.14}$$

where Ω_{max} represents the maximum surface density of adsorbed oxygen and K_{O_2} is the equilibrium adsorption constant for oxygen. It should be noted that the adsorption process is written in terms of the concentration of oxygen at the

TiO_2/water interface, in contrast to previous treatments which consider bulk concentrations.[18,19]

The limits to equation (4.14), $K_{O_2}[O_2]_i << 1$ and $K_{O_2}[O_2]_i >> 1$, result in equations (4.15) and (4.16) respectively:

$$j = \left(\frac{k_1 k_2' \Gamma_0 \Omega_{max} K_{O_2}[O_2]_i}{k_3} \right)^{1/2} \tag{4.15}$$

$$j = \left(\frac{k_1 k_2' \Gamma_0 \Omega_{max}}{k_3} \right)^{1/2} \tag{4.16}$$

Equation (4.15) predicts the same half-order dependence on interfacial oxygen concentration as equation (4.12), while equation (4.16) suggests a zero-order dependence on $[O_2]_i$.

Another approach worth considering to describe the photoreduction of oxygen is a simple Langmuir-Hinshelwood model, since this approach has been adopted in previous photomineralisation studies.[18] In this case, the rate law has the following form:

$$j = \frac{k' K_{O_2}[O_2]_i}{1 + K_{O_2}[O_2]_i} \tag{4.17}$$

where k' is the rate constant for the heterogeneous electron transfer process.

The limits in equation (4.17) result in first- and zero-order dependences on the interfacial oxygen concentration, for $K_{O_2}[O_2]_i << 1$ and $K_{O_2}[O_2]_i >> 1$, respectively:

$$j = k' K_{O_2}[O_2]_i \tag{4.18}$$

$$j = k' \tag{4.19}$$

If the adsorption step itself were rate-limiting, then a rate law with a first-order dependence on $[O_2]_i$ might be expected of the form:

$$j = k''[O_2]_i \tag{4.20}$$

where k'' is an experimentally-observable heterogeneous rate constant.

4.3.2 Mass Transfer Model for the SECM Simulation

Formulation of the Model

A numerical model was developed to describe mass transfer in the SECM geometry, assuming simple Langmuir-Hinshelwood reaction kinetics at the TiO_2 interface, as described by equation (4.17). For the case where the oxidized form of a redox species, Ox, is electrolytically-reduced at the UME producing the reduced species, Red, the reaction at the tip is:

$$\text{Tip:} \quad \text{Ox} + ne^- \rightarrow \text{Red} \tag{4.21}$$

The time-dependent diffusion equation, appropriate to the axisymmetric cylindrical geometry of the SECM can be written for the species of interest, O_2,

$$\frac{\partial c_{Ox}}{\partial t} = D_{Ox}\left[\frac{\partial^2 c_{Ox}}{\partial r^2} + \frac{1}{r}\frac{\partial c_{Ox}}{\partial r} + \frac{\partial^2 c_{Ox}}{\partial z^2}\right] \tag{4.22}$$

where c_{Ox} and D_{Ox} are, respectively, the concentration and diffusion coefficient of the oxidised species, t is time and r and z are spatial co-ordinates in directions radial and normal to the electrode surface, respectively, measured from the centre of the electrode (see Figure 4.3).

To calculate the tip current response, the diffusion equations must be solved subject to the boundary and initial conditions of the system. Initially O_2 is present in the solution at a concentration, c_{Ox}^*. The initial condition is thus,

$$t = 0; \qquad 0 \le r \le r_g,\ 0 \le z \le d:\ c_{Ox} = c_{Ox}^* \tag{4.23}$$

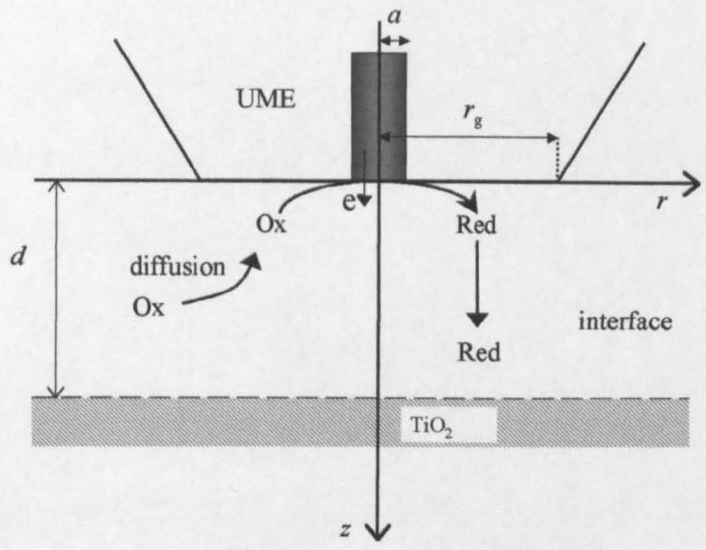

Figure 4.3 Schematic of the co-ordinate system used in the model. The co-ordinates r and z are measured from the centre of the UME in the radial and normal directions, respectively. The UME is characterised by an electrode radius a, and r_g is the distance from the centre of the electrode to the edge of the surrounding insulating glass sheath. d is the distance between the UME and the TiO_2 surface.

where d denotes the distance between the UME and the TiO_2 substrate and r_g is the location of the edge of the glass sheath surrounding the UME.

At time $t > 0$, the potential of the UME tip is stepped from a value where no electrode reaction occurs, to one sufficient to drive the reduction of Ox at a diffusion-controlled rate. Species Ox is assumed to be inert with respect to the insulating glass sheath surrounding the electrode and to remain at bulk concentration values beyond the radial edge of the tip. These boundary conditions may be summarized as follows:

$$z = 0, \qquad 0 \le r \le a \qquad : \qquad c_{Ox} = 0 \tag{4.24}$$

$$z = 0, \qquad a < r \le r_g \qquad : \qquad D_{Ox} \frac{\partial c_{Ox}}{\partial z} = 0 \tag{4.25}$$

$$r > r_g, \qquad 0 < z < d \qquad : \qquad c_{Ox} = c_{Ox}^{*} \tag{4.26}$$

Equation (4.26) is a reasonable assumption provided that $RG = r_g / a \geq 10$,[20] where a is the radius of the electrode.

The axisymmetric geometry of the SECM implies that there is no radial flux of the species at the cylindrical axis of symmetry:

$$r = 0, \qquad 0 < z < d \qquad : \qquad D_{Ox} \frac{\partial c_{Ox}}{\partial r} = 0 \tag{4.27}$$

The final boundary condition applies to the surface of the TiO_2 substrate. During the first part of the simulation, *i.e.*, prior to turning on the UV illumination, there is no reaction of O_2 at the TiO_2 substrate, hence,

$$z = d, \qquad 0 < z < d \qquad : \qquad D_{Ox} \frac{\partial c_{Ox}}{\partial z} = 0 \tag{4.28}$$

The simulation calculates the current-time response of the UME and is run until the current reaches steady state, *ca.* 10 s. At this time, t_{switch}, the UV illumination is switched on and the boundary condition at the interface is changed to follow Langmuir-Hinshelwood kinetics:

$$t > t_{switch} \qquad j_z = -D_{Ox} \frac{\partial c_{Ox,int}}{\partial z} = \frac{k' K_{Ox} c_{Ox,int}}{1 + K_{Ox} c_{Ox,int}} \tag{4.29}$$

To formulate a general solution, the problem was cast into dimensionless form through the introduction of the following terms

$$\tau = \frac{t D_{Ox}}{a^2} \tag{4.30}$$

$$R = \frac{r}{a} \tag{4.31}$$

$$Z = \frac{z}{a} \tag{4.32}$$

$$C = \frac{c_{Ox}}{c_{Ox}^*} \tag{4.33}$$

$$k_n' = \frac{k' a}{D_{Ox} c_{Ox}^*} \tag{4.34}$$

$$K_{Ox}^n = c_{Ox}^* K_{Ox} \tag{4.35}$$

It should be clear how these terms affect the diffusion equation (equation 4.22) and associated boundary and initial conditions.

The tip current response is calculated as a function of time and tip/interface separation. The UME current is related to the flux of Ox at the electrode surface and hence the dimensionless current ratio is given by:[21]

$$\frac{i}{i(\infty)} = \frac{\pi}{2} \int_0^1 \left(\frac{\partial C_{Ox}}{\partial Z} \right)_{Z=0} R dR \tag{4.36}$$

where $i(\infty)$ is the steady-state diffusion-limited current at an inlaid disc electrode positioned at an effectively infinite distance from the interface.[22]

$$i(\infty) = 4nFaD_{Ox} c_{Ox}^* \tag{4.37}$$

Method of Solution

Numerical solutions were achieved using a FORTRAN program based on the alternating direction implicit finite-difference method (ADIFDM) algorithm.[23] Simulations were run on the University of Warwick central unix system. The application of ADIFDM to a diversity of SECM problems has been described elsewhere.[21,24,25,26,27,28] This section briefly highlights the main modifications required to treat the boundary condition at TiO_2 surface. Further details on the treatment of the remaining boundary conditions and implementation of the numerical solution can be found in more in depth accounts of ADIFDM as applied to SECM.[21,24,25]

The ADIFDM involves the construction of implicit finite difference equations at successive half-time intervals for the R and Z directions. The finite-difference grid employed was as used previously.[24(a)] For the first half-time step, in which concentrations were calculated in the R direction from known values deduced in the Z direction in the previous half-time step, the calculation proceeded from the points $j = 1$ to $j = NE+NG-1$, where j denotes the grid points in the radial direction running from $j = 0$ at $R = 0$ to $j = NE$ at $R = 1$ (over the tip electrode) and $j = NE+1$ to $j = NE+NG$ over the insulating glass sheath. This results in $NE+NG-1$ simultaneous equations in $NE+NG-1$ unknowns for each grid point, k, in the Z direction where k runs from $k = 0$ at the UME surface to $k = NZ$ at the substrate. After application of the boundary conditions above, these equations may be expressed as a tridiagonal matrix, the solution of which is found using the Thomas algorithm.[29]

At the end of the first half-time step the boundary condition, equation (4.29), in finite-difference form is employed to update the concentration of Ox at the substrate for each node on the FD grid in the R direction.

$$K_{Ox}^{n}\left(C_{j,NZ}^{*}\right)^{2}+\left[1-K_{Ox}^{n}C_{j,NZ-1}^{*}+\Delta Zk_{n}^{'}K_{Ox}^{n}\right]C_{j,NZ}^{*}-C_{j,NZ-1}^{*}=0 \qquad (4.38)$$

In equation (4.38) $C_{j,k}^{*}$ denotes the new concentration of Ox calculated in first half-time step at the grid point with co-ordinates (j,k).

For the second half time step the boundary condition, equation (4.29), in finite-difference form is

$$C_{j,NZ}^{**}=C_{j,NZ-1}^{**}-\frac{k_{n}^{'}K_{Ox}^{n}\Delta ZC_{j,NZ}^{**}}{1+K_{Ox}^{n}C_{j,NZ}^{**}} \qquad (4.39)$$

where the double * denotes the new concentration of Ox calculated in the R direction in the second half-time step. It is apparent from equation (4.39) that

calculation of the new R concentrations requires a prior knowledge of the new concentration, $C^{**}_{j,NZ}$ for each j value, which have yet to be calculated, for the matrix equations to reduce to tridiagonal form. An iterative procedure was adopted in which for a particular value of j, $C^{**}_{j,NZ}$ on the right hand side of equation (4.39) was initially approximated by $C^{*}_{j,NZ}$ (calculated in the first-half time step). Following the calculation of all the radial concentrations, $C^{**}_{j,k}$, $C^{**}_{j,NZ}$ was updated.

$$K^{n}_{Ox}\left(C^{**}_{j,NZ}\right)^{2} + \left[1 - K^{n}_{Ox}C^{**}_{j,NZ-1} + \Delta Z k'_{n} K^{n}_{Ox}\right]C^{**}_{j,NZ} - C^{**}_{j,NZ-1} = 0 \qquad (4.40)$$

The procedure was repeated using the newly determined value for $C^{**}_{j,NZ}$ until changes in $C^{**}_{j,NZ}$ were less than 10^{-4} % upon further iteration.

4.4 Experimental Results and Discussion

4.4.1 Preliminary Studies: Testing the Effect of UV Illumination

Firstly, the SECM control measurements of the extent of oxygen depletion at the illuminated fibre surface in the absence of TiO_2 were demonstrated in a 0.1 M $NaClO_4$ solution. A 25 μm diameter Ag UME was positioned at a precise distance above the fibre surface and the potential was held at –1.0 V to effect the diffusion-limited reduction of oxygen. The steady-state current for the hindered diffusion of oxygen to the UME provided information of the tip-substrate separation *via* theory of the type from Kwak and Bard.[20] Transients were then recorded at the tip UME after stepping the UV illumination on and off. A typical transient is shown in Figure 4.4. The reduction current experienced at the UME shows a fairly constant value, indicating that when there is no TiO_2, the associated photoresponse of the UME is negligible. This indicates that a sensitive means of

investigating the photoelectrochemical reduction of oxygen at the TiO_2 substrate could be made by illuminating a TiO_2 film and detecting the depletion *via* the reduction of oxygen at the tip.

The next step was to assess the reduction of oxygen catalysed by TiO_2. Transients for oxygen reduction at the tip UME were recorded in 0.1 M $NaClO_4$ solution and a typical response is shown in Figure 4.5. When the TiO_2 surface was illuminated, the tip current significantly decreased, meaning that less oxygen is detected by the probe. This is due to the consumption of oxygen in the photoprocess at the TiO_2 surface. Illumination causes the photogenerated electrons to be captured by O_2 to produce $O_2^{\bullet-}$, thus causing a depletion of oxygen concentration at, and near, the catalyst surface. In contrast, when the illumination was suddenly stopped, the transient response tended to level off towards the dark value, consistent with no ongoing photocatalytic reaction, and oxygen reaching the probe by hindered diffusion. This result demonstrates that molecular oxygen participates significantly in the photocatalytic process. A schematic representation of the reduction of oxygen at the UME probe, with and without illumination, is shown in Figure 4.6.

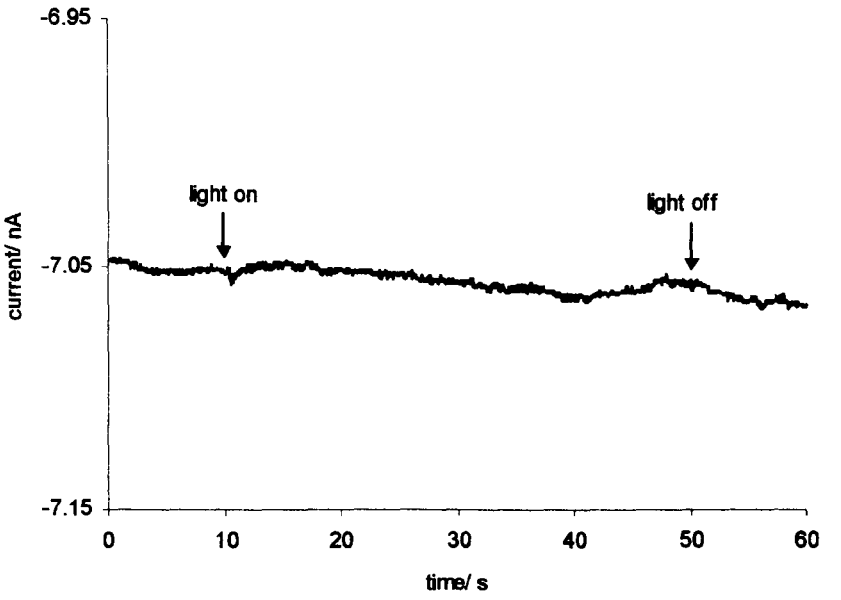

Figure 4.4 Phototransient response at an Ag UME, held at –1.0 V, for the reduction of oxygen in a 0.1 M $NaClO_4$ solution in the absence of a TiO_2 film. The UME was positioned 20 μm away from the fibre surface and the illumination was switched on at 10 s and switched off at 50 s.

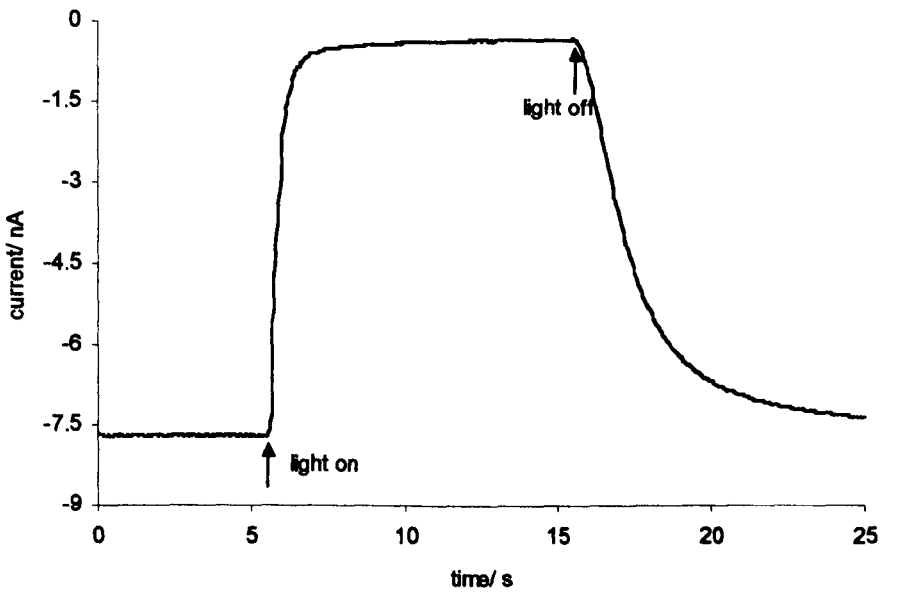

Figure 4.5 Phototransient response at an Ag UME, held at –1.0 V, for the reduction of oxygen in a 0.1 M $NaClO_4$ solution in the presence of a TiO_2 film. The tip-substrate distance was 22.8 μm.

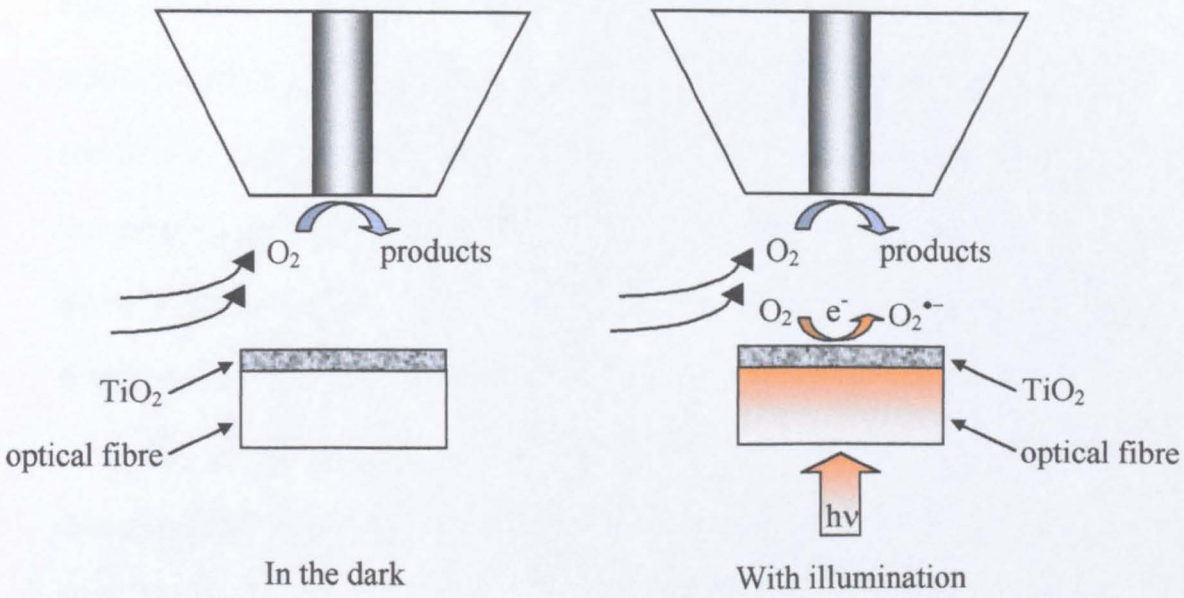

Figure 4.6 Schematic representation of the photoelectrochemical reduction of oxygen.

4.4.2 Mechanistic Study of the Photoelectrochemical Reduction of Oxygen at TiO_2 Films

4.4.2.1 In the Presence of an Aqueous Electrolyte Solution

Transients for oxygen reduction at an Ag UME were recorded in an aqueous aerated 0.1 M $NaClO_4$ solution. The UME was positioned at a known distance, *d*, from the TiO_2 film based on the negative feedback response for oxygen reduction in the dark, as discussed above. A set of typical transient responses are shown in Figure 4.7 for $d = 19.1$ μm. The diminution in the oxygen reduction current becomes smaller as the transients are performed consecutively and from the 3rd transient onwards a spike in the cathodic direction is observed immediately after switching on the light. The current corresponding to the spike was higher than the dark oxygen reduction current and became larger as further transient measurements were made. To assess if this behaviour could be due to the electrode response, the UME was taken out, polished with alumina and put back

again at the same distance. The transient recorded afterwards also showed a spike, which means that this behaviour was not due a degradation of the electrode surface with time. The experiment was also performed in a phosphate buffer, but the transients recorded showed the same trends as the ones in Figure 4.7, *i.e.*, a decrease in the diminution of the oxygen reduction current, accompanied by the formation of a spike after switching the light on.

To investigate this effect further, transients were run in an aqueous deoxygenated solution of supporting electrolyte (0.1 M $NaClO_4$) with the Ag UME held at a potential to detect the reduction of oxygen (-1.0 V). The transients obtained are shown in Figure 4.8. The first transient shows a large cathodic current spike, which occurs very quickly after switching on the light, but the spike becomes smaller as further transient measurements are performed. The spike is probably due to desorption of oxygen that was adsorbed at the TiO_2 surface. A possible evidence for this is that when the potential at the UME is held at –0.1 V, where the reduction of oxygen at the tip cannot occur, a spike was not observed (Figure 4.9). There is also evidence in the literature that when a rutile TiO_2 (110) surface is illuminated with UV light oxygen photodesorbs from the surface.[30] This, however, does not explain the formation of the spikes in Figure 4.7.

When the experiment was performed in the same aerated aqueous electrolyte solution, but at a smaller tip-substrate distance (9.6 μm), a spike was observed straight away in the first transient (Figure 4.10). Also, when the solution was oxygenated and the transient run at a tip-substrate distance of 18.9 μm, a spike was obtained in the first transient recorded (Figure 4.11). For each of these experiments a fresh TiO_2 film was used and so film history cannot explain the observed effects. The spikes are probably due to the build up of intermediates

($O_2^{\bullet-}$, $HO_2^{\bullet}$, HO_2^-, H_2O_2, $^{\bullet}OH$) formed in the photochemical process. A possible indication for this is that when the transient measurements were made in the presence of 4-chlorophenol (4-CP), which will be photomineralised as discussed later, the spikes were no longer observed (Figure 4.12). The primary products of the photomineralisation process are radicals, which will undergo secondary reactions to form more stable molecules. Molecular oxygen and activated oxygen species ($O_2^{\bullet-}$, $HO_2^{\bullet}$, HO_2^-, H_2O_2) play an essential role in these processes.[5,6,7,8]

As the transients were measured consecutively, a decrease in the overall diminution of the oxygen reduction current is observed. A possible explanation for this effect is that reactions between the intermediate species can generate oxygen, which will be detected at the UME, thus increasing the observed current for oxygen reduction. Some of the possible reactions between the intermediates that could generate oxygen are shown below (equations 4.41-4.44)[31,32] along side the hydrogen peroxide disproportionation reaction (equation 4.45).

$$HO_2^{\bullet} + HO_2^{\bullet} \rightarrow H_2O_2 + O_2 \qquad (4.41)$$

$$HO_2^{\bullet} + O_2^{\bullet-} \rightarrow HO_2^- + O_2 \qquad (4.42)$$

$$H_2O_2 + O_2^{\bullet-} \rightarrow {}^{\bullet}OH + OH^- + O_2 \qquad (4.43)$$

$$H_2O_2 + 2\,{}^{\bullet}OH \rightarrow 2H_2O + O_2 \qquad (4.44)$$

$$2H_2O_2 \rightarrow 2H_2O + O_2 \qquad (4.45)$$

In the presence of 4-chlorophenol, the systematic deterioration of the oxygen reduction current transients is less significant because the activated oxygen species will be able to react with the organic radicals formed when 4-CP is photomineralised.

When transient measurements were made in an aerated electrolyte solution employing a Pt UME instead of Ag, a deterioration in the current transients run

consecutively was again seen, but the initial spikes observed with Ag were no longer observed (Figure 4.13). This difference in the transient response could be due to the influence of the detector electrode material and the state of oxidation/reduction of its surface. While oxygen reduction at an Ag UME is a $4e^-$ process, at Pt it occurs in $2 \times 2e^-$ steps in which H_2O_2 is the $2e^-$ product in acidic solutions.[17] It has been shown that H_2O_2 is the major product from oxygen reduction in conditions leading to a high mass-transfer coefficient, *i.e.*, at Pt microelectrodes.[16]

The experiments in this section prove the general concept of the proposed technique. However, to prevent the interference from the radical intermediates on the determination of the oxygen reduction kinetics, the experiments described in the next section were performed in the presence of a hole scavenger (triethanolamine).

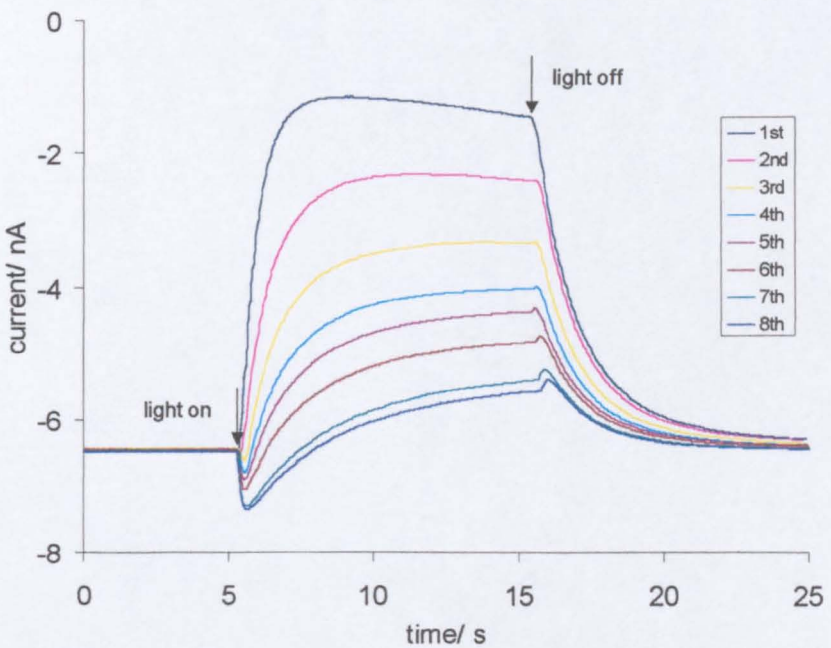

Figure 4.7 Phototransient responses at the Ag UME, held at –1.0 V, for the reduction of oxygen in an aqueous aerated 0.1 M $NaClO_4$ solution. The tip-substrate distance was 19.1 μm.

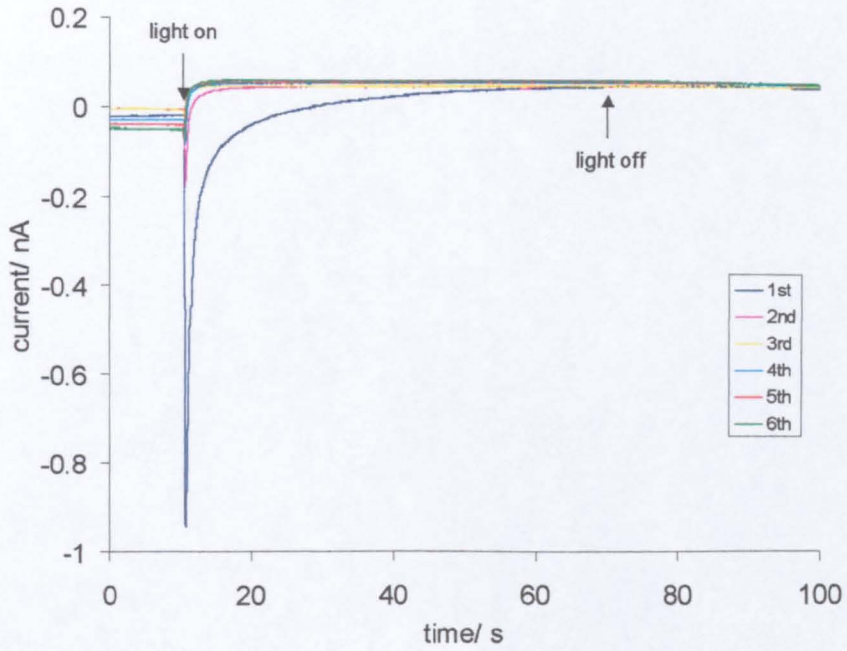

Figure 4.8 Phototransient responses at the Ag UME, which was held at a potential to detect the reduction of oxygen (-1.0 V), in an aqueous deoxygenated 0.1 M $NaClO_4$ solution. The tip-substrate distance was 19.0 μm.

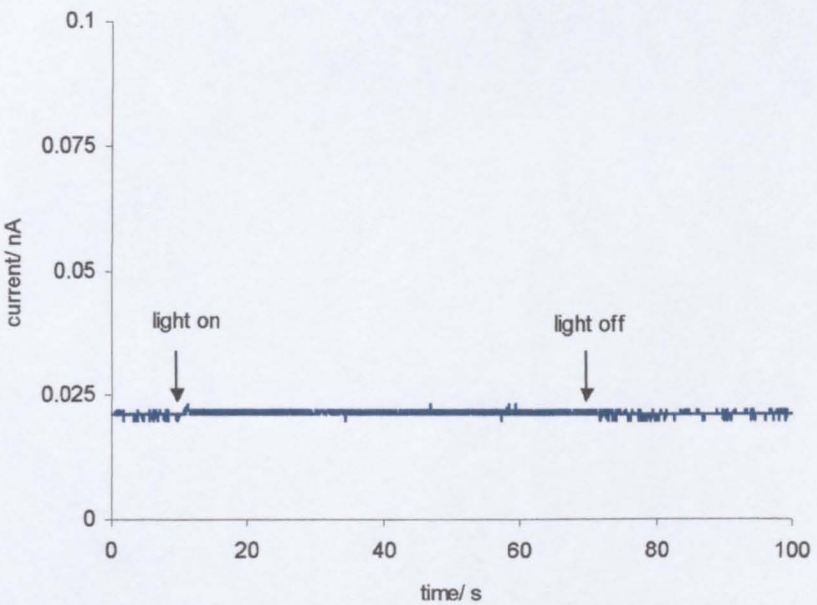

Figure 4.9 Phototransient response at the Ag UME, which was held at a potential (-0.1 V) where the reduction of oxygen could not occur, in an aqueous deoxygenated 0.1 M $NaClO_4$ solution. The tip-substrate distance was 18.4 μm.

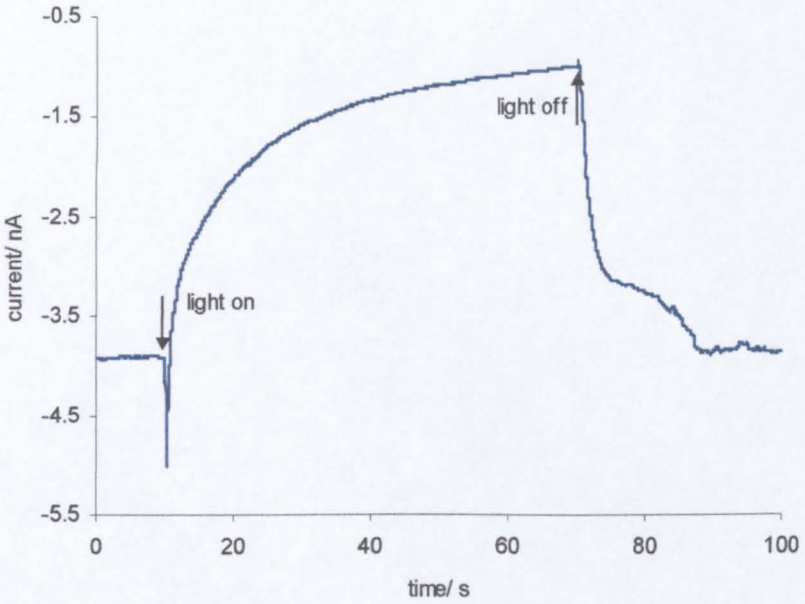

Figure 4.10 Phototransient response at the Ag UME, held at –1.0 V, for the reduction of oxygen in an aqueous aerated 0.1 M $NaClO_4$ solution. The tip-substrate distance was 9.6 μm.

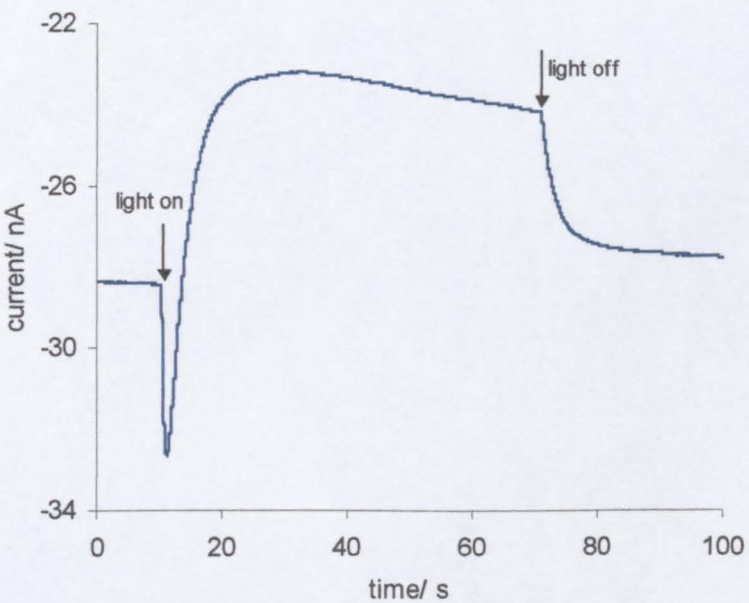

Figure 4.11 Phototransient response at the Ag UME, held at –1.0 V, for the reduction of oxygen in an aqueous oxygenated 0.1 M $NaClO_4$ solution. The tip-substrate distance was 18.9 μm.

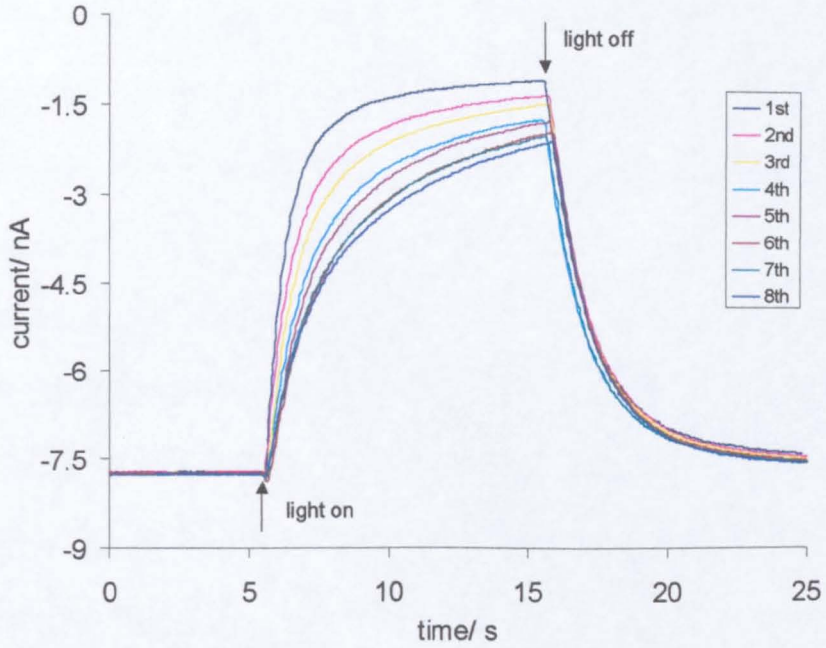

Figure 4.12 Phototransient responses at the Ag UME, held at –1.0 V, for the reduction of oxygen in an aqueous aerated 1.0×10^{-3} mol dm^{-3} 4-CP solution in the presence of 0.1 M $NaClO_4$ as supporting electrolyte. The tip-substrate distance was 19.4 μm.

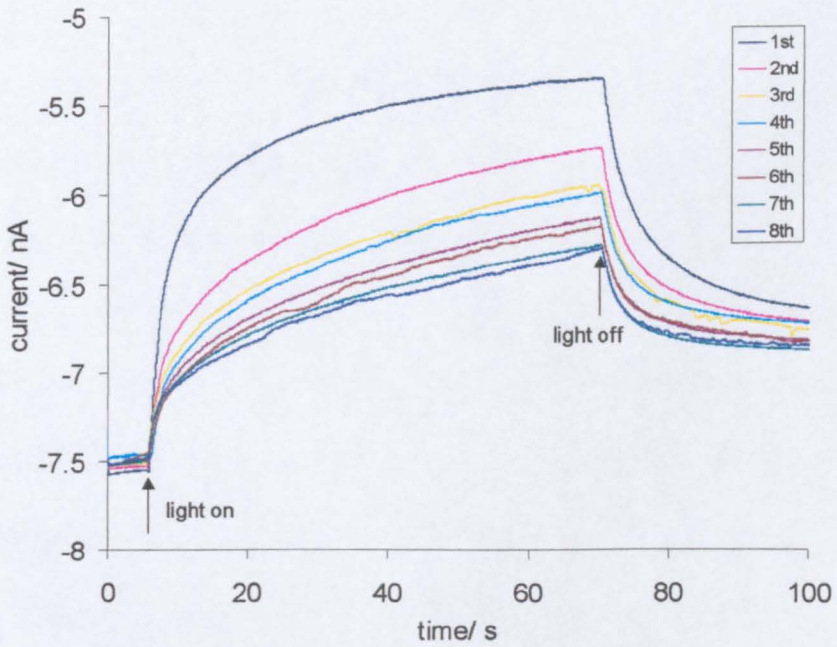

Figure 4.13 Phototransient responses at the Pt UME, held at –1.0 V, for the reduction of oxygen in an aqueous aerated 0.1 M $NaClO_4$ solution. The tip-substrate distance was 19.2 μm.

4.4.2.2 In the Presence of a Hole Scavenger

Transients for oxygen reduction at a Pt UME were recorded in an aqueous 5.0×10^{-2} mol dm^{-3} triethanolamine solution in the presence of 0.1 M $NaClO_4$ as supporting electrolyte. Triethanolamine acts as a hole scavenger and the problems encountered in the last section, *i.e.*, a decrease in the depletion of the oxygen reduction current as transients were recorded consecutively, and in the case of the Ag UME accompanied by the formation of spikes, were no longer observed. As shown in Figure 4.14, systematic deterioration of the oxygen reduction current transient was negligible, which allowed kinetic and mechanistic investigation of light intensity and oxygen concentration effects.

The light flux intensity was varied by using neutral density filters which only transmitted 50%, 25% and 12.5% of the incident light intensity. The oxygen levels present in an aerated solution (~ 20%) were increased to 50% and saturation by purging the solution with a 50% O_2/ N_2 mixture and pure oxygen, respectively. The transients for oxygen reduction at four different light intensities and for aerated, 50% O_2 and oxygenated conditions are shown in Figure 4.15(a), (b) and (c), respectively. As the light intensity decreases the transients become less sharp and there is a smaller depletion in the oxygen reduction current.

The results were analysed using the theoretical models described in sections 4.3.1 and 4.3.2. As an example, the data obtained at the maximum light intensity ($I_0 = 2.13 \times 10^{16}$ q cm^{-2} s^{-1}) for the three different oxygen concentrations are analysed in terms of the zero- and half-order models in Figures 4.16, 4.17 and 4.18. Figure 4.16 shows the best simulated behaviour for the zero-order model ($k_{zero} = 3.19 \times 10^{-10}$ mol cm^{-2} s^{-1}) and the half-order model ($k_{half} = 1.50 \times 10^{-6}$ $mol^{1/2}$ $cm^{-1/2}$ s^{-1}) for aerated conditions. In Figures 4.17 and 4.18 are given the best

fits for the zero-order (k_{zero} = 7.98 × 10^{-10} and 1.14 × 10^{-9} mol cm^{-2} s^{-1}) and the half-order (k_{half} = 2.30 × 10^{-6} and 1.63 × 10^{-6} $mol^{1/2}$ $cm^{-1/2}$ s^{-1}) models for 50% O_2 and oxygenated conditions, respectively. It can be seen that these models only fit the experimental data when the steady-state has been reached and that they do not provide a good description of the initial few seconds after the light has been switched on.

To see if a better agreement between the experimental data and the model simulations could be obtained, the transients were also analysed using a Langmuir-Hinshelwood model. This model requires an equilibrium adsorption constant for oxygen and the literature values of K_{O_2} = 9.63 × 10^6 mol^{-1} cm^3 [33] and 4.89 × 10^5 mol^{-1} cm^3 [19] were used for the present numerical simulations. Figures 4.19, 4.20 and 4.21 show the best fits for the four different light intensities and for aerated, 50% O_2 and oxygenated conditions, respectively. It can be seen that the model provides a reasonably good agreement with the experimental data over the entire transient for aerated conditions and the two higher light intensities, however for the lower light intensities the model only fits to the steady-state. When the light is stepped on, the oxygen molecules adsorbed at the TiO_2 surface will react with the photogenerated electrons, and other oxygen molecules will adsorb at the surface causing a depletion of the oxygen concentration in the vicinity of the electrode. When the light intensity is lower, the reaction will proceed slower and the depletion in the oxygen reduction current detected at the electrode will also occur more slowly. This could be a possible explanation for the deviation observed between the experimental data and the model simulation before reaching steady-state. This deviation is also observed for the higher oxygen concentrations, even at the higher light intensities. If the oxygen concentration is higher there will

be more oxygen molecules adsorbed at the TiO_2 surface, which must react before the next ones can adsorb, thus causing the depletion in the oxygen reduction current to occur more slowly. Table 4.1 provides a summary of the rate constants obtained from the analysis of the data in Figures 4.19-4.21. It can be seen that at all light intensities, $K_{O2} = 9.63\times10^{6}$ mol^{-1} cm^{3} provides the most consistent rate constants as the oxygen concentration is changed by a factor of five (aerated to oxygenated conditions).

For comparative purposes it was useful to investigate the photoelectrochemical reduction kinetics of oxygen in an aqueous solution of a model organic substrate. Thus, the experiments described in the next section were performed in the presence of 4-chlorophenol.

Table 4.1 Values of the rate constants (mol cm^{-2} s^{-1}), estimated using a Lagmuir-Hinshelwood model, for the reduction of oxygen in a 5.0×10^{-2} mol dm^{-3} triethanolamine solution in the presence of 0.1 M $NaClO_4$ as supporting electrolyte under aerated, 50% O_2 and oxygenated conditions.

	aerated condition		50% O_2		oxygenated condition	
I_0 q cm^{-2} s^{-1}	k_{lh} K_{O2}=9.63×10^{6} mol^{-1} cm^{3}	k_{lh} K_{O2}=4.89×10^{5} mol^{-1} cm^{3}	k_{lh} K_{O2}=9.63×10^{6} mol^{-1} cm^{3}	k_{lh} K_{O2}=4.89×10^{5} mol^{-1} cm^{3}	k_{lh} K_{O2}=9.63×10^{6} mol^{-1} cm^{3}	k_{lh} K_{O2}=4.89×10^{5} mol^{-1} cm^{3}
2.13×10^{16}	1.1×10^{-9}	1.5×10^{-8}	1.5×10^{-9}	1.4×10^{-8}	1.4×10^{-9}	6.2×10^{-9}
1.07×10^{16}	8.5×10^{-10}	1.1×10^{-8}	1.0×10^{-9}	7.3×10^{-9}	9.5×10^{-10}	3.5×10^{-9}
5.33×10^{15}	6.6×10^{-10}	7.8×10^{-9}	5.5×10^{-10}	3.2×10^{-9}	5.4×10^{-10}	1.8×10^{-9}
2.66×10^{15}	3.5×10^{-10}	3.4×10^{-9}	3.0×10^{-10}	1.5×10^{-9}	3.2×10^{-10}	1.0×10^{-9}

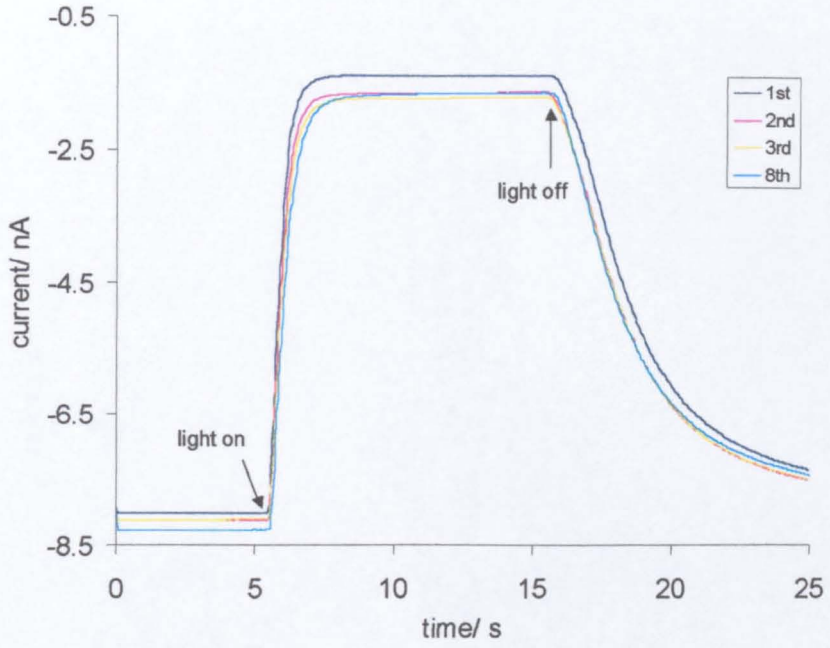

Figure 4.14 Phototransient responses at the Pt UME for the reduction of oxygen in an aqueous aerated 5.0×10^{-2} mol dm^{-3} triethanolamine solution in the presence of 0.1 M $NaClO_4$ as supporting electrolyte. The tip-substrate distance was 23.8 μm.

(a)

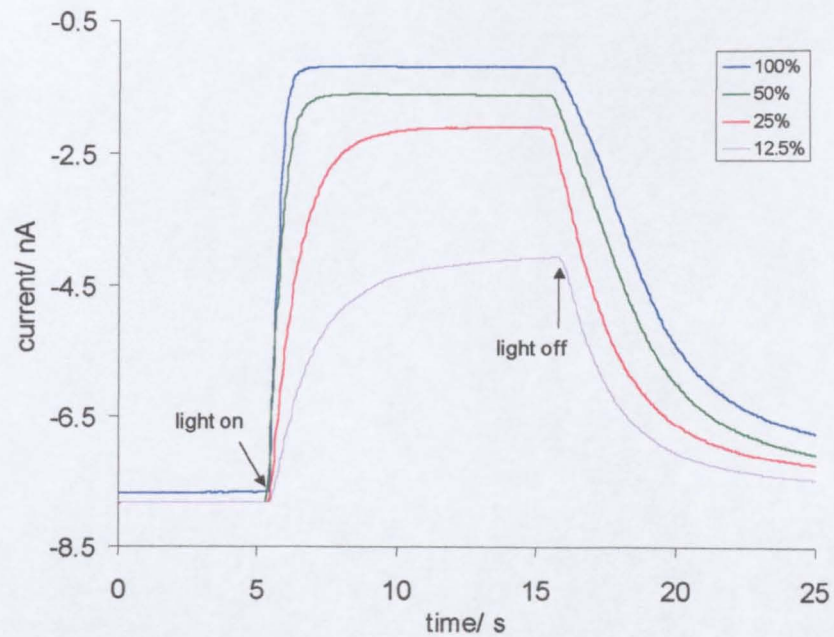

(b)

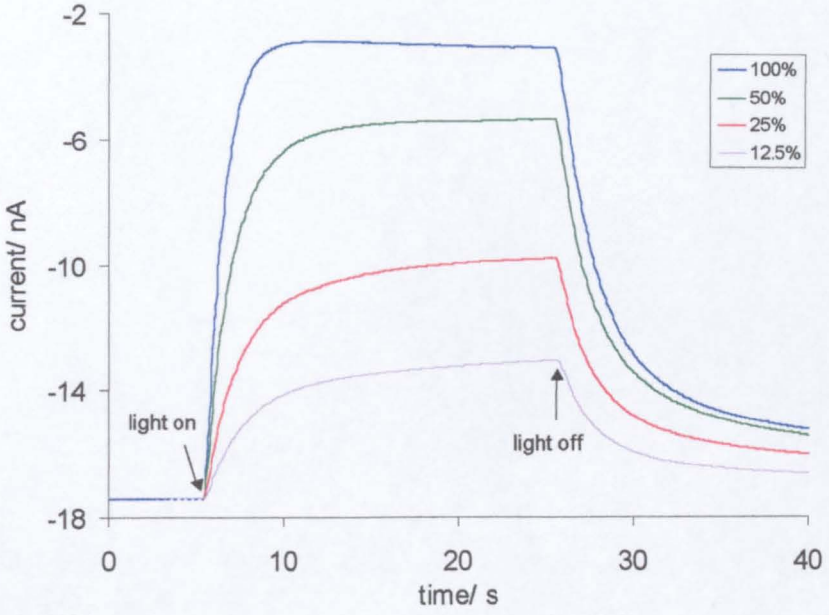

(c)

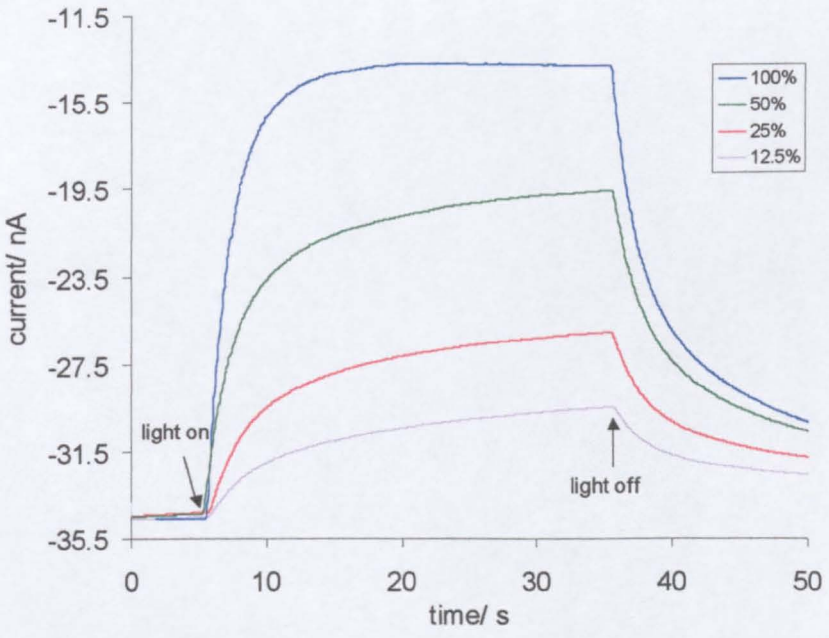

Figure 4.15 Phototransient responses at the Pt UME for the reduction of oxygen in an aqueous (a) aerated, (b) 50% O_2 and (c) oxygenated 5.0×10^{-2} mol dm^{-3} triethanolamine solution in the presence of 0.1 M $NaClO_4$ as supporting electrolyte. The tip-substrate distance was 23.4 μm.

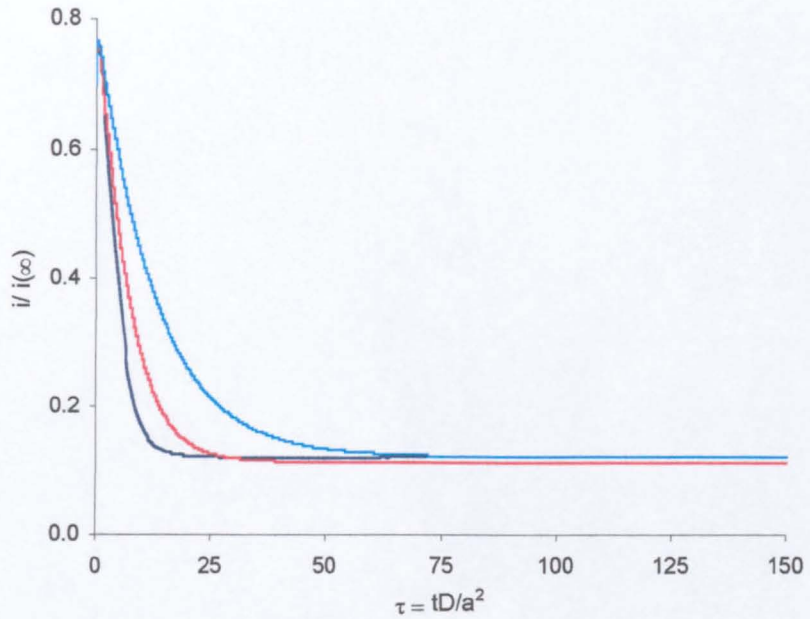

Figure 4.16 Normalised experimental data (—), after stepping the light on, for oxygen reduction in aerated conditions compared with the best fit theoretical simulations for the (—) zero-order model ($k_{zero} = 3.19 \times 10^{-10}$ mol cm^{-2} s^{-1}) and the (—) half-order model ($k_{half} = 1.50 \times 10^{-6}$ mol$^{1/2}$ cm$^{-1/2}$ s^{-1}). $I_0 = 2.13 \times 10^{16}$ q cm^{-2} s^{-1}.

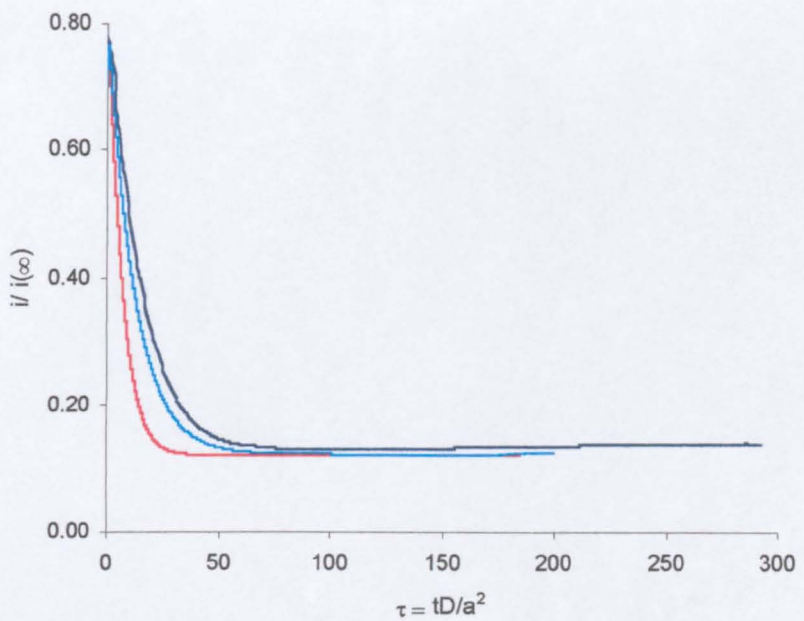

Figure 4.17 Normalised experimental data (—), after stepping the light on, for oxygen reduction in 50% O_2 conditions compared with the best fit theoretical simulations for the (—) zero-order model ($k_{zero} = 7.98 \times 10^{-10}$ mol cm^{-2} s^{-1}) and the (—) half-order model ($k_{half} = 2.30 \times 10^{-6}$ mol$^{1/2}$ cm$^{-1/2}$ s^{-1}). $I_0 = 2.13 \times 10^{16}$ q cm^{-2} s^{-1}.

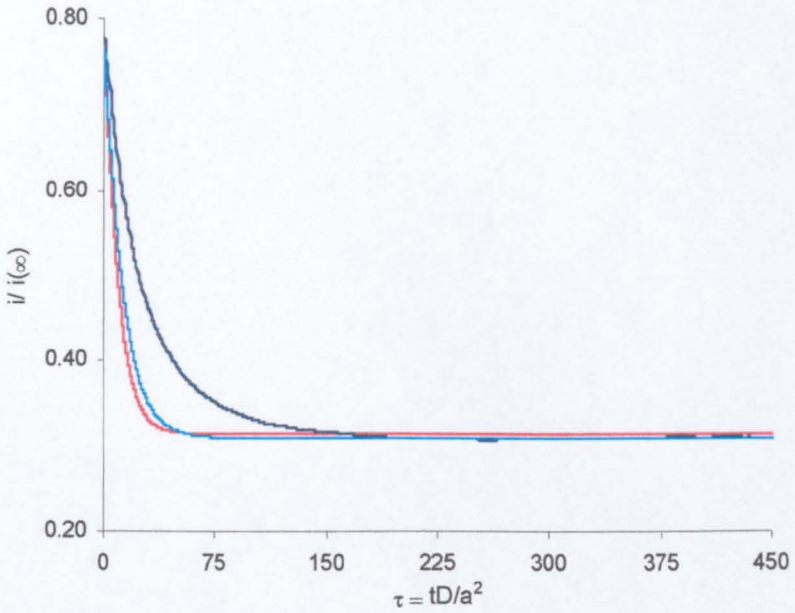

Figure 4.18 Normalised experimental data (—), after stepping the light on, for oxygen reduction in oxygenated conditions compared with the best fit theoretical simulations for the (—) zero-order model ($k_{zero} = 1.14 \times 10^{-9}$ mol cm^{-2} s^{-1}) and the (—) half-order model ($k_{half} = 1.63 \times 10^{-6}$ mol$^{1/2}$ cm$^{-1/2}$ s^{-1}). $I_0 = 2.13 \times 10^{16}$ q cm^{-2} s^{-1}.

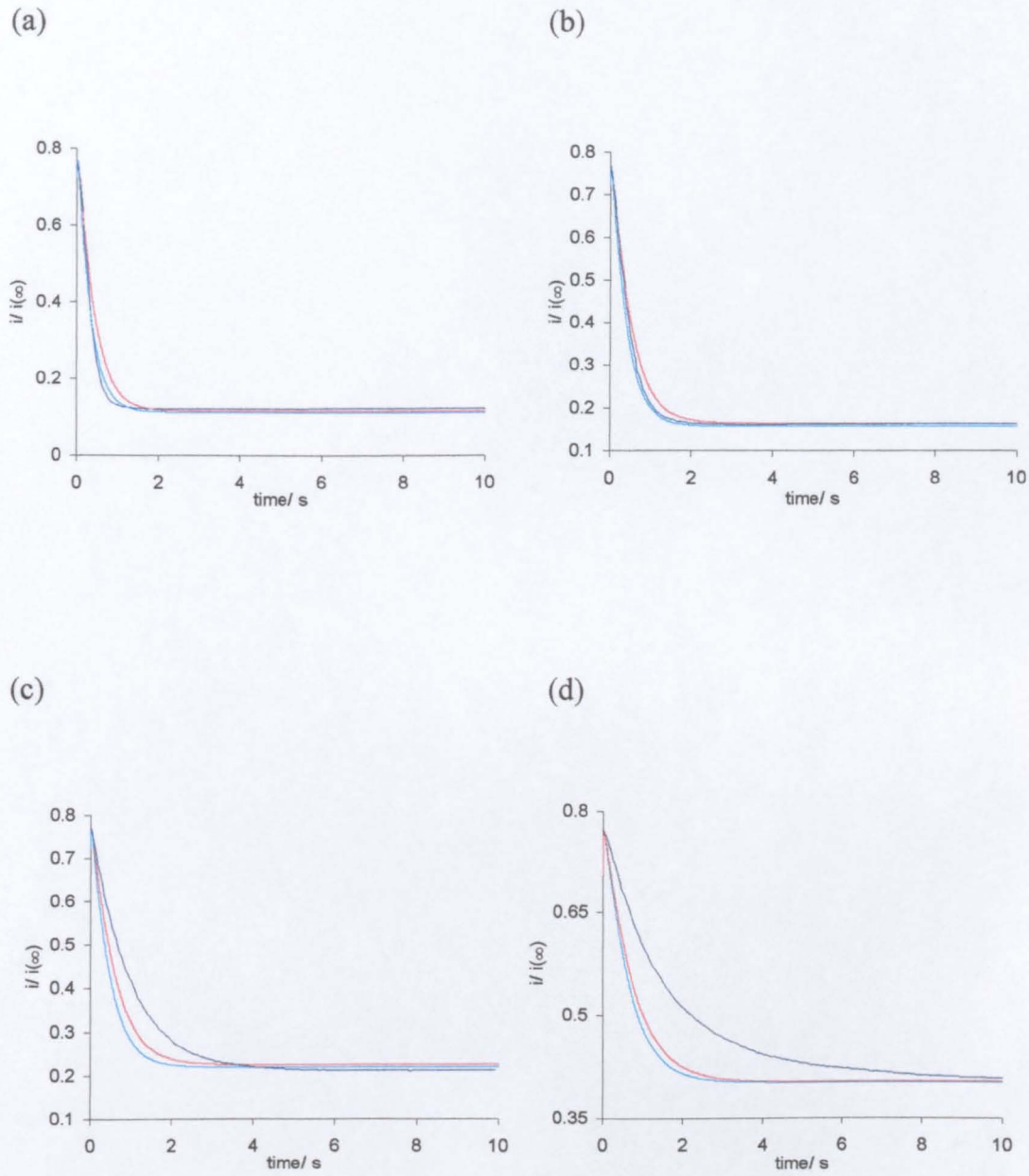

Figure 4.19 Experimental data (—) for oxygen reduction in aerated conditions compared with the best fit theoretical simulations for the Langmuir-Hinshelwood model for (—) $K_{O2} = 9.63 \times 10^{6}$ mol^{-1} cm^{3} and (—) $K_{O2} = 4.89 \times 10^{5}$ mol^{-1} cm^{3}, at (a) $I_0 = 2.13 \times 10^{16}$ q cm^{-2} s^{-1}, (b) $I_0 = 1.07 \times 10^{16}$ q cm^{-2} s^{-1}, (c) $I_0 = 5.33 \times 10^{15}$ q cm^{-2} s^{-1} and (d) $I_0 = 2.66 \times 10^{15}$ q cm^{-2} s^{-1}.

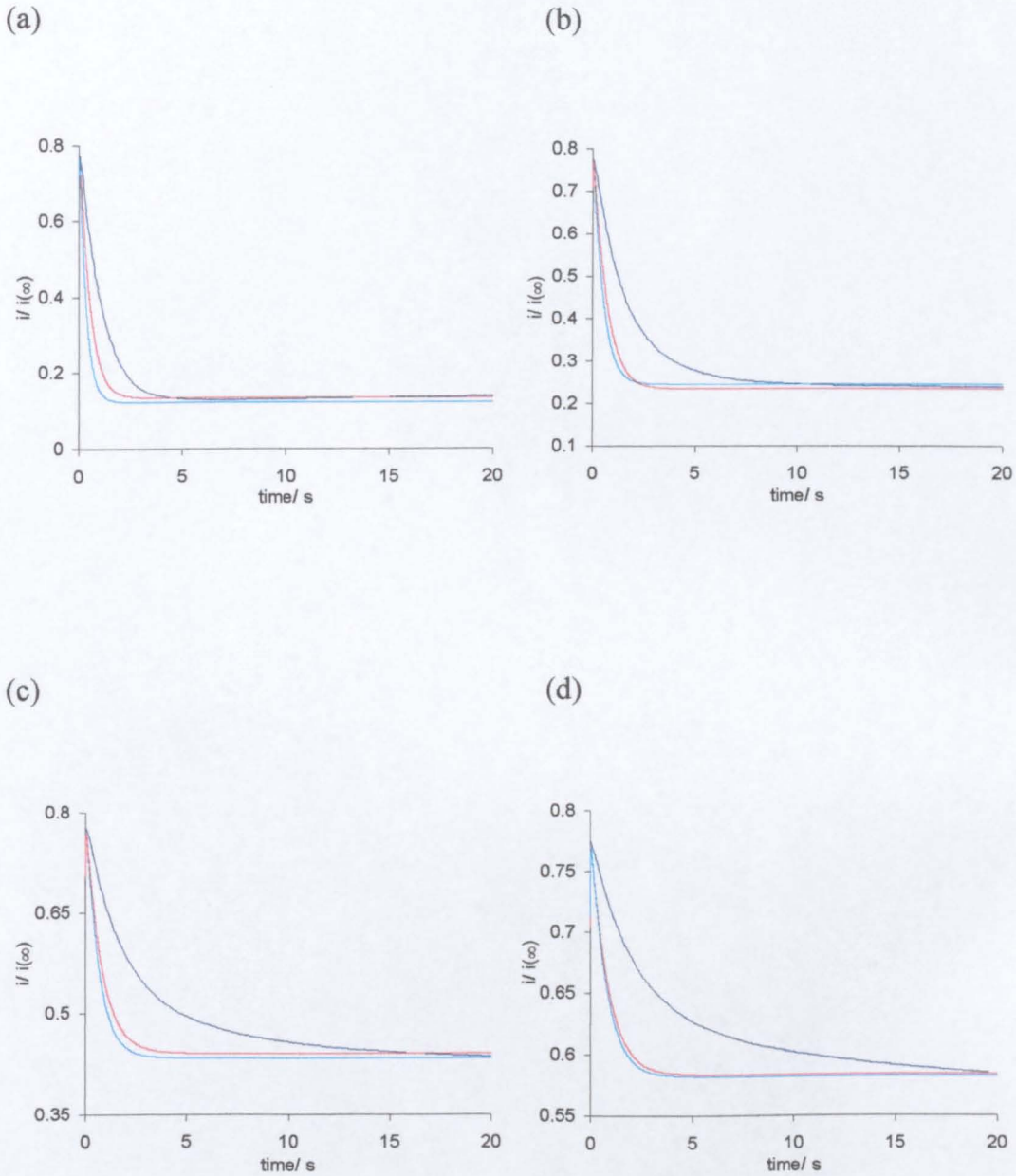

Figure 4.20 Experimental data (—) for oxygen reduction in 50% O_2 conditions compared with the best fit theoretical simulations for the Langmuir-Hinshelwood model for (—) $K_{O2} = 9.63 \times 10^6$ mol^{-1} cm^3 and (—) $K_{O2} = 4.89 \times 10^5$ mol^{-1} cm^3, at (a) $I_0 = 2.13 \times 10^{16}$ q cm^{-2} s^{-1}, (b) $I_0 = 1.07 \times 10^{16}$ q cm^{-2} s^{-1}, (c) $I_0 = 5.33 \times 10^{15}$ q cm^{-2} s^{-1} and (d) $I_0 = 2.66 \times 10^{15}$ q cm^{-2} s^{-1}.

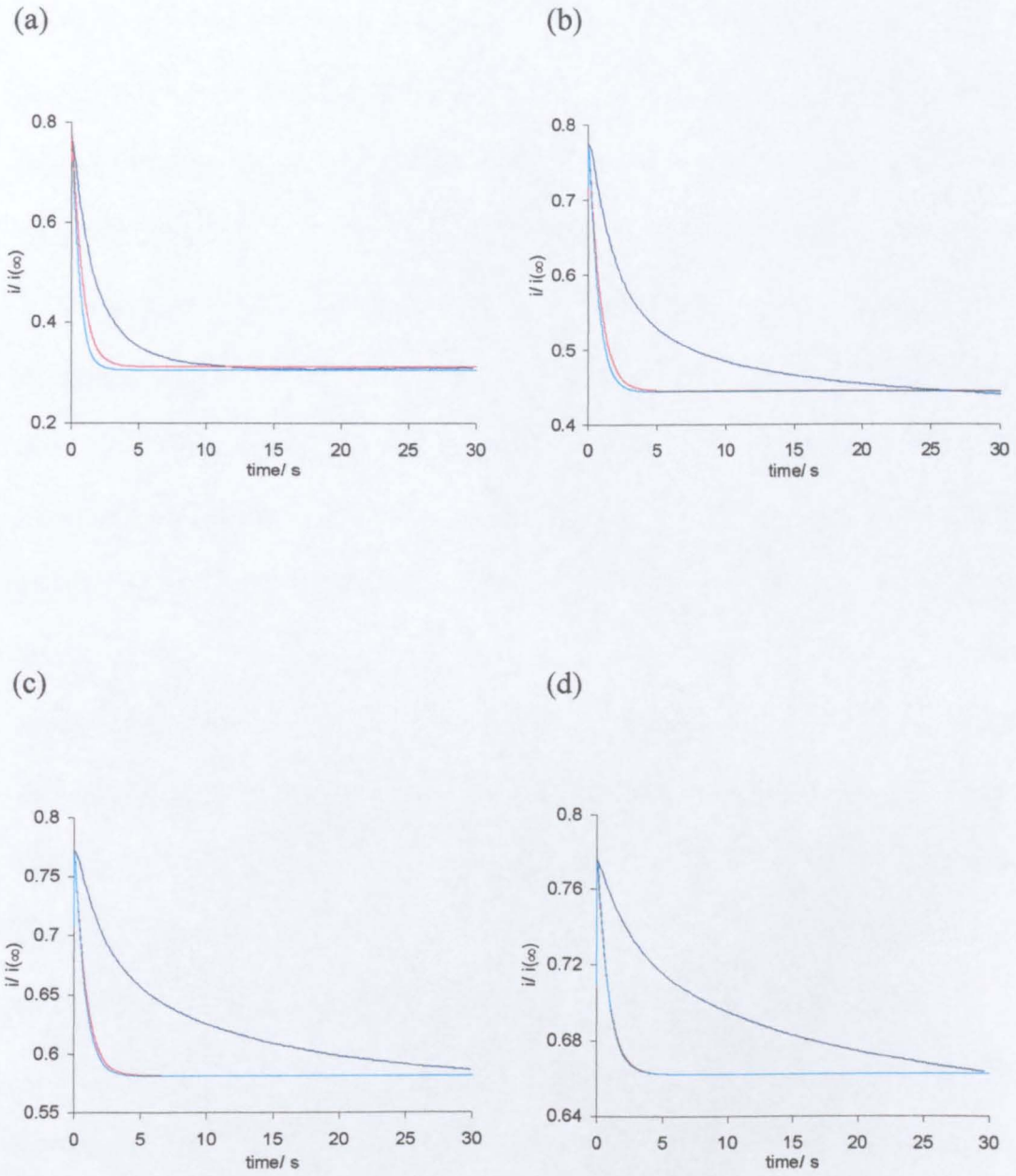

Figure 4.21 Experimental data (—) for oxygen reduction in oxygenated conditions compared with the best fit theoretical simulations for the Langmuir-Hinshelwood model for (—) $K_{O2} = 9.63 \times 10^6$ mol^{-1} cm^3 and (—) $K_{O2} = 4.89 \times 10^5$ mol^{-1} cm^3, at (a) $I_0 = 2.13 \times 10^{16}$ q cm^{-2} s^{-1}, (b) $I_0 = 1.07 \times 10^{16}$ q cm^{-2} s^{-1}, (c) $I_0 = 5.33 \times 10^{15}$ q cm^{-2} s^{-1} and (d) $I_0 = 2.66 \times 10^{15}$ q cm^{-2} s^{-1}.

4.4.2.3 In the Presence of an Organic Substrate

Transients for oxygen reduction at a Pt UME were recorded in an aqueous aerated 1.0×10^{-3} mol dm^{-3} and oxygenated 1.0×10^{-2} mol dm^{-3} 4-chlorophenol (4-CP) solutions in the presence of 0.1 M $NaClO_4$ as supporting electrolyte. The organic substrate has a similar role to the hole scavenger by reacting with the photogenerated holes, or with the $^{\bullet}OH$ radicals formed by reaction of H_2O or OH^- with the holes. The transients for oxygen reduction at four different light intensities and for aerated and oxygenated conditions are shown in Figures 4.22 and 4.23, respectively. The transients are less sharp and take longer to reach steady-state, compared to those performed in triethanolamine, especially for the oxygenated solution. At first glance, it appears that triethanolamine is a better hole scavenger than 4-CP. On the other hand, it has to be recognised that for the oxygen reduction reaction to occur, the appropriate hole transfer reaction must also take place. For the 4-CP studies, a much lower concentration of 4-CP has been used, and it is likely that this is consumed significantly at the TiO_2 surface. Consequently, it is perhaps not surprising that the oxygen reduction process is slower than with triethanolamine. This issue is explored in the next chapter.

The transients for the aerated conditions were analysed using the Langmuir-Hinshelwood model and the best fits for the four light intensities are shown in Figure 4.24. The model simulation only fits the experimental data to the steady-state. Table 4.2 provides a summary of the rate constants obtained from the analysis of the data in Figure 4.24. The rate constants for oxygen reduction in the presence of 4-CP are lower than the ones in the presence of triethanolamine by a factor of three, with the likely reason for this given above. The transients for the oxygenated solution were not analysed because the steady-state was not reached.

Table 4.2 Values of the rate constants (mol cm^{-2} s^{-1}), estimated using a Lagmuir-Hinshelwood model, for the reduction of oxygen in an aerated 1.0×10^{-3} mol dm^{-3} 4-CP solution in the presence of 0.1 M $NaClO_4$ as supporting electrolyte.

I_0 q cm^{-2} s^{-1}	k_{lh} K_{O2}=9.63×10⁶ mol^{-1} cm^3	k_{lh} K_{O2}=4.89×10⁵ mol^{-1} cm^3
2.13×10^{16}	3.5×10^{-10}	3.4×10^{-9}
1.07×10^{16}	1.9×10^{-10}	1.7×10^{-9}
5.33×10^{15}	9.9×10^{-11}	8.2×10^{-10}
2.66×10^{15}	5.9×10^{-11}	4.8×10^{-10}

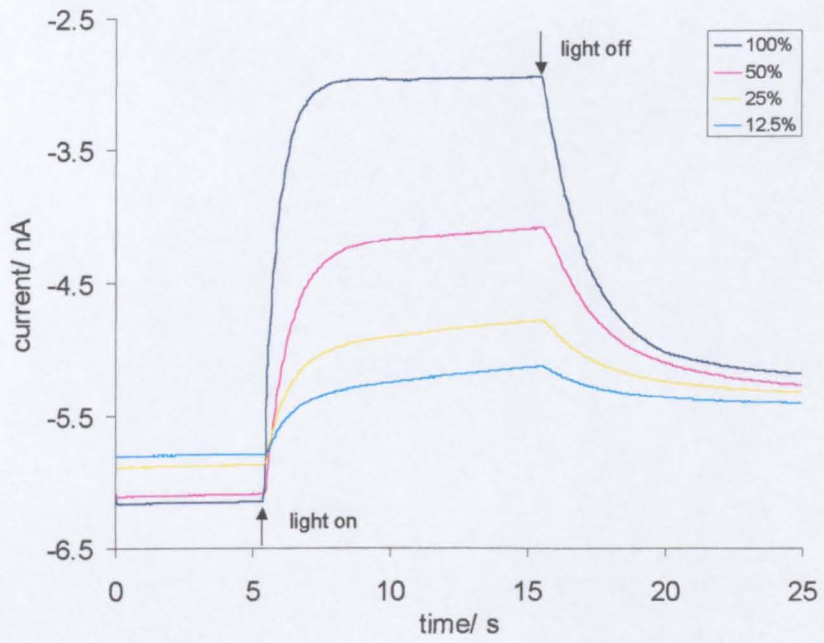

Figure 4.22 Phototransient responses at the Pt UME for the reduction of oxygen in an aqueous aerated 1.0×10^{-3} mol dm^{-3} 4-CP solution in the presence of 0.1 M $NaClO_4$ as supporting electrolyte. The tip-substrate distance was 19.6 μm.

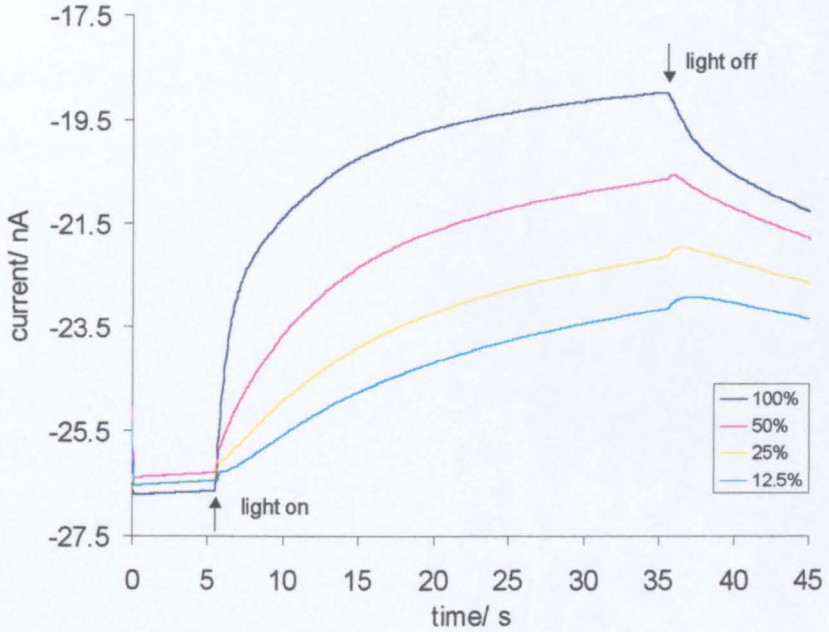

Figure 4.23 Phototransient responses at the Pt UME for the reduction of oxygen in an aqueous oxygenated 1.0×10^{-2} mol dm^{-3} 4-CP solution in the presence of 0.1 M $NaClO_4$ as supporting electrolyte. The tip-substrate distance was 20.4 μm.

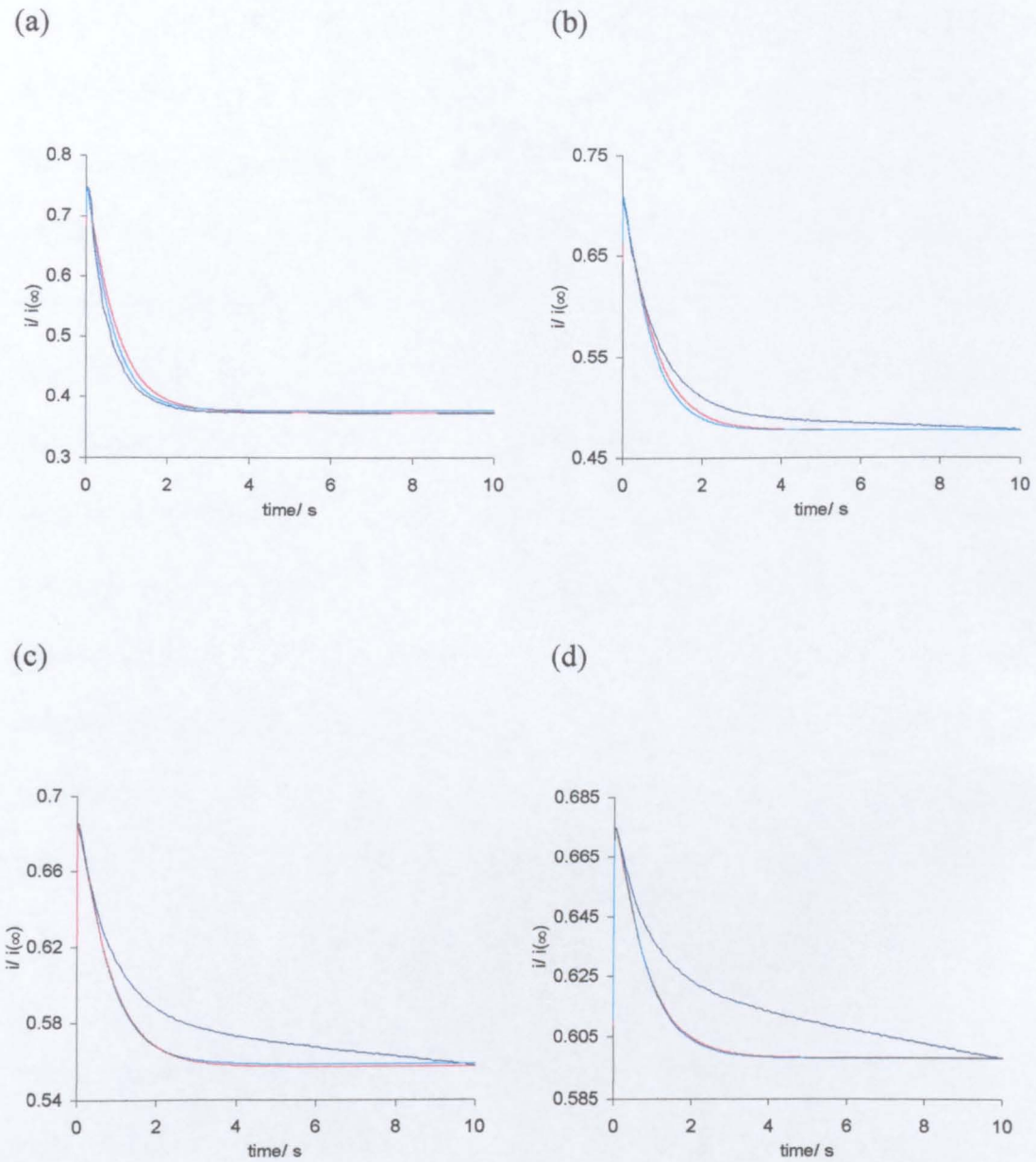

Figure 4.24 Experimental data (—) for oxygen reduction in an aerated 4-CP solution compared with the best fit theoretical simulations for the Langmuir-Hinshelwood model for (—) $K_{O2} = 9.63 \times 10^6$ mol^{-1} cm^3 and (—) $K_{O2} = 4.89 \times 10^5$ mol^{-1} cm^3, at (a) $I_0 = 2.13 \times 10^{16}$ q cm^{-2} s^{-1}, (b) $I_0 = 1.07 \times 10^{16}$ q cm^{-2} s^{-1}, (c) $I_0 = 5.33 \times 10^{15}$ q cm^{-2} s^{-1} and (d) $I_0 = 2.66 \times 10^{15}$ q cm^{-2} s^{-1}.

4.4.3 Development of a New Mechanistic Model for the Photoelectrochemical Reduction of Oxygen

A new model based on Langmuir-Hinshelwood kinetics was developed which accounted for the surface concentration of sites. As seen in the last sections the previous Langmuir-Hinshelwood model only fitted the transients to the steady-state. One explanation that was advanced was that oxygen molecules already pre-adsorbed at the TiO_2 surface must react before oxygen can adsorb from solution. Since the SECM method detects the loss of oxygen from solution, this therefore causes a delay in the transient response. In this new model the surface concentration of adsorption sites was introduced as an adjustable parameter to investigate its effect on the reduction kinetics of oxygen. The model is essentially the same as the one described in section 4.3.2 except that during the second part of the simulation, after the UV illumination is turned on, the boundary condition at the TiO_2 substrate (equation 4.29) is modified by an extra term which takes account of the pre-adsorbed oxygen on the surface:

$$t > t_{\text{switch}} \qquad j_z = -D_{\text{Ox}} \frac{\partial c_{\text{Ox,int}}}{\partial z} = \frac{k' K_{\text{Ox}} c_{\text{Ox,int}}}{1 + K_{\text{Ox}} c_{\text{Ox,int}}} - k'\theta \tag{4.46}$$

where θ is the fraction of sites occupied by the pre-adsorbed oxygen molecules. At the time at which the illuimination is switched on, θ_{initial} is calculated *viz:*

$$t = t_{\text{switch}} \qquad \theta_{initial} = \frac{K_{\text{Ox}} c_{\text{Ox,int}}}{1 + K_{\text{Ox}} c_{\text{Ox,int}}} \tag{4.47}$$

The rate of change of θ with time is given by:

$$N \frac{\partial \theta}{\partial t} = -k'\theta \tag{4.48}$$

where N is the density of sites (mol cm^{-2}).

Figures 4.25, 4.26 and 4.27 show the fits for several values of the surface concentration of sites, N, for oxygen reduction in the presence of triethanolamine, for the four light intensities and for aerated, 50% O_2 and oxygenated conditions, respectively. The new model provides a better fit than the previous L-H model, however, in some cases the model simulation still does not fit the experimental data completely. It should be recognised that the model is a simplification, but does at least provide a likely explanation of the experimental observations. A possible explanation for the deviation between experiment and theory is that the value of the equilibrium adsorption constant for oxygen used (K_{O2} = 9.63×10^6 mol^{-1} cm^3)[33] was obtained in the dark and the value for K_{O2} in light conditions could be different. Also, the TiO_2 surface is extremely heterogeneous, with some sites that are more active than others, but the simplified model assumes that all the sites react at the same rate. While more detailed models could be developed, they would involve additional adjustable parameters and at this stage, such a treatment is not warranted.

A general trend that can be observed from Figures 4.25-4.27 is that the value of the surface concentration of sites, N, increases with the increase in oxygen concentration. This is in agreement with the reasoning that the oxygen molecules already adsorbed on the surface must react before oxygen from solution can adsorb and react, which will cause a delay in the transient response. The more surface adsorption sites, the bigger the delay observed, as can be seen in the oxygenated condition transients. This also provides evidence that the reduction process is controlled by surface kinetics. This analysis also makes clear the fact that oxygen reduction at TiO_2 involves adsorption as a major factor.

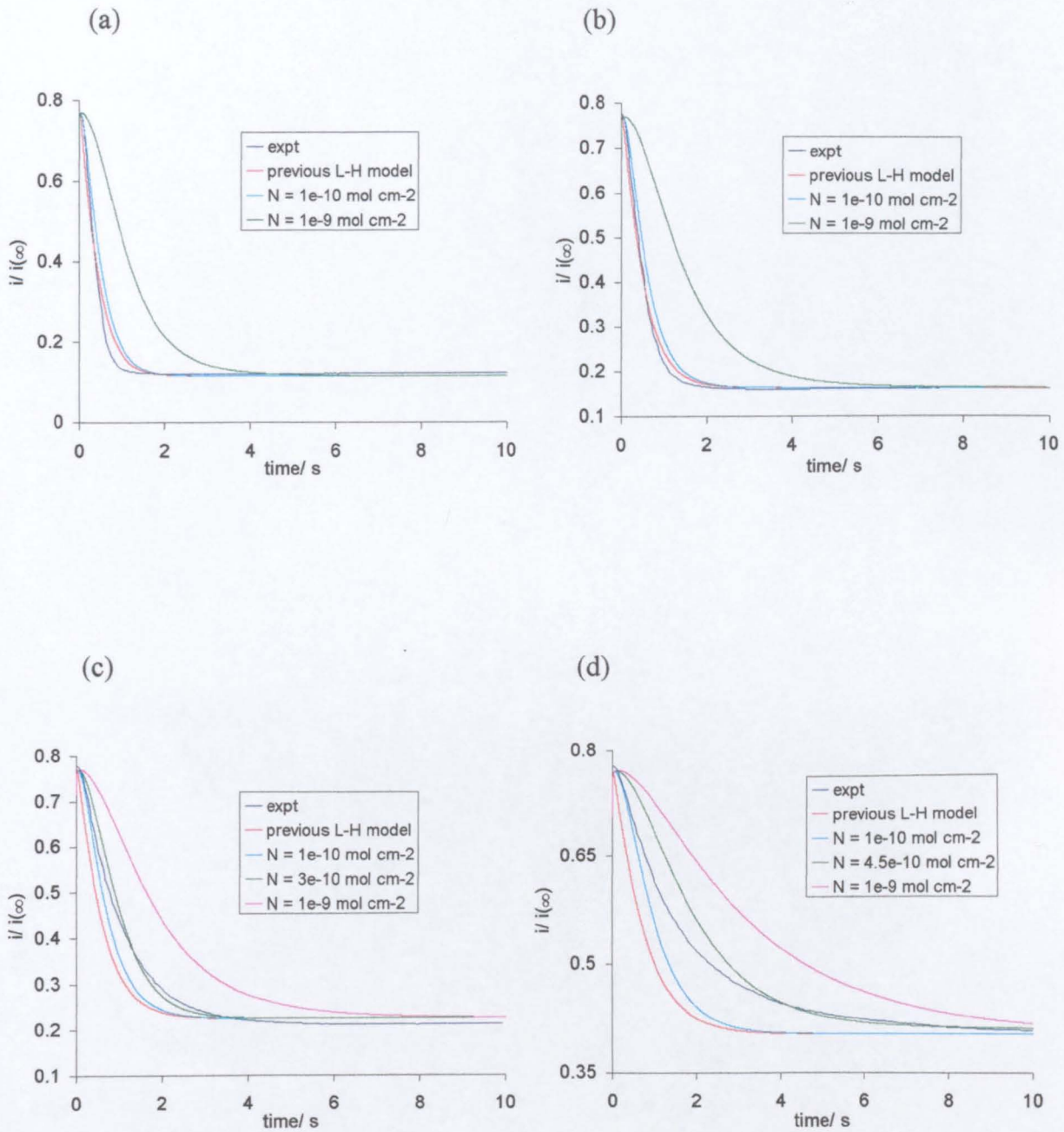

Figure 4.25 Experimental data for oxygen reduction in an aerated triethanolamine solution compared with the best fit theoretical simulations for the previous and new Langmuir-Hinshelwood model with $K_{O2} = 9.63 \times 10^6$ mol^{-1} cm^3, at (a) $I_0 = 2.13 \times 10^{16}$ q cm^{-2} s^{-1}, (b) $I_0 = 1.07 \times 10^{16}$ q cm^{-2} s^{-1}, (c) $I_0 = 5.33 \times 10^{15}$ q cm^{-2} s^{-1} and (d) $I_0 = 2.66 \times 10^{15}$ q cm^{-2} s^{-1}.

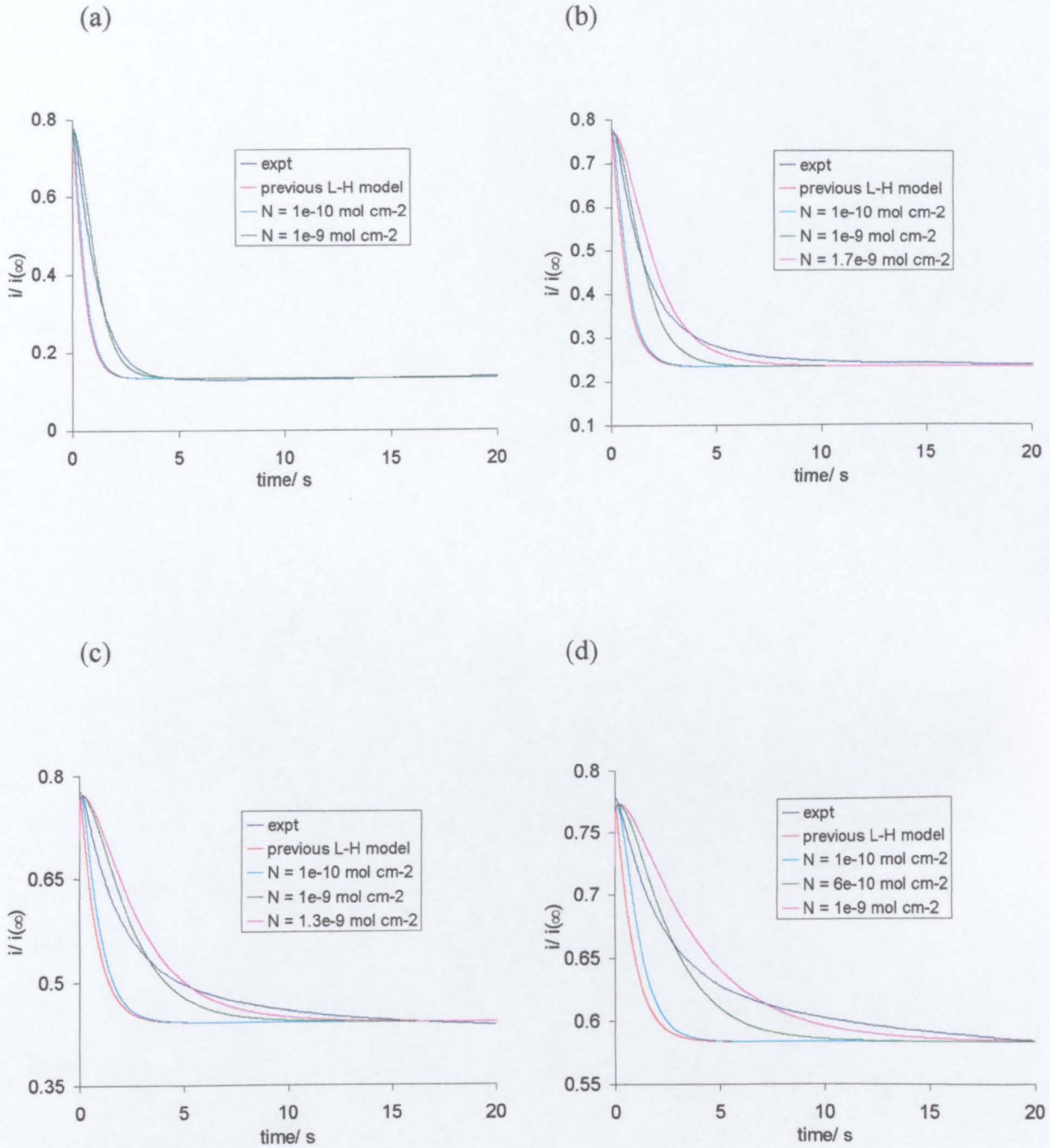

Figure 4.26 Experimental data for oxygen reduction in a 50% O_2 triethanolamine solution compared with the best fit theoretical simulations for the previous and new Langmuir-Hinshelwood model with $K_{O2} = 9.63 \times 10^6$ mol^{-1} cm^3, at (a) $I_0 = 2.13 \times 10^{16}$ q cm^{-2} s^{-1}, (b) $I_0 = 1.07 \times 10^{16}$ q cm^{-2} s^{-1}, (c) $I_0 = 5.33 \times 10^{15}$ q cm^{-2} s^{-1} and (d) $I_0 = 2.66 \times 10^{15}$ q cm^{-2} s^{-1}.

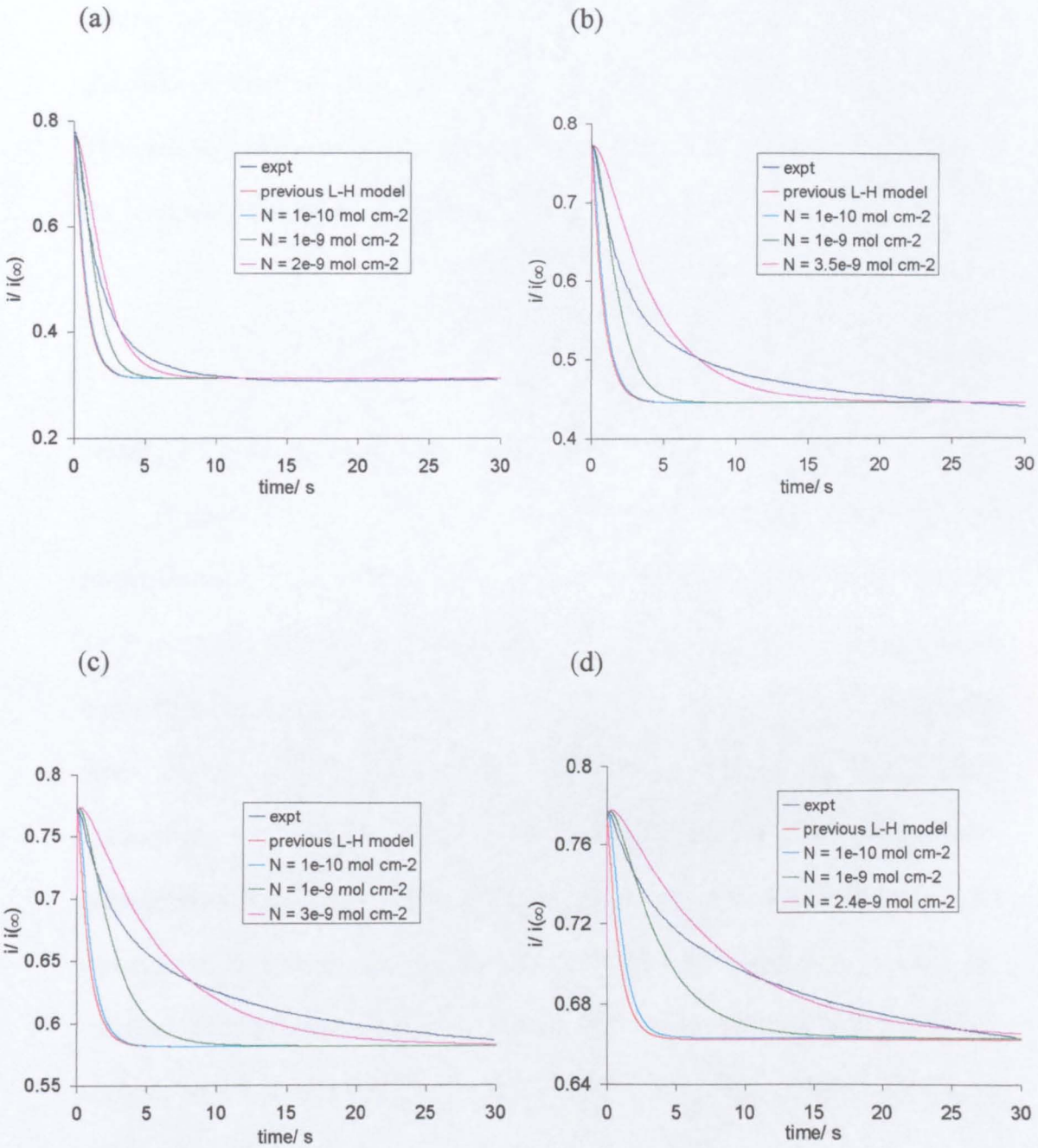

Figure 4.27 Experimental data for oxygen reduction in a oxygenated triethanolamine solution compared with the best fit theoretical simulations for the previous and new Langmuir-Hinshelwood model with $K_{O2} = 9.63 \times 10^6$ mol^{-1} cm^3, at (a) $I_0 = 2.13 \times 10^{16}$ q cm^{-2} s^{-1}, (b) $I_0 = 1.07 \times 10^{16}$ q cm^{-2} s^{-1}, (c) $I_0 = 5.33 \times 10^{15}$ q cm^{-2} s^{-1} and (d) $I_0 = 2.66 \times 10^{15}$ q cm^{-2} s^{-1}.

4.5 Estimating the Quantum Efficiency

Since the quantum efficiency is an important parameter in the photomineralisation process, it is worth estimating its value for the photoelectrochemical reduction of oxygen at TiO_2 films presented in this chapter. The quantum efficiency can be estimated from the following expression related to the Langmuir-Hinshelwood model:

$$\phi = \frac{k_{lh}\left(\frac{K_{O_2}[O_2]^*}{1+K_{O_2}[O_2]^*}\right)N_A}{I_0} \tag{4.49}$$

where $[O_2]^*$ is the bulk concentration of oxygen.

Tables 4.3 and 4.4 show the estimated quantum yields for the photoelectrochemical reduction of oxygen in the triethanolamine solution and the 4-CP solution, respectively. It was found that there was a slight increase in the quantum efficiency with a decrease in the light flux intensity. This suggests that when the light flux intensity is relatively high, the rate of charge-carrier recombination increases compared to interfacial charge transfer, and so the entire photoprocess tends to a lower quantum efficiency. A likely reason for this observation is that by driving the surface photoelectrochemical process, the reaction tends to become more limited by the transport of reagents to the TiO_2 surface, which is restricted in the SECM geometry. Consequently, there is an enhanced likelihood of charge recombination.

Table 4.3 Estimated quantum yields, related to the Lagmuir-Hinshelwood model, for the photoreduction of oxygen at TiO_2 films in a 5.0×10^{-2} mol dm^{-3} triethanolamine solution in the presence of 0.1 M $NaClO_4$ as supporting electrolyte under aerated, 50% O_2 and oxygenated conditions.

	aerated condition		50% O_2		oxygenated condition	
I_0 q cm^{-2} s^{-1}	ϕ $K_{O2}=9.63\times10^6$ mol^{-1} cm^3	ϕ $K_{O2}=4.89\times10^5$ mol^{-1} cm^3	ϕ $K_{O2}=9.63\times10^6$ mol^{-1} cm^3	ϕ $K_{O2}=4.89\times10^5$ mol^{-1} cm^3	ϕ $K_{O2}=9.63\times10^6$ mol^{-1} cm^3	ϕ $K_{O2}=4.89\times10^5$ mol^{-1} cm^3
2.13×10^{16}	0.022	0.046	0.036	0.096	0.037	0.067
1.07×10^{16}	0.034	0.067	0.051	0.096	0.049	0.075
5.33×10^{15}	0.053	0.096	0.053	0.085	0.056	0.075
2.66×10^{15}	0.056	0.084	0.058	0.080	0.067	0.086

Table 4.4 Estimated quantum yields, related to the Lagmuir-Hinshelwood model, for the photoreduction of oxygen at TiO_2 films in an aerated 1.0×10^{-3} mol dm^{-3} 4-CP solution in the presence of 0.1 M $NaClO_4$ as supporting electrolyte.

I_0 q cm^{-2} s^{-1}	ϕ $K_{O2}=9.63\times10^6$ mol^{-1} cm^3	ϕ $K_{O2}=4.89\times10^5$ mol^{-1} cm^3
2.13×10^{16}	7.0×10^{-3}	0.011
1.07×10^{16}	7.6×10^{-3}	0.010
5.33×10^{15}	7.9×10^{-3}	0.010
2.66×10^{15}	9.4×10^{-3}	0.012

4.6 Conclusions

The development of a new approach to investigate the kinetics of interfacial photochemical process, using the SECM technique, has allowed the successful study, at the microscopic level, of the photoelectrochemical reduction kinetics of oxygen at a TiO_2 film. The results presented in this chapter have demonstrated a significant depletion of the oxygen concentration at/ in the vicinity of the illuminated TiO_2 surface, which provides a new insight into the photomineralisation process. Theoretical models have been developed that allowed the kinetics of the photoreduction of oxygen to be determined. Of the models developed, the Langmuir-Hinshelwood model is the one which provides a better agreement with the experimental data. However, for the lower light intensities and for the higher oxygen concentrations, the model only fits the transient to the steady-state. To improve the fit between the experimental data and the model simulation, the Langmuir-Hinshelwood model was modified by taking into account pre-adsorbed oxygen at the TiO_2 surface. This provided evidence that oxygen reduction at TiO_2 involves adsorption as a major factor.

References

1. H. Gerischer and A. Heller, *J. Phys. Chem.*, **1991**, 95, 5261.

2. H. Gerischer and A. Heller, *J. Electrochem. Soc.*, **1992**, 139, 113.

3. C. M. Wang, A. Heller and H. Gerischer, *J. Am. Chem. Soc.*, **1992**, 114, 5230.

4. S. Upadhya and D. F. Ollis, *J. Phys. Chem. B*, **1997**, 101, 2625.

5. K. Vinodgopal, U. Stafford, K. A. Gray and P. V. Kamat, *J. Phys. Chem.*, **1994**, 98, 6797.

6. J. Schwitzgebel, J. G. Ekerdt, H. Gerischer and A. Heller, *J. Phys. Chem.*, **1995**, 99, 5633.

7. K. Ikeda, H. Sakai, R. Baba, K. Hashimoto and A. Fujishima, *J. Phys. Chem. B*, **1997**, 101, 2617.

8. L. Cermenati, P. Pichat, C. Guillard and A. Albini, *J. Phys. Chem. B*, **1997**, 101, 2650.

9. C. Kormann, D. W. Bahnemann and M. R. Hoffmann, *Environ. Sci. Technol.*, **1991**, 25, 494.

10. M. Bideau, B. Claudel, L. Faure and H. Kazouan, *J. Photochem. Photobiol. A: Chem.*, **1991**, 61, 269.

11. J. M. Kesselman, G. A. Shreve, M. R. Hoffmann and N. S. Lewis, *J. Phys. Chem.*, **1994**, 98, 13385.

12. J. P. Hoare, *The Electrochemistry of Oxygen*, Interscience, New York, 1968.

13. D. J. Schiffrin in *Specialist Periodical Reports on Electrochemistry*, Royal Society of Chemistry, London, 1985, vol. 6, ch. 4, p. 126.

14. E. J. M. O'Sullivan and E. J. Calvo in *Comprehensive Chemical Kinetics*, R. G. Compton (Ed.), Elsevier, Amsterdam, 1987, p. 247.

15. A. J. Appleby, *J. Electroanal. Chem.*, **1993**, 357, 117.

16. D. Pletcher and S. Sotiropoulos, *J. Electroanal. Chem.*, **1993**, 356, 109.

17. D. Pletcher and S. Sotiropoulos, *J. Chem. Soc. Faraday Trans.*, **1995**, 91, 457.

18. A. Mills and S. Le Hunte, *J. Photochem. Photobiol. A: Chem.*, **1997**, 108, 1.

19. A. Mills and J. Wang, *J. Photochem. Photobiol. A: Chem.*, **1998**, 118, 53.

20. J. Kwak and A. J. Bard, *Anal. Chem.*, **1989**, 61, 1221.

21. (a) J. V. Macpherson and P. R. Unwin, *J. Phys. Chem.*, **1994**, 98, 1704. (b) J. V. Macpherson and P. R. Unwin, *J. Phys. Chem.*, **1994**, 98, 3109. (c) J. V. Macpherson and P. R. Unwin, *J. Phys. Chem.*, **1995**, 99, 3338. (d) J. V. Macpherson and P. R. Unwin, *J. Phys. Chem.*, **1995**, 99, 14824. (e) J. V. Macpherson and P. R. Unwin, *J. Phys. Chem.*, **1996**, 100, 19475.

22. Y. Saito, *Rev. Polarogr. Jpn.*, **1968**, 15, 177.

23. D. W. Peaceman and H. H. Rachford, *J. Soc. Ind. Appl. Math.*, **1955**, 3, 28.

24. (a) P. R. Unwin and A. J. Bard, *J. Phys. Chem.*, **1991**, 95, 7814. (b) A. J. Bard, M. V. Mirkin, P. R. Unwin and D. O. Wipf, *J. Phys. Chem.*, **1992**, 96, 1861. (c) D. T. Pierce, P. R. Unwin and A. J. Bard, *Anal. Chem.*, **1992**, 64, 1795. (d) P. R. Unwin and A. J. Bard, *J. Phys. Chem.*, **1992**, 96, 5035.

25. A. L. Barker, J. V. Macpherson, C. J. Slevin and P. R. Unwin, *J. Phys. Chem. B*, **1998**, 102, 1586.

26. A. L. Barker, P. R. Unwin, S. Amemiya, J. Zhou and A. J. Bard, *J. Phys. Chem. B*, **1999**, 103, 7260.

27. C. J. Slevin, J. V. Macpherson and P. R. Unwin, *J. Phys. Chem. B*, **1997**, 101, 10851.

28. R. D. Martin and P. R. Unwin, *J. Electroanal. Chem.*, **1997**, 439, 123.

29. (a) L. Lapidus and G. F. Pinder, *Numerical Solutions of Partial Differential Equations in Science and Engineering*, Wiley, New York, 1982. (b) W. F. Ames, *Numerical Methods of Partial Differential Equations*, Wiley, New York, 1977.

30. C. N. Rusu and J. T. Yates Jr., *Langmuir*, **1997**, 13, 4311.

31. E. Pelizzetti and C. Minero, *Electrochim. Acta*, **1993**, 38, 47.

32. H. Sakai, R. Baba, K. Hashimoto, A. Fujishima and A. Heller, *J. Phys. Chem.*, **1995**, 99, 11896.

33. L. Rideh, A. Wehrer, D. Ronze and A. Zoulalian, *Catalysis Today*, **1999**, 48, 357.

CHAPTER 5

PHOTOMINERALISATION KINETICS OF A MODEL ORGANIC POLLUTANT SENSITISED BY TiO_2 FILMS

In this chapter, SECM is used as a new approach for quantitatively investigating the photomineralisation kinetics of a model organic pollutant, 4-chlorophenol (4-CP), in aerated and oxygenated aqueous solutions at supported TiO_2 films. A potentiometric Ag/AgCl UME, positioned at a known distance above the TiO_2 film, was used to monitor directly the Cl^- production from the photomineralisation of 4-CP. Both the effect of light intensity and 4-CP concentration were investigated. A theoretical model, which employs a Langmuir-Hinshelwood type kinetic equation, has been developed to interpret the kinetics of the photomineralisation process and determine the associated quantum efficiency.

5.1 Introduction

The use of semiconductors as photocatalysts in the photomineralisation of organic pollutants in water by oxygen has been, and continues to be, an active field of research.[1,2] The mechanism of TiO_2-sensitised photodegradation of organic pollutants was reviewed in chapter 1. The photo-oxidative mineralisation of 4-chlorophenol by oxygen and sensitised by TiO_2 has been the subject of numerous, detailed characterisation studies, with TiO_2 either in the form of a dispersion[3,4,5,6,7,8] or immobilised as a film on a support.[9,10,11,12,13,14] The role of mass transport for immobilised systems has also been investigated.[14,15,16] In these systems it is usually found that the overall rate of reaction is, at least in part, controlled by the rate of diffusion/convection mass transfer to and from the

photocatalyst.[17,18] Mills *et al.*[14] have investigated the rate of degradation of 4-CP in a stirred reactor where mass transfer was considered to be sufficiently high to have a negligible effect on the rate. Ahmed *et al.*[16] have used the channel flow method with electrochemical detection to identify the conditions under which mass transfer is important in controlling the photomineralisation rates of four chlorophenols.

The mechanism of 4-CP photocatalytic degradation sensitised by TiO_2 has also been the subject of detailed studies.[3,4,13,14] The reaction scheme illustrating the likely mechanistic pathways to the formation of the major intermediates is shown in Figure 5.1.[14] The generation of the intermediates can be explained through reaction schemes which initially involve $^{\bullet}OH$ radical attack on 4-CP to give the 4-chlorodihydroxycyclohexadienyl radical. Reduction by a conduction band electron yields hydroquinone (HQ) and Cl^-. The other major intermediates are 4-chlorocatechol (4-CC) and benzoquinone (BQ). The intermediate product distribution is pH dependent.[7] The pathway leading to the formation of HQ is preponderant in the pH range 3.4-6.0,[3] but under very acidic conditions (*ca.* pH 2) 4-CC appears to be the most stable of the reaction intermediates.[4,14] With prolonged irradiation all the 4-CP is eventually converted to CO_2, H_2O and HCl.

Usually, chromatographic techniques are used in the investigation of the photomineralisation of 4-CP sensitised by TiO_2. Quantitative and qualitative analyses of the reaction intermediates are carried out by HPLC, CO_2 evolution is usually measured by GC and Cl^- generation is measured by ion chromatography.[3,4,5] There is only one report in the literature where a potentiometric UME was used to monitor the Cl^- production from the photomineralisation of 2,4-dichlorophenol sensitised by TiO_2.[19] The production of

Cl^- was modelled on the basis of a heterogeneous process at the TiO_2/aqueous interface, however there was a significant deviation of the experimental data from theory.

The aim of this chapter is to use the SECM technique in the investigation of the photomineralisation of 4-CP sensitised by TiO_2 films and to develop a theoretical model to interpret the kinetics of the photomineralisation process.

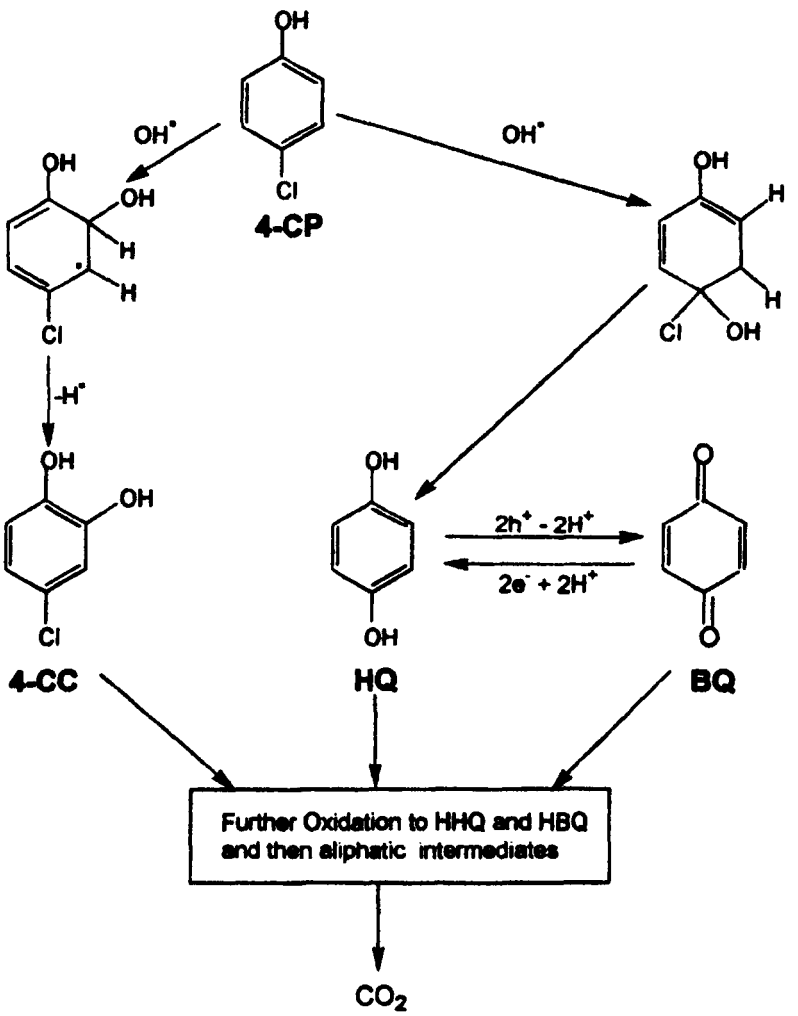

Figure 5.1 Reaction scheme illustrating the likely mechanistic pathways to the formation of the major intermediates, 4-chlorocatechol (4-CC), hydroquinone (HQ) and benzoquinone (BQ), generated during the photomineralisation of 4-CP sensitised by TiO_2.[14]

5.2 Theory

Given the experimental data that follows, and that obtained for oxygen photoelectrochemical reduction in chapter 4, it is reasonable to consider that O_2 and Cl^- diffusion is important, but 4-CP diffusion can be neglected. Time-dependent diffusion equations appropriate to the axisymmetric cylindrical geometry of the SECM can be written for each species of interest:

$$\frac{\partial c_{O_2}}{\partial t} = D_{O_2}\left[\frac{\partial^2 c_{O_2}}{\partial r^2} + \frac{1}{r}\frac{\partial c_{O_2}}{\partial r} + \frac{\partial^2 c_{O_2}}{\partial z^2}\right] \tag{5.1}$$

$$\frac{\partial c_{Cl^-}}{\partial t} = D_{Cl^-}\left[\frac{\partial^2 c_{Cl^-}}{\partial r^2} + \frac{1}{r}\frac{\partial c_{Cl^-}}{\partial r} + \frac{\partial^2 c_{Cl^-}}{\partial z^2}\right] \tag{5.2}$$

Initially oxygen is present in the solution with concentration $c^*_{O_2}$ and there is no Cl^- present, therefore the initial condition is,

$$t = 0; \qquad 0 \le r \le r_g,\ 0 \le z \le d: \ c_{O_2} = c^*_{O_2}\ , c_{Cl^-} = 0 \tag{5.3}$$

The boundary conditions for the model can be summarised as

$$z = 0, \qquad 0 < r \le r_g \quad : \quad D_{O_2}\frac{\partial c_{O_2}}{\partial z} = 0\ , \qquad D_{Cl^-}\frac{\partial c_{Cl^-}}{\partial z} = 0 \tag{5.4}$$

$$r > r_g, \qquad 0 < z < d \quad : \quad c_{O_2} = c^*_{O_2}\ , \qquad c_{Cl^-} = 0 \tag{5.5}$$

$$r = 0, \qquad 0 < z < d \quad : \quad D_{O_2}\frac{\partial c_{O_2}}{\partial r} = 0\ , \qquad D_{Cl^-}\frac{\partial c_{Cl^-}}{\partial r} = 0 \tag{5.6}$$

These conditions have similar meaning to those described in section 4.3.2 except now the UME is a passive potentiometric probe and hence is inert with respect to Cl^- and O_2 (equation 5.4).

The following boundary condition applies to the TiO_2 surface:

$$z = d, \qquad 0 < r < r_g \quad : D_{O_2}\frac{\partial c_{O_2}}{\partial z} = -nD_{Cl^-}\frac{\partial c_{Cl^-}}{\partial z} = -\frac{k' K_{O_2} c_{O_2,int}}{1 + K_{O_2} c_{O_2,int}} \tag{5.7}$$

The problem was cast into dimensionless form and solved using ADIFDM. An analogous iterative procedure was used to that described in section 4.3.2 to first calculate the radial concentrations of O_2 in the second half time step, and then the radial concentration of Cl^-. It was assumed that O_2 undergoes a two electron reduction to H_2O_2, so $n = 2$. The simulation provided the steady-state concentration profile of Cl^- in the radial direction along the surface of the potentiometric microelectrode probe.

5.3 Experimental Results and Discussion

5.3.1 Preliminary Studies: Stability and Sensitivity of the Ag/AgCl UME to Monitor the Photomineralisation of 4-CP

Since the light beam directly illuminates the Ag/AgCl UME probe, with the SECM-optical fibre technique, it was important to ensure the validity of this new potentiometric SECM approach. Accordingly, a 25 μm diameter Ag/AgCl UME was positioned over the TiO_2-coated optical fibre in an aerated ultrapure aqueous solution, and the potential response during illumination was recorded at the tip Ag/AgCl UME against a SCE reference electrode. Little change of potential was observed at the UME as a result of direct illumination, as shown in Figure 5.2. This behaviour demonstrates that the detector electrode is relatively photostable. The small changes in potential seen are negligible compared to those observed during Cl^- detection for photomineralisation, as described latter.

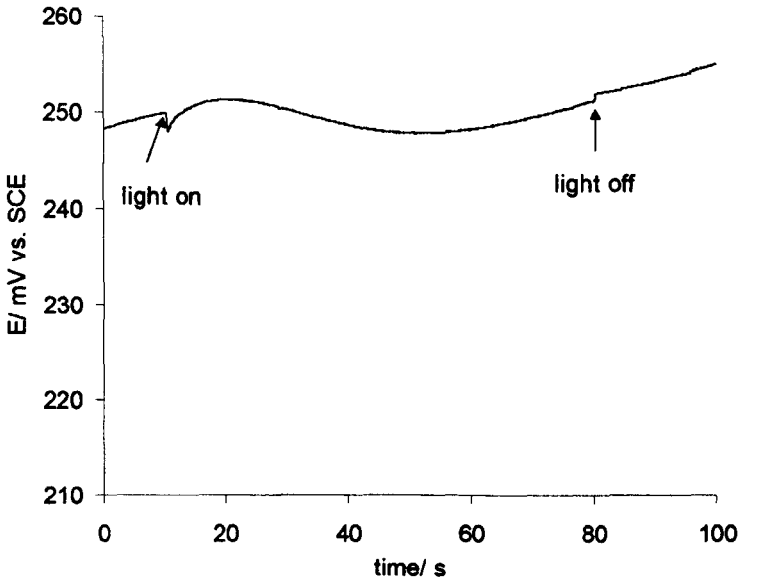

Figure 5.2 Potential response of the Ag/AgCl UME vs. SCE recorded in ultrapure water. The tip-substrate distance, determined by video microscopy, was 20 μm.

5.3.2 4-CP Electrochemistry

It would be important to know if the Cl^- formed during the photomineralisation process is mainly generated from 4-CP molecules already adsorbed at the TiO_2 surface, or if the 4-CP concentration is being depleted in the vicinity of the illuminated surface. A way to find out would be to run a voltammogram close to the TiO_2 surface in the dark and with illumination. Firstly, voltammograms for 4-CP oxidation at a 25 μm diameter Pt UME were recorded away from the TiO_2 surface in an aqueous 1.0×10^{-3} mol dm^{-3} 4-CP solution in the presence of 0.1 M $NaClO_4$ as supporting electrolyte. A series of voltammograms were obtained at increasing sweep rates because, as can be seen from Figure 5.3, the electrode response was blocked during the oxidation of 4-CP. A way around this was to step the potential from 0 to 1 V and record the chronoamperometric response on a shorter timescale (millisecond range) for the diffusion-limited oxidation of 4-CP. Transients were performed close to the TiO_2 surface (tip-substrate distance of 17 μm) first in the dark and then after 10 s illumination.

Figure 5.4 shows that the transient response is essentially identical under the two sets of conditions. The current is due mainly to 4-CP diffusion to the electrode which, in turn, depends on the local concentration. Since the response is similar in both cases, this indicates that the 4-CP in solution was not depleted by illumination on the timescale of this measurement, which means that the Cl^- formed in the experiments discussed later is generated mainly from the photomineralisation of 4-CP molecules already adsorbed at the TiO_2 surface.

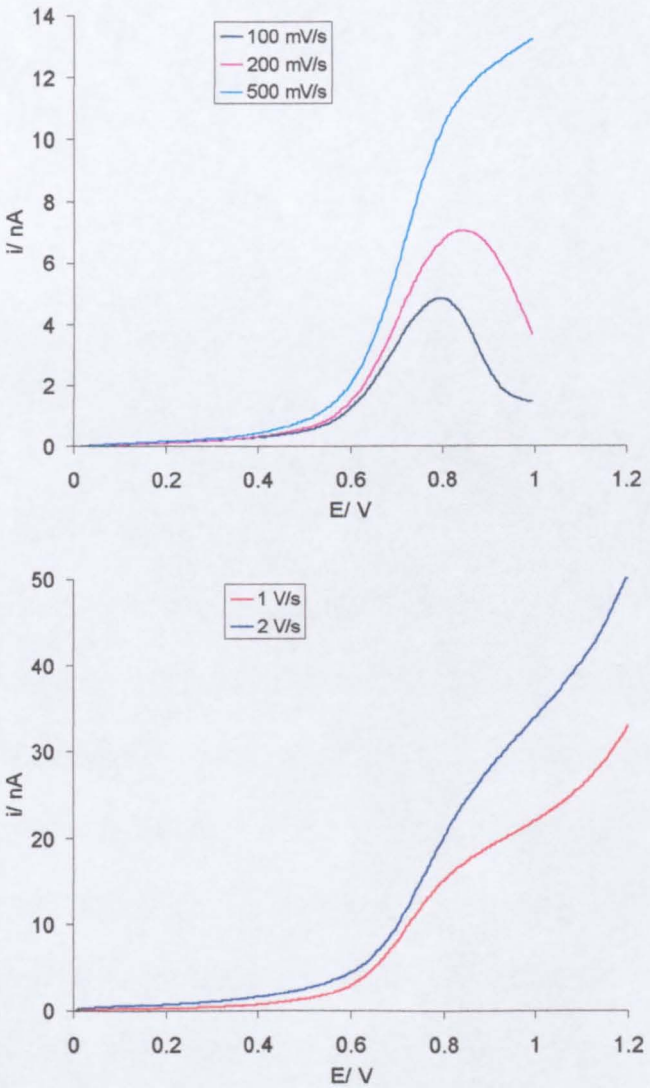

Figure 5.3 Voltammograms for 4-CP oxidation at a 25 μm diameter Pt UME recorded in the bulk of an aqueous 1.0×10^{-3} mol dm^{-3} 4-CP solution in the presence of 0.1 M $NaClO_4$ as supporting electrolyte.

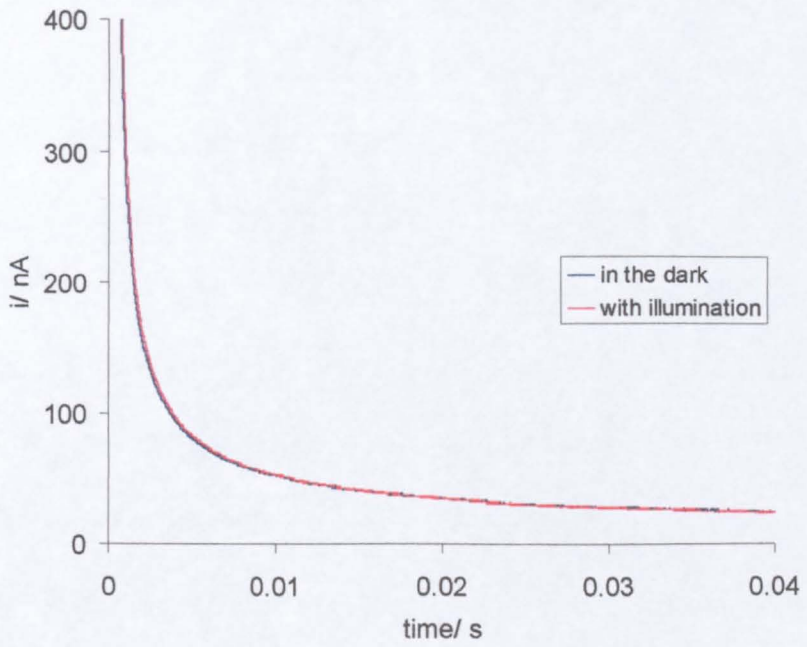

Figure 5.4 Chronoamperometric response for the oxidation of 4-CP after stepping the potential from 0 to 1 V. The transients were performed with a 25 μm diameter Pt UME positioned 17 μm away from the TiO_2 surface in an aqueous 1.0×10^{-3} mol dm^{-3} 4-CP solution in the presence of 0.1 M $NaClO_4$ as supporting electrolyte.

5.3.3 Photomineralisation of 4-CP

The photomineralisation of an aerated 1.0×10^{-3} mol dm^{-3} 4-CP solution in the presence of 0.1 M $NaClO_4$ as supporting electrolyte was monitored by recording the potential response due to illumination at the tip Ag/AgCl UME against SCE, as a function of tip-substrate separation. Typical potentiometric phototransients resulting from UV-excitation of the TiO_2 surface for two tip-substrate separation distances are shown in Figure 5.5. The transients clearly demonstrate the high sensitivity of the system. When the illumination was switched on, the potential difference between the indicator and reference electrode significantly moved in the negative direction, resulting in a *ca.* 49 – 31 mV change in potential (depending on tip-substrate distance) and then reached a

plateau. This behaviour is attributed to the formation of a concentration gradient of Cl^- at the illuminated TiO_2 surface, which after a certain period of illumination attains a constant value. It was shown in the last chapter that there is a significant depletion of oxygen near the illuminated TiO_2 surface. Since oxygen plays an active role in the photomineralisation process by scavenging the photogenerated electrons, a depletion in oxygen concentration will retard the trapping of the electrons. Such a process will promote enhanced electron-hole recombination, making the photomineralisation less efficient. When the illumination was switched off, the tip potential returned towards the initial dark value, indicating that the surface photomineralisation process had terminated. A schematic representation of the formation of Cl^- at the illuminated TiO_2 film is shown in Figure 5.6.

A calibration curve of $[Cl^-]$ vs. potentiometric response for an Ag/AgCl UME (Figure 5.7; see also section 2.1.2) was used to convert the observed potentials into Cl^- concentration, as shown in Figure 5.8. It is apparent from the data in Figure 5.8 that at the closest distance more Cl^- is formed, indicating that the photomineralisation of 4-CP obviously follows a heterogeneous process at the excited catalyst surface to produce Cl^- which will then diffuse into the solution gap between the TiO_2 surface and the probe, before being detected at the Ag/AgCl UME. When the tip-substrate distance increased, the response of the indicator electrode became less pronounced, and thus less Cl^- was detected at the UME. This is because at longer tip-substrate distances Cl^- escapes from the tip-substrate gap by diffusion, with the result that its concentration does not increase as significantly as that detected with a thinner tip-substrate domain.

In the subsequent investigations on the photomineralisation kinetics of 4-CP that were carried out, tip-substrate distances between 16 – 19 μm were chosen to enhance the sensitivity of the method.

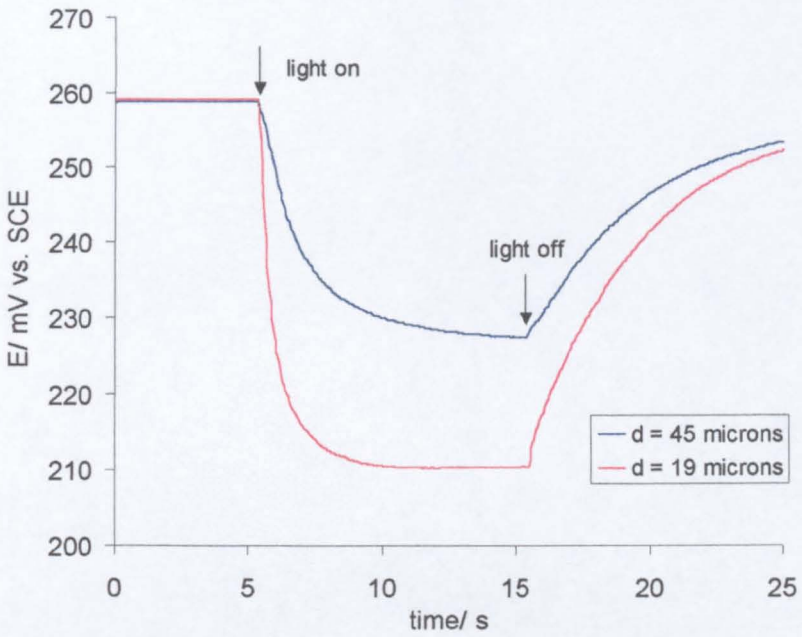

Figure 5.5 Potential response of the Ag/AgCl indicator electrode for two tip-substrate distances during the photomineralisation of an aerated 1.0×10^{-3} mol dm^{-3} 4-CP solution in the presence of 0.1 M $NaClO_4$ as supporting electrolyte.

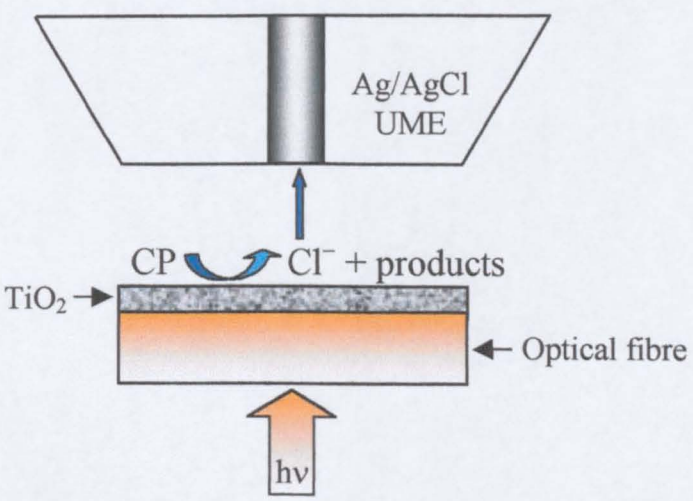

Figure 5.6 Schematic representation showing the formation of Cl^- from the photomineralisation of 4-CP at an illuminated TiO_2 film.

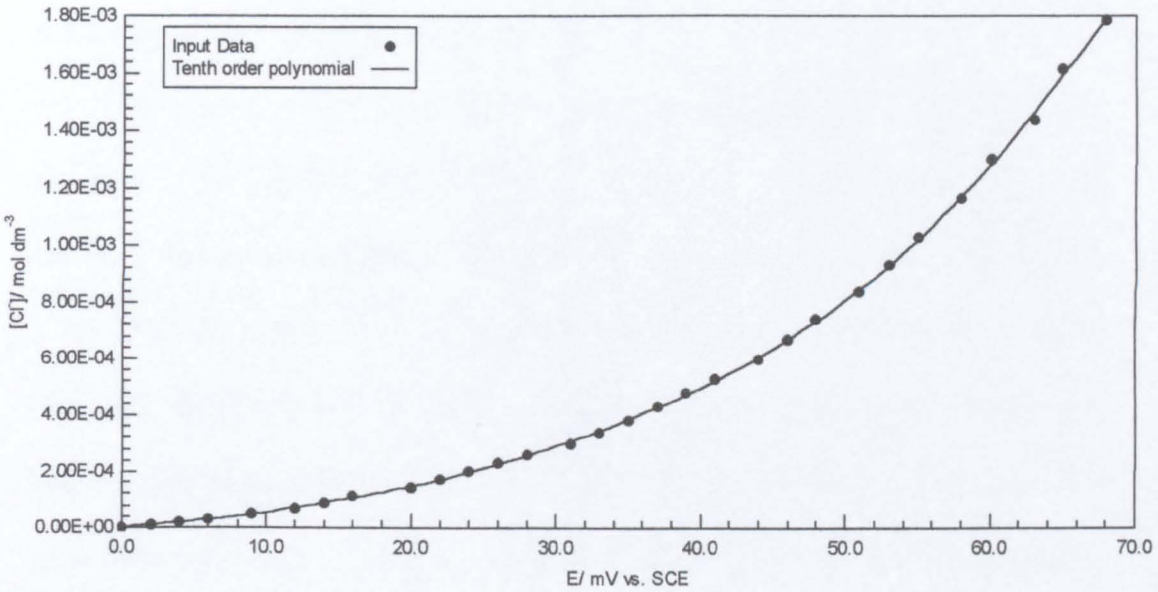

Figure 5.7 Calibration curve of [Cl^-] vs. potentiometric response for an Ag/AgCl UME (a = 12.5 μm).

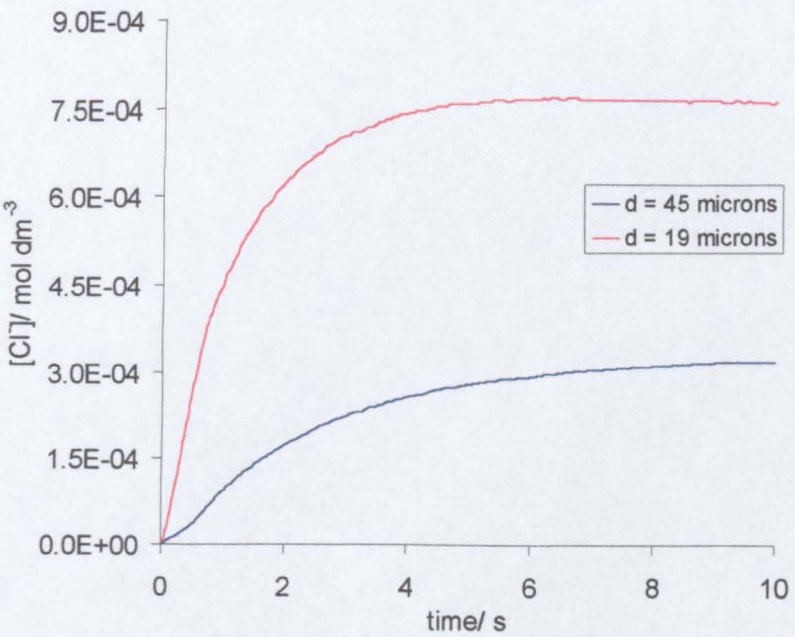

Figure 5.8 Photogenerated [Cl^-] detected at the Ag/AgCl UME during the photomineralisation of an aerated 1.0×10^{-3} mol dm^{-3} 4-CP solution in the presence of 0.1 M $NaClO_4$ as supporting electrolyte.

5.3.4 The Kinetics of 4-CP Photomineralisation: Light Intensity Effect

5.3.4.1 In an Aerated 4-CP Solution

It is well established that the photomineralisation rate depends on the intensity of the incident light.[14,18,20] Accordingly, the influence of the light flux intensity was investigated by using neutral density filters which only transmitted 50%, 25% and 12.5% of the incident light intensity. The potential response of the Ag/AgCl UME, positioned 17.4 μm away from the TiO_2 film, during the photomineralisation of an aerated 1.0×10^{-3} mol dm^{-3} 4-CP solution in the presence of 0.1 M $NaClO_4$ as supporting electrolyte, at the four light intensities, is shown in Figure 5.9. The corresponding photogenerated [Cl^-] is given in Figure 5.10. The results were analysed using the theoretical model developed, which employs a Langmuir-Hinshelwood type kinetic equation, and the best fits to the experimental data are also shown in Figure 5.10. The values of the initial rate of 4-CP photomineralisation are shown in Table 5.1. The model simulation provides a good fit to the experimental data and the estimated rate constants are closely proportional to the incident light intensity. Similar behaviour was found by Mills and Wang[14,18] in their stirred reactor studies on the photomineralisation of 4-CP by TiO_2 films.

It is worth comparing the rate of Cl^- formation in the photomineralisation process with the rate of oxygen consumption at the illuminated TiO_2 surface at a similar light intensity. Comparison of the rate constants for photomineralisation with the rate constants for oxygen reduction in an aerated 4-CP solution (obtained in chapter 4, section 4.4.2.3, for $K_{O2} = 9.63\times10^6$ mol^{-1} cm^3) shows that there is a direct correlation between the loss of oxygen and the formation of Cl^-. This close

correlation strongly suggests that the flux matching ideas of Lewis[21] (section 4.3.1) represents a good description of the photomineralisation process.

Table 5.1 Values of the rate constants, estimated using a Langmuir-Hinshelwood model, for the formation of Cl^- during the photomineralisation of 4-CP at TiO_2 films in a 1.0×10^{-3} mol dm^{-3} 4-CP solution in the presence of 0.1 M $NaClO_4$ as supporting electrolyte under aerated conditions.

I_0/ q cm^{-2} s^{-1}	k'/ mol cm^{-2} s^{-1}
2.13×10^{16}	3.1×10^{-10}
1.07×10^{16}	1.5×10^{-10}
5.33×10^{15}	6.8×10^{-11}
2.66×10^{15}	3.4×10^{-11}

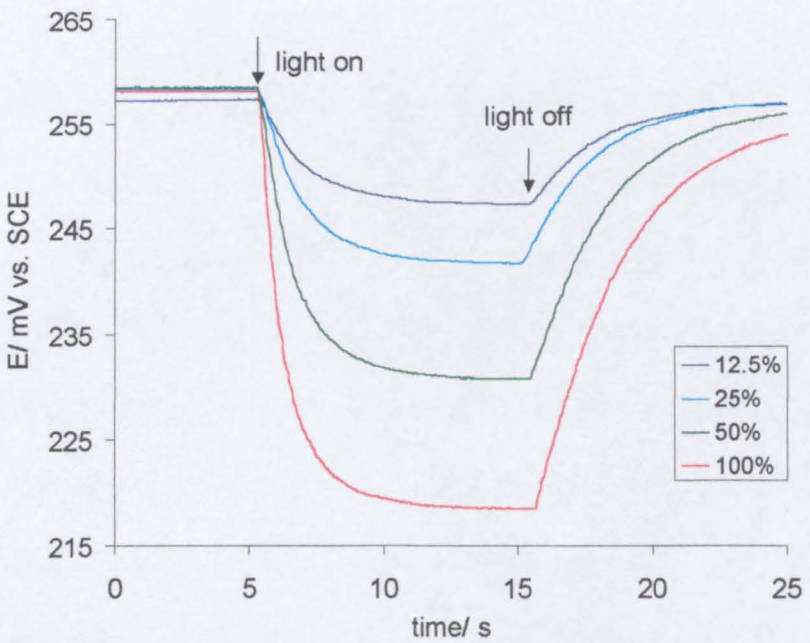

Figure 5.9 Potential response of the Ag/AgCl UME, positioned 17.4 μm away from the TiO_2 film, during the photomineralisation of an aerated 1.0×10^{-3} mol dm^{-3} 4-CP solution in the presence of 0.1 M $NaClO_4$ as supporting electrolyte, at four light intensities.

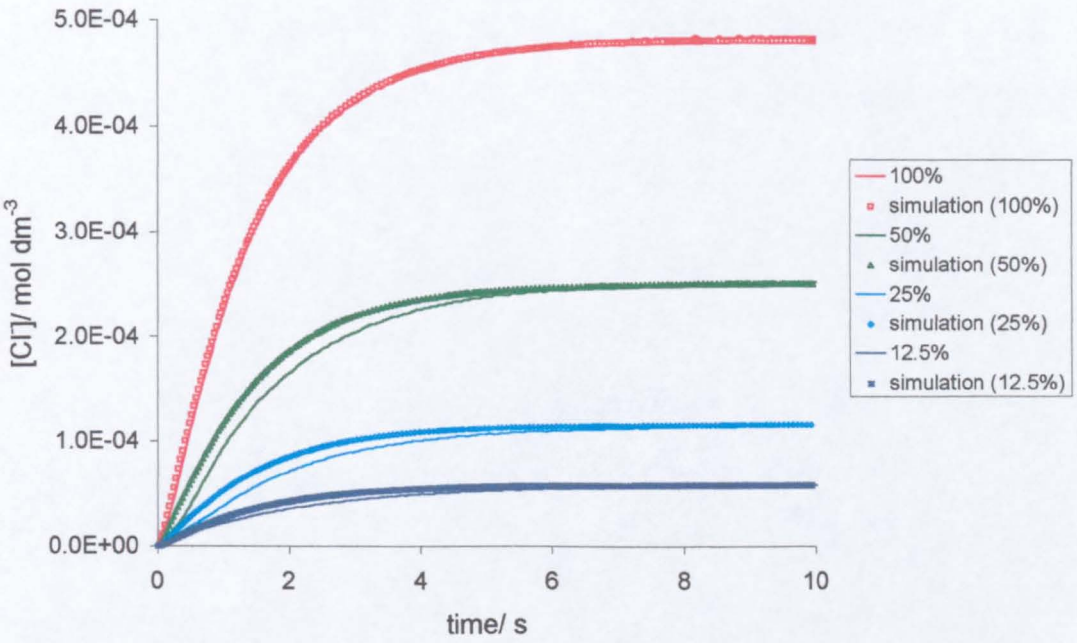

Figure 5.10 Photogenerated [Cl^-] detected at the Ag/AgCl UME during the photomineralisation of an aerated 1.0×10^{-3} mol dm^{-3} 4-CP solution (with 0.1 M $NaClO_4$) compared with the best fit theoretical simulations for the Langmuir-Hinshelwood model at four light intensities.

5.3.4.2 In an Oxygenated 4-CP Solution

The presence of higher levels of oxygen speeds up the surface photomineralisation process by scavenging the photogenerated electrons at the TiO_2 surface, producing superoxide radical anions.[2,20] Accordingly, the photomineralisation kinetics were also examined under conditions where the level of oxygen in a 1.0×10^{-3} mol dm^{-3} 4-CP solution (in the presence of 0.1 M $NaClO_4$) was increased from aerated to saturation with 1 atm. O_2. Figure 5.11 shows the potential response of the Ag/AgCl UME, positioned 17.4 μm away from the TiO_2 film, during the photomineralisation of the oxygenated 4-CP solution, at the four light intensities. The corresponding photogenerated [Cl^-] is shown in Figure 5.12. Also shown in Figure 5.12 are the best fits to the

experimental results, which were analysed using the Langmuir-Hinshelwood model described previously. The values of the initial rate of 4-CP photomineralisation are shown in Table 5.2. The model simulation does not provide an accurate description of the initial few seconds after the light has been switched on, but good agreement under steady-state conditions is achieved. This slight deviation was less pronounced for the aerated solutions, where the reaction rate was lower. When the reaction is faster, as in the case of oxygenated conditions, diffusional effects in solution, and possibly in the film, may lead to a broadening of the transient response, manifested as a longer lag time in the transient before a steady-state is attained.

As for the aerated solutions, the estimated rate constants are closely proportional to the incident light intensity. Comparing Figures 5.12 and 5.10, it can be seen that increasing the concentration of oxygen in solution by a factor of five increases the rate constants values by a factor of *ca.* 1.3 to 1.9.

Table 5.2 Values of the rate constants, estimated using a Langmuir-Hinshelwood model, for the formation of Cl^- during the photomineralisation of 4-CP at TiO_2 films in a 1.0×10^{-3} mol dm^{-3} 4-CP solution in the presence of 0.1 M $NaClO_4$ as supporting electrolyte under oxygenated conditions.

I_0/ q cm^{-2} s^{-1}	k'/ mol cm^{-2} s^{-1}
2.13×10^{16}	4.0×10^{-10}
1.07×10^{16}	2.2×10^{-10}
5.33×10^{15}	1.2×10^{-10}
2.66×10^{15}	6.4×10^{-11}

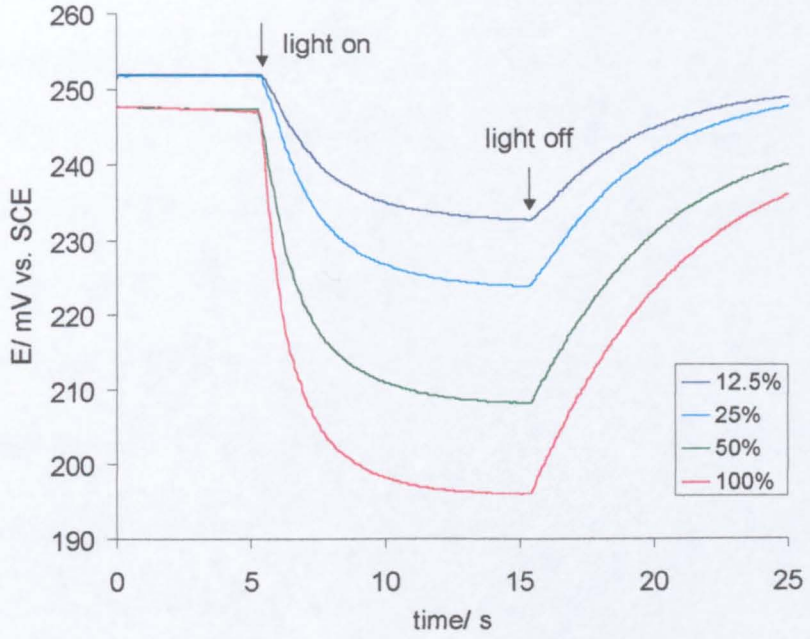

Figure 5.11 Potential response of the Ag/AgCl UME, positioned 17.4 μm away from the TiO_2 film, during the photomineralisation of an oxygenated 1.0×10^{-3} mol dm^{-3} 4-CP solution in the presence of 0.1 M $NaClO_4$ as supporting electrolyte, at four light intensities.

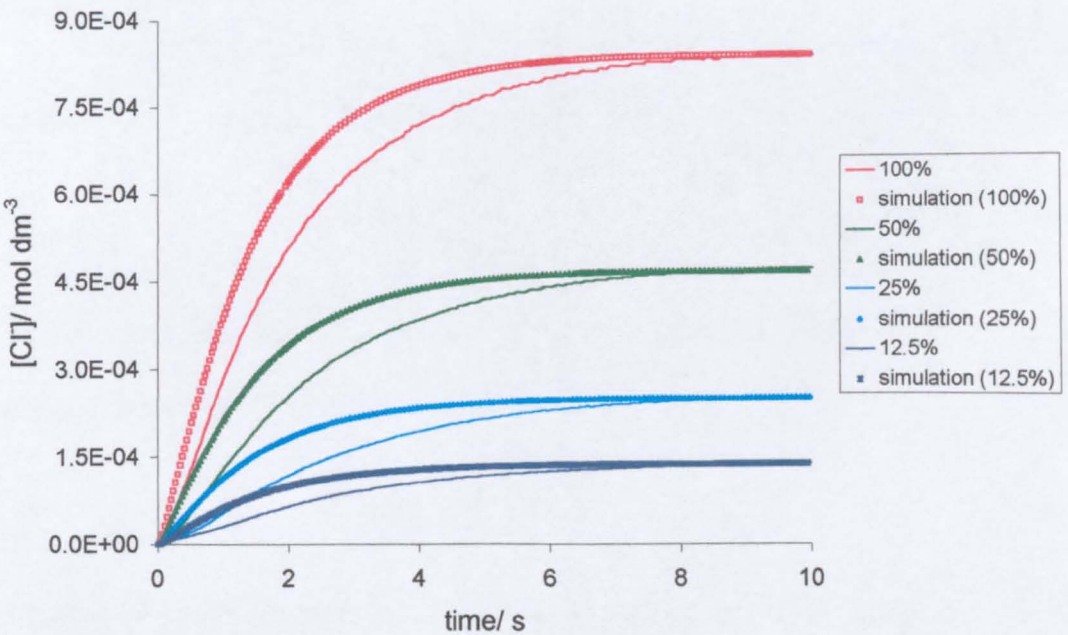

Figure 5.12 Photogenerated [Cl^-] detected at the Ag/AgCl UME during the photomineralisation of an oxygenated 1.0×10^{-3} mol dm^{-3} 4-CP solution (with 0.1 M $NaClO_4$) compared with the best fit theoretical simulations for the Langmuir-Hinshelwood model at four light intensities.

5.3.5 Effect of [4-CP] on the Kinetics of 4-CP Photomineralisation

5.3.5.1 In Aerated 4-CP Solutions

The influence of [4-CP] on the photomineralisation rate was investigated by using four different 4-CP solutions (with 0.1 M $NaClO_4$) with the following concentrations: 1.0×10^{-3} mol dm^{-3}, 5.0×10^{-4} mol dm^{-3}, 2.0×10^{-4} mol dm^{-3} and 1.0×10^{-4} mol dm^{-3}. The potential response of the Ag/AgCl UME, positioned 16.2 μm away from the TiO_2 film, during the photomineralisation of the aerated 4-CP solutions at the maximum light intensity of 2.13×10^{16} q cm^{-2} s^{-1}, is shown in Figure 5.13. The photogenerated [Cl^-] is compared alongside the best fits for the Langmuir-Hinshelwood model in Figure 5.14. The values of the initial rate of photomineralisation, for the different 4-CP concentrations, are shown in Table 5.3. There is a good agreement between the experimental data and the model simulation.

The model employs a Langmuir-Hinshelwood type kinetic equation for O_2, so the rate of photomineralisation is given by:

$$Rate = \frac{k' K_{O_2}[O_2]}{1 + K_{O_2}[O_2]} \tag{5.8}$$

where k' is the rate constant determined in the simulation, which has a dependence on [4-CP] given by the following equation:

$$k' = \frac{k'' K_{4\text{-CP}}[4\text{-CP}]}{1 + K_{4\text{-CP}}[4\text{-CP}]} \tag{5.9}$$

where k'' is a rate constant which provides a measure of the intrinsic reactivity of the photoactivated TiO_2 surface with 4-CP, and $K_{4\text{-CP}}$ is the equilibrium adsorption constant of 4-CP at the TiO_2 surface. From equation (5.9) we can write,

$$\frac{1}{k'} = \frac{1}{k''K_{4\text{-CP}}[4\text{-CP}]} + \frac{1}{k''} \qquad (5.10)$$

A plot of $1/k'$ vs. 1/[4-CP], shown in Figure 5.15, yields k'' and $K_{4\text{-CP}}$. The values obtained for k'' and $K_{4\text{-CP}}$ are, respectively, 1.3×10^{-9} mol cm^{-2} s^{-1} and 7.7×10^{2} M^{-1}. The equilibrium adsorption constant is lower than that obtained by Mills *et al.*[14], 1.7×10^{3} M^{-1}, for a thin film system.

The model considers that there is enough 4-CP adsorbed at the TiO_2 surface to react with the photogenerated holes and does not account for diffusion of 4-CP into the tip-substrate gap. However, for the lower concentrations, mass transport of 4-CP into the gap might be an important parameter. The importance of mass transfer effects for dilute solutions was highlighted by Turchi and Ollis[17], and Ahmed *et al.*[16] have shown that mass transport is a key parameter in controlling photomineralisation rates, particularly with low substrate concentrations. An improvement to the model would be to consider diffusion of 4-CP into the tip-substrate gap.

Table 5.3 Values of the rate constants, estimated using a Langmuir-Hinshelwood model, for the formation of Cl^- during the photomineralisation of different 4-CP solutions at TiO_2 films under aerated conditions.

[4-CP]/ mol dm^{-3}	k'/ mol cm^{-2} s^{-1}
1.0×10^{-3}	5.9×10^{-10}
5.0×10^{-4}	3.3×10^{-10}
2.0×10^{-4}	1.8×10^{-10}
1.0×10^{-4}	9.2×10^{-11}

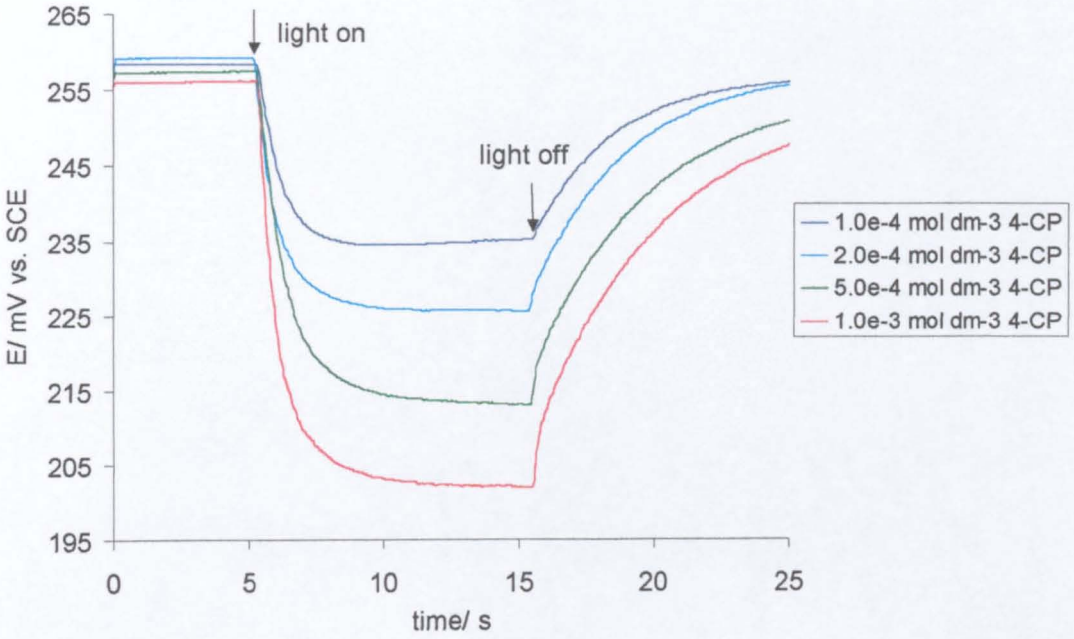

Figure 5.13 Potential response of the Ag/AgCl UME, positioned 16.2 μm away from the TiO_2 film, during the photomineralisation of aerated 4-CP solutions (with 0.1 M $NaClO_4$) at the light intensity of 2.13×10^{16} q cm^{-2} s^{-1}.

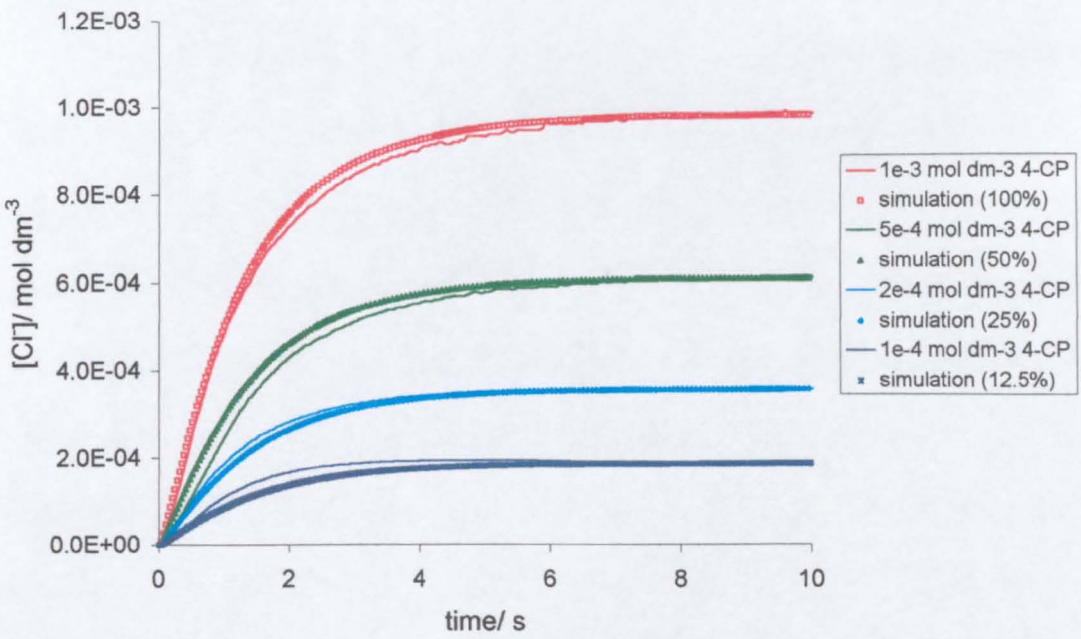

Figure 5.14 Photogenerated [Cl^-] detected at the Ag/AgCl UME during the photomineralisation of the aerated 4-CP solutions (with 0.1 M $NaClO_4$) compared with the best fit theoretical simulations for the Langmuir-Hinshelwood model.

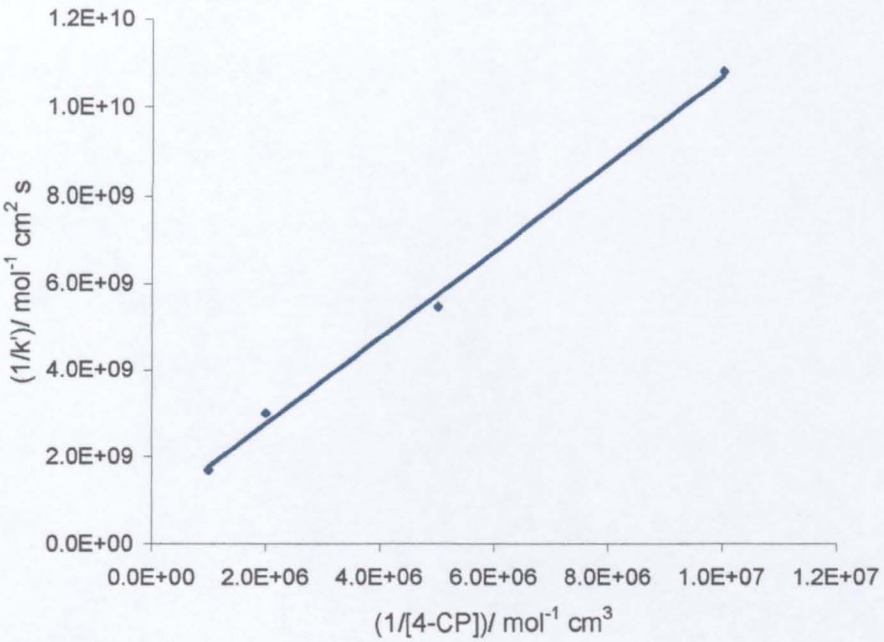

Figure 5.15 Reciprocal initial rate vs. reciprocal 4-CP concentration for the photomineralisation of 4-CP at a TiO_2 film (aerated conditions).

5.3.5.2 In Oxygenated 4-CP Solutions

The effect of [4-CP] on the photomineralisation rate was also investigated under oxygenated conditions. Figure 5.16 shows the potential response of the Ag/AgCl UME, positioned 16.2 μm away from the TiO_2 film, during the photomineralisation of the oxygenated 4-CP solutions at the maximum light intensity of 2.13×10^{16} q cm^{-2} s^{-1}. The photogenerated [Cl^-] and the best fit theoretical simulations for the Langmuir-Hinshelwood model are given in Figure 5.17. The values of the initial rate of photomineralisation, for the different 4-CP concentrations, are shown in Table 5.4. There is a good agreement between the best fit theoretical simulations and the experimental results. Comparing Tables 5.3 and 5.4 it can be seen that increasing the concentration of oxygen in solution from aerated conditions to saturation only slightly increases the rate constants values.

From the double reciprocal plot shown in Figure 5.18, the values 1.1×10^{-9} mol cm^{-2} s^{-1} and 9.9×10^{2} M^{-1} were obtained for k'' and $K_{4\text{-CP}}$, respectively.

For each solution, the [Cl^-] formed is bigger than the 4-CP concentration in that solution, particularly for the lower concentrations. This is consistent with the model and electrochemical measurements on the oxidation of 4-CP reported earlier in this chapter which point to a surface photomineralisation process of adsorbed 4-CP, where the equivalent surface concentration could be higher than in solution.

Table 5.4 Values of the rate constants, estimated using a Langmuir-Hinshelwood model, for the formation of Cl^- during the photomineralisation of different 4-CP solutions at TiO_2 films under oxygenated conditions.

[4-CP]/ mol dm^{-3}	k'/ mol cm^{-2} s^{-1}
1.0×10^{-3}	6.0×10^{-10}
5.0×10^{-4}	3.4×10^{-10}
2.0×10^{-4}	1.9×10^{-10}
1.0×10^{-4}	1.0×10^{-10}

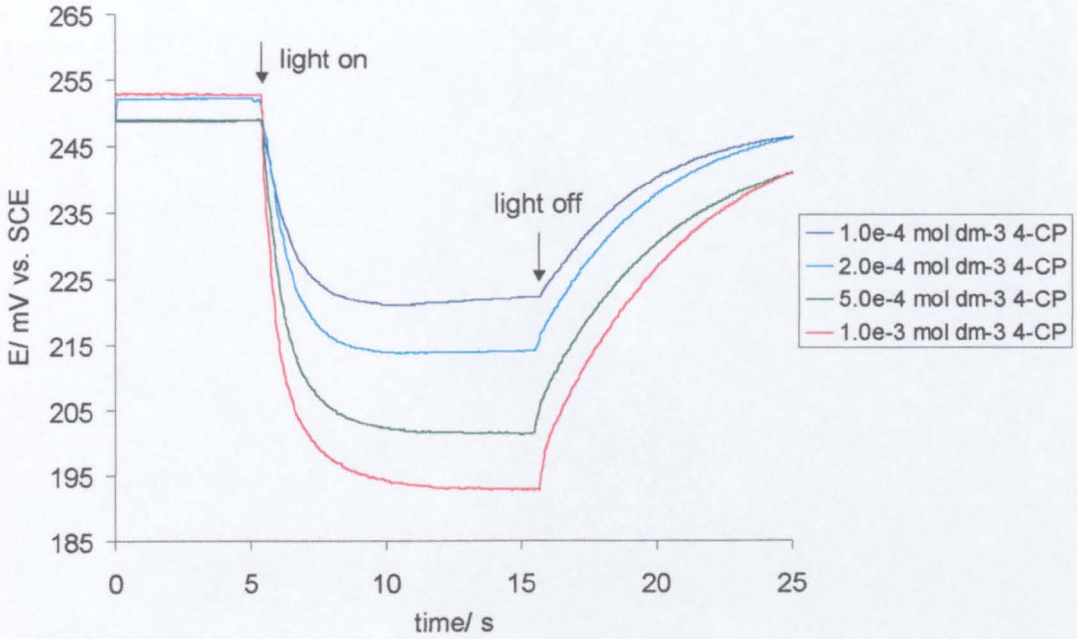

Figure 5.16 Potential response of the Ag/AgCl UME, positioned 16.2 μm away from the TiO_2 film, during the photomineralisation of oxygenated 4-CP solutions (with 0.1 M $NaClO_4$) at the light intensity of 2.13×10^{16} q cm^{-2} s^{-1}.

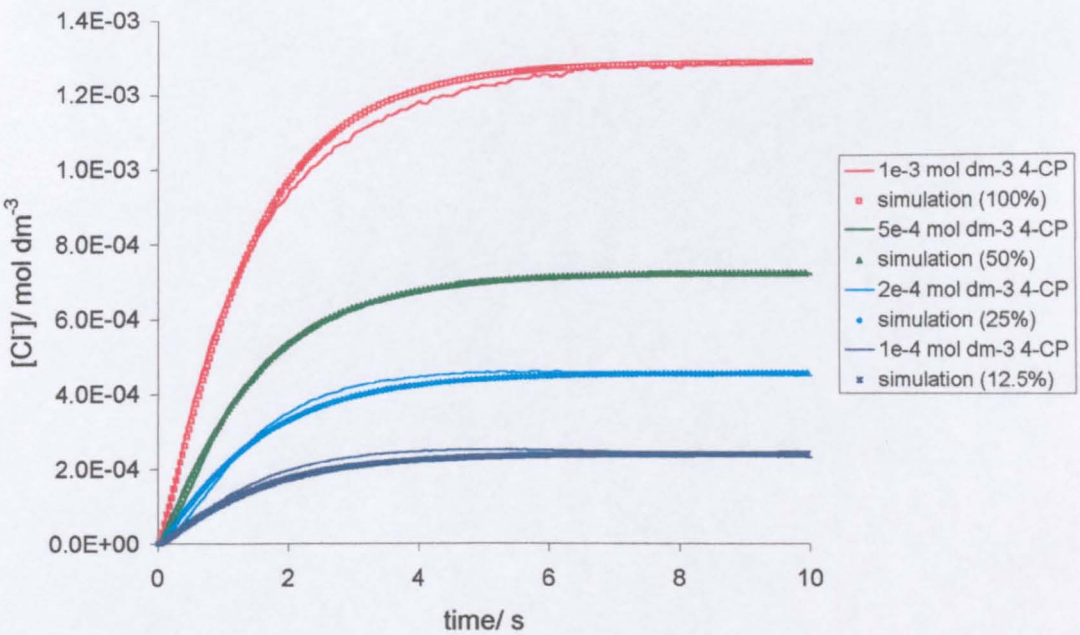

Figure 5.17 Photogenerated [Cl^-] detected at the Ag/AgCl UME during the photomineralisation of the oxygenated 4-CP solutions (with 0.1 M $NaClO_4$) compared with the best fit theoretical simulations for the Langmuir-Hinshelwood model.

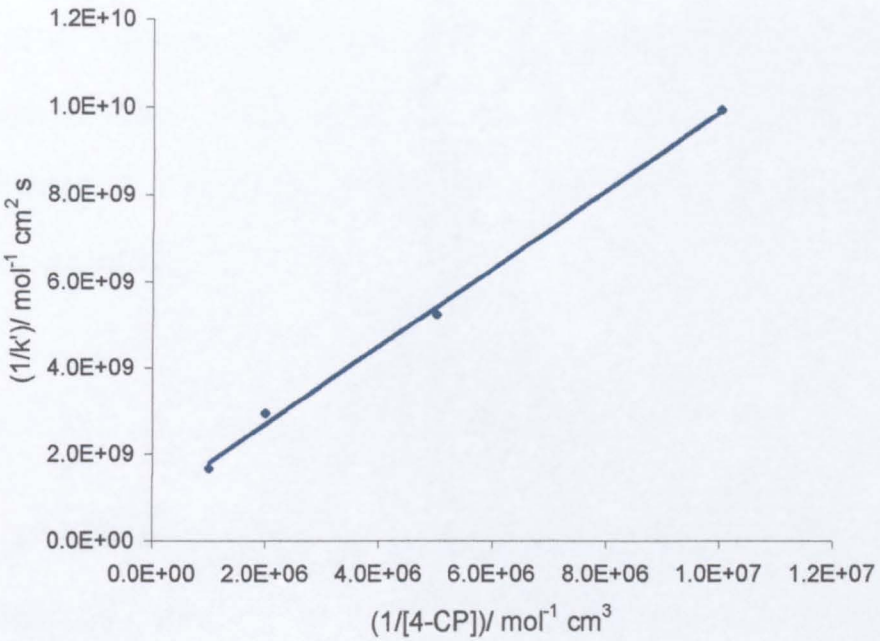

Figure 5.18 Reciprocal initial rate vs. reciprocal 4-CP concentration for the photomineralisation of 4-CP at a TiO_2 film (oxygenated conditions).

5.3.6 Estimating the Quantum Efficiency

The quantum efficiency is an important parameter in the photomineralisation process and it is worth estimating its value. The quantum efficiency can be calculated *via* the following expression related to the Langmuir-Hinshelwood model:

$$\phi = \frac{k'\left(\frac{K_{O_2}[O_2]^*}{1+K_{O_2}[O_2]^*}\right)N_A}{I_0} \qquad (5.11)$$

where k' is the rate constant for the photomineralisation of 4-CP, K_{O2} is the equilibrium adsorption constant for oxygen (9.63×10^6 mol^{-1} cm^3),[22] $[O_2]^*$ is the bulk concentration of oxygen, N_A is the Avogadro's number and I_0 is the light flux intensity in q cm^{-2} s^{-1}.

Tables 5.5 and 5.6 show the estimated quantum yields for the photomineralisation of 4-CP at different light intensities and for different 4-CP concentrations, respectively. The quantum yield, and hence the efficiency of the photocatalytic process, increases between 1.3 and 2.5 times when the level of oxygen was increased to saturated conditions with 1 atm. O_2. This is in reasonable agreement with the literature value of a 1.7 – fold enhancement of the rate under oxygen saturation compared to aerated conditions.[20]

Table 5.5 Estimated quantum yields for the photomineralisation of 4-CP at TiO_2 films in a 1.0×10^{-3} mol dm^{-3} 4-CP solution in the presence of 0.1 M $NaClO_4$ as supporting electrolyte under aerated and oxygenated conditions.

I_0 / q cm^{-2} s^{-1}	ϕ (aerated conditions)	ϕ (oxygenated conditions)
2.13×10^{16}	6.1×10^{-3}	0.011
1.07×10^{16}	6.0×10^{-3}	0.011
5.33×10^{15}	5.4×10^{-3}	0.012
2.66×10^{15}	5.4×10^{-3}	0.013

Table 5.6 Estimated quantum yields for the photomineralisation of 4-CP at TiO_2 films under aerated and oxygenated conditions at the light intensity of 2.13×10^{16} q cm^{-2} s^{-1}.

[4-CP] / mol dm^{-3}	ϕ (aerated conditions)	ϕ (oxygenated conditions)
1.0×10^{-3}	0.012	0.016
5.0×10^{-4}	6.6×10^{-3}	8.8×10^{-3}
2.0×10^{-4}	3.6×10^{-3}	5.0×10^{-3}
1.0×10^{-4}	1.8×10^{-3}	2.6×10^{-3}

5.4 Conclusions

SECM has been shown to be a successful new approach for quantitatively investigating the photomineralisation kinetics of a model organic pollutant, 4-CP, at supported TiO_2 films. A theoretical model, which employs a Langmuir-Hinshelwood type kinetic equation for O_2 and constant surface coverage of 4-CP, has been developed to interpret the kinetics of the photomineralisation process. This assumes that electron transfer to oxygen is rate-limiting and that the concentration of 4-CP does not fall to zero at the TiO_2 surface. The model simulation generally provided a good fit to the experimental data, although there are instances (higher reaction rate, low [4-CP]) when the model assumptions are not met experimentally. It has been shown that the photomineralisation rate is closely proportional to the light flux intensity and that increasing the concentration of oxygen in solution from aerated to saturated conditions only slightly enhances the photomineralisation rate.

It is also interesting to compare the rate of Cl^- formation in the photomineralisation process with the rate of oxygen consumption at the illuminated TiO_2 surface, under similar experimental conditions. Comparison of the rate constants for photomineralisation with the rate constants for oxygen reduction in 4-CP solutions shows that there is a direct correlation between the loss of oxygen and the formation of Cl^-. This close correlation strongly suggests that the flux matching ideas of Lewis,[23] in which the anodic (hole consumption) and cathodic (electron consumption) rates must balance, represents a good description of the photomineralisation process.

References

1. D. F. Ollis, *C. R. Acad. Sci. Paris, Série IIC, Chimie / Chemistry*, **2000**, 3, 405.

2. A. Mills and S. Le Hunte, *J. Photochem. Photobiol. A: Chem.*, **1997**, 108, 1 and references therein.

3. G. Al-Sayyed, J.-C. D'Oliveira and P. Pichat, *J. Photochem. Photobiol. A: Chem.*, **1991**, 58, 99.

4. A. Mills, S. Morris and R. Davis, *J. Photochem. Photobiol. A: Chem.*, **1993**, 70, 183.

5. A. Mills and S. Morris, *J. Photochem. Photobiol. A: Chem.*, **1993**, 71, 75.

6. J. Cunningham and P. Sedlak, *J. Photochem. Photobiol. A: Chem.*, **1994**, 77, 255.

7. J. Theurich, M. Linder and D. W. Bahnemann, *Langmuir*, **1996**, 12, 6368.

8. U. Stafford, K. A. Gray and P. V. Kamat, *J. Catal.*, **1997**, 167, 25.

9. R. W. Matthews, *Solar Energy*, **1987**, 38, 405.

10. R. W. Matthews, *J. Chem. Soc., Faraday Trans.*, **1989**, 85, 1291.

11. R. W. Matthews, *J. Catal.*, **1988**, 111, 264.

12. H. Al-Ekabi and N. Serpone, *J. Phys. Chem.*, **1988**, 92, 5726.

13. H. Al-Ekabi, N. Serpone, E. Pelizzetti, C. Minero, M. A. Fox and R. B. Draper, *Langmuir*, **1989**, 5, 250.

14. A. Mills and J. Wang, *J. Photochem. Photobiol. A: Chem.*, **1998**, 118, 53.

15. S. Ahmed, C. E. Jones, T. J. Kemp and P. R. Unwin, *Phys. Chem. Chem. Phys.*, **1999**, 1, 5229.

16. S. Ahmed, T. J. Kemp and P. R. Unwin, *J. Photochem. Photobiol. A: Chem.*, **2001**, 141, 69.

17. C. S. Turchi and D. F. Ollis, *J. Phys. Chem.*, **1988**, 92, 6852.

18. A. Mills and J. Wang, *Int. J. Res. Phys. Chem. Chem. Phys.*, **1999**, 213, 49.

19. T. J. Kemp, P. R. Unwin and L. Vincze, *J. Chem. Soc. Faraday Trans.*, **1995**, 91, 3893.

20. A. Mills, R. H. Davies and D. Worsley, *Chem. Soc. Rev.*, **1993**, 22, 417.

21. J. M. Kesselman, G. A. Shreve, M. R. Hoffmann and N. S. Lewis, *J. Phys. Chem.*, **1994**, 98, 13385.

22. L. Rideh, A. Wehrer, D. Ronze and A. Zoulalian, *Catalysis Today*, **1999**, 48, 357.

23. J. M. Kesselman, G. A. Shreve, M. R. Hoffmann and N. S. Lewis, *J. Phys. Chem.*, **1994**, 98, 13385.

CHAPTER 6

PHOTOELECTROCHEMICAL KINETICS AT THE TiO_2/AQUEOUS INTERFACE: THE METHYL VIOLOGEN – ACETATE SYSTEM

This chapter describes how SECM has been used to monitor photoelectrochemical kinetics at the TiO_2/aqueous interface using a well-known electron scavenger, methyl viologen. The TiO_2 film was in contact with a solution containing methyl viologen dication (MV^{2+}) as the redox mediator and sodium acetate as the hole scavenger. The chronoamperometric behaviour for MV^{2+} reduction was recorded at an Ag UME tip after stepping the light flux at the TiO_2 film on and off. Both the effect of MV^{2+} concentration and light intensity were investigated. The rate constants for the reduction process were obtained through a theoretical model based on zero-order kinetics allowing the rate dependence on $[MV^{2+}]$ to be determined. The substrate generation/ tip collection mode of the SECM was also used to detect the $MV^{\bullet+}$ radical cation generated at the substrate at the UME tip.

6.1 Introduction

The photoelectrochemical reduction of oxygen at illuminated TiO_2 films was investigated in chapter 4 and this chapter is concerned with the study of another electron scavenger, methyl viologen (1,1'-dimethyl-4,4'bipyridinium ion; MV^{2+}). The dynamics of interfacial electron transfer reactions in TiO_2[1,2,3,4,5] and CdS[5,6] colloids and in CdS films,[7] employing MV^{2+} as an electron acceptor, have been extensively studied. Grätzel and co-workers[5] investigated the dynamics of interfacial electron transfer reactions in colloidal TiO_2 and CdS particles using

laser photolysis techniques. They found that the rate of reaction of photogenerated electrons with MV^{2+} was strongly influenced by the MV^{2+} concentration and pH. The kinetics of this reaction were found to be controlled by the diffusion of MV^{2+} to the particle surface as well as the rate of interfacial electron transfer. The interfacial electron transfer step controlled the rate at lower pH when the overvoltage available to drive the reaction was small. At higher pH, mass transfer effects became increasingly important and determined the overall reaction rate.[2,3]

Using electrochemical techniques, Bard and co-workers[1] have demonstrated that markedly enhanced photocurrents could be obtained from illuminated TiO_2 suspensions when MV^{2+} was present in the suspension. This behaviour was consistent with electron trapping by MV^{2+}, which prevented electron-hole recombination.

Haram and Bard[7] have used the feedback mode of the SECM to study the kinetics of photoelectron transfer reactions at a CdS thin film. The CdS film was in contact with a solution containing methyl viologen radical cation ($MV^{\bullet+}$) as the redox mediator and triethanolamine as the hole scavenger. In the absence of illumination, SECM approach curves of $MV^{\bullet+}$ oxidation to MV^{2+} as the probe was translated towards CdS films showed negative feedback. This demonstrated that the substrate could not reduce tip generated MV^{2+}, *i.e.*, the film behaved as an insulator. However, upon illumination, positive feedback was obtained due to photoelectron reduction of MV^{2+} to $MV^{\bullet+}$ at the interface. Apparent pseudo-first-order rate constants for the photoelectron transfer reaction were estimated by fitting experimental approach curves to theory.

The aim of this chapter is to use SECM to determine the kinetics of methyl viologen reduction at a TiO_2 film. A theoretical model based on zero-order

kinetics was developed to determine the rate constants for the reduction process and the functionalised dependence on [MV^{2+}].

6.2 Theory

The usual initial conditions and boundary conditions have already been described in section 4.3.2. The following boundary condition applies to the TiO_2 surface:

$$z = d, \qquad 0 < r < r_g \qquad : D\frac{\partial c_{MV^{2+}}}{\partial z} = k \tag{6.1}$$

The tip reduces MV^{2+} at a transport-controlled rate. The problem was cast into dimensionless form and solved using ADIFDM. For a given tip-substrate separation, this allowed the calculation of the current-time behaviour following illumination with a given K value. The normalised rate constant, K, is given by the following expression:

$$K = \frac{ka}{Dc^*} \tag{6.2}$$

where k is the rate constant for the reduction of MV^{2+} (mol cm^{-2} s^{-1}), a is the radius of the UME (cm), D is the diffusion coefficient for MV^{2+} (cm^2 s^{-1}) and c^* is the bulk concentration of MV^{2+} (mol cm^{-3}). Thus, the rate constants for the reduction process could be calculated.

6.3 Experimental Results and Discussion

6.3.1 Methyl Viologen Voltammetry

Current-potential voltammograms for the reduction of MV^{2+} at a 25 μm diameter Ag UME were recorded away from the TiO_2 film in a deoxygenated

aqueous 1.0×10^{-3} mol dm^{-3} MV^{2+} solution in the presence of 1.0 M sodium acetate. The reduction of MV^{2+} proceeds according to the following reaction:

$$MV^{2+} + e^- \rightarrow MV^{\bullet+} \quad (6.3)$$

A typical voltammogram is shown in Figure 6.1. Voltammograms were also run with the UME tip brought close to the TiO_2 surface, *ca.* 25 μm, in the dark and with illumination. A typical response is shown in Figure 6.2. The voltammetry with illumination produced a smaller limiting current than the corresponding voltammogram in the dark. The steady-state response is due to the photoelectrochemical reduction of MV^{2+} at the illuminated TiO_2 surface. This causes a depletion of MV^{2+} concentration at, and near, the catalyst surface, resulting in a smaller current being detected at the UME. A schematic representation of this process is shown in Figure 6.3.

The MV^{2+} solution must be thoroughly deoxygenated, since oxygen reduction occurs at similar potentials and oxygen would also compete with MV^{2+} for scavenging electrons at the illuminated TiO_2 surface. Moreover, $MV^{\bullet+}$ reacts readily with oxygen. The role of acetate ion is rapid removal of photogenerated holes in an irreversible fashion. Its presence prevents "short circuiting" of the particles by MV^{2+}, *i.e.*, by the reaction $MV^{\bullet+} + h^+ \rightarrow MV^{2+}$. The pH of the solution was ~ 8, which was enough for the photoelectrochemical reduction of MV^{2+} at the illuminated TiO_2 surface to occur.[1] The redox potential for the MV^{2+}/ $MV^{\bullet+}$ couple, equivalent to an energy level, E_{redox}, is independent of pH. The energy of the photogenerated electrons is represented by the Fermi level energy, E_F. E_F will shift with respect to E_{redox} with changes in solution pH. When E_F is below E_{redox}, reduction of MV^{2+} by photogenerated electrons does not occur. As

E_F increases in energy above E_{redox} (*i.e.*, as the pH increases), the driving force or overpotential for the reduction increases.[2,3]

From the limiting current in bulk solution, the diffusion coefficient for MV^{2+} was determined as $D = 9.63\times10^{-6}$ cm^2 s^{-1} using equation 1.22.

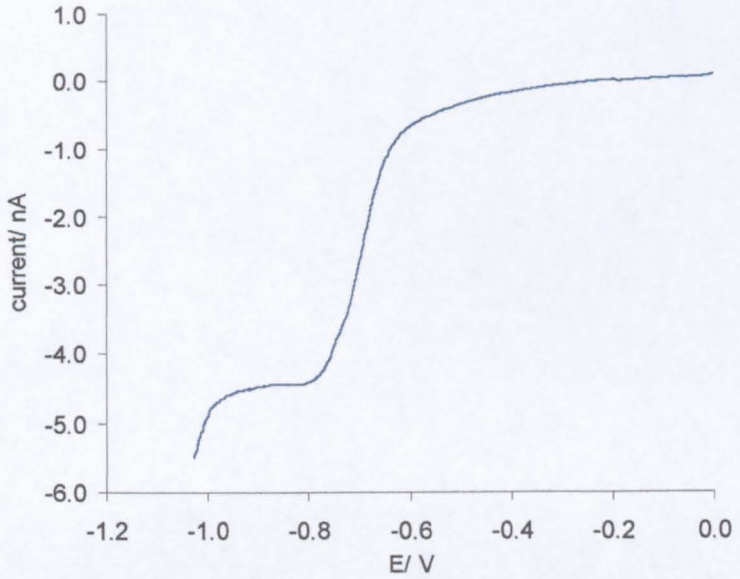

Figure 6.1 Bulk voltammogram for the reduction of 1.0×10^{-3} mol dm^{-3} MV^{2+} solution with 1.0 M sodium acetate at a 25 μm diameter Ag UME.

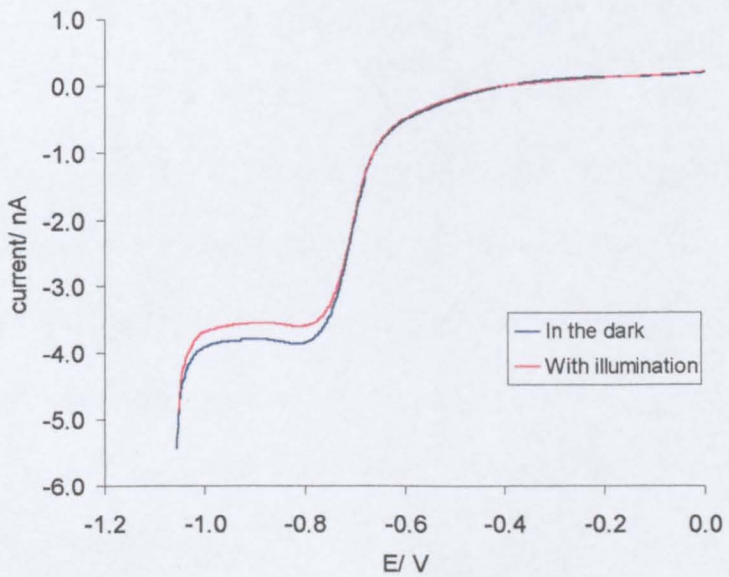

Figure 6.2 Voltammograms for the reduction of 1.0×10^{-3} mol dm^{-3} MV^{2+} solution with 1.0 M sodium acetate when the UME was brought close (~ 25 μm) to the TiO_2 surface, with the illumination on and off.

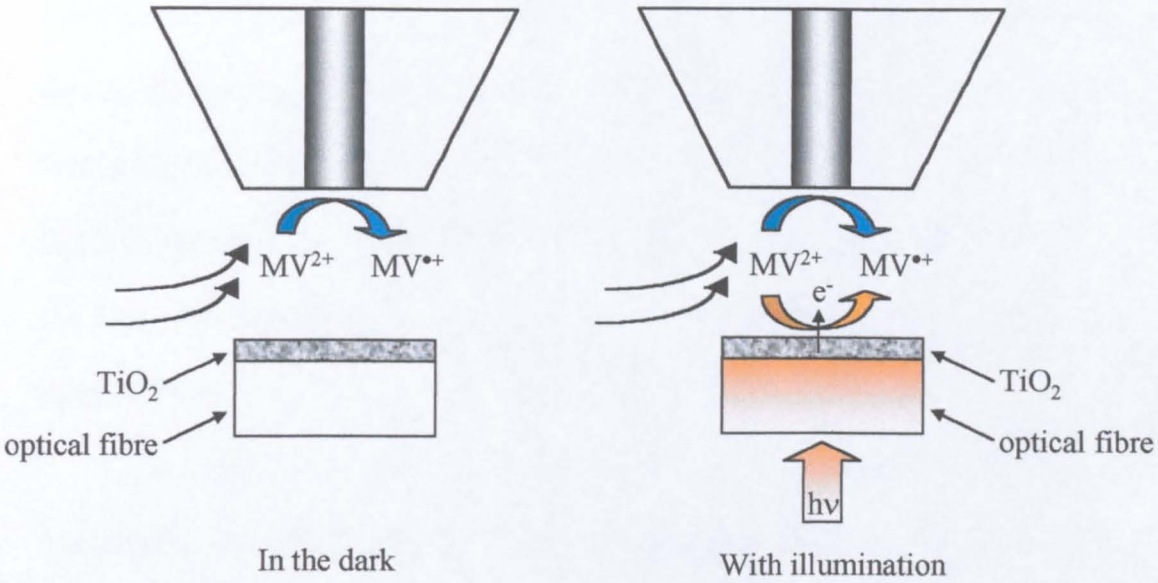

Figure 6.3 Schematic representation of the photoelectrochemical reduction of MV^{2+} at an illuminated TiO_2 surface. The UME was held at –0.9 V to effect the diffusion-limited reduction of MV^{2+}.

6.3.2 Chronoamperometry of MV^{2+} Reduction at an Illuminated TiO_2 Film

Phototransients for MV^{2+} reduction at a 25 μm diameter Ag UME were recorded in deoxygenated aqueous MV^{2+} solutions with 1.0 M sodium acetate with the following concentrations: 2.0×10^{-4} mol dm^{-3}, 3.0×10^{-4} mol dm^{-3}, 5.0×10^{-4} mol dm^{-3} and 1.0×10^{-3} mol dm^{-3}. The influence of the light flux intensity was investigated by using neutral density filters which only transmitted 50%, 25% and 12.5% of the incident light intensity. The transients for MV^{2+} reduction at the different light intensities and for the different concentrations are shown in Figures 6.4 to 6.7. These were obtained by establishing the steady-state diffusion-limited current for MV^{2+} reduction in the dark, with the probe close to the surface, and then switching on the light. The decrease in current when the light is switched on is due to the photoelectrochemical reduction of MV^{2+} at the TiO_2 surface, as explained above. The current changes are roughly proportional to the light intensity. All the transients were performed at tip-substrate distances of 24 ± 1

μm. However, the value of the dark current is lower than what would be expected for the dark hindered diffusion current corresponding to that distance. This means that before turning the illumination on there is already some reduction of MV^{2+} at the TiO_2 surface. This might be due to room illumination and/ or to the fact that the TiO_2 surface might be poised at a potential where it is acting like a partially conducting surface.

To analyse the results, simulations were run for different values of the normalised rate constant, K. For each of the simulations an $i/\ i(\infty)$ vs. time transient was obtained. The steady-state $i/\ i(\infty)$ values were then plotted against the corresponding log K values (Figure 6.8) and an equation was fitted to the curve. This allowed the determination of the K values corresponding to the $i/\ i(\infty)$ values for each concentration and for each light intensity. The $i/\ i(\infty)$ and K values are shown in Tables 6.1 and 6.2, respectively. The normalised rate constant K is given by equation 6.2.

It is apparent from Table 6.2 that the normalised rate constant obtained from the simulation is closely inversely proportional to $[MV^{2+}]$. In order to determine the rate constants, k, for the photoelectrochemical reduction of MV^{2+}, and to prove this functional dependence on concentration, plots of K vs. $1/\ [MV^{2+}]$ were constructed for each light intensity and are shown in Figure 6.9. The slope of each line allowed the rate constants k for the different light intensities to be calculated, and these are shown in Table 6.3. The data shows that the reaction proceeds quite readily in the dark and that illumination only has a small effect on promoting the reaction to occur faster. These rate constants are the same order of magnitude as the ones for oxygen reduction in a 4-CP solution (for K_{O2} = 9.63×10^{6} mol^{-1} cm^{3}) and an order of magnitude lower than the ones in the

presence of triethanolamine (for the same K_{O2}), although a report in the literature shows that interfacial electron transfer from CdS to oxygen is a slow process compared with electron transfer to MV^{2+}.[6]

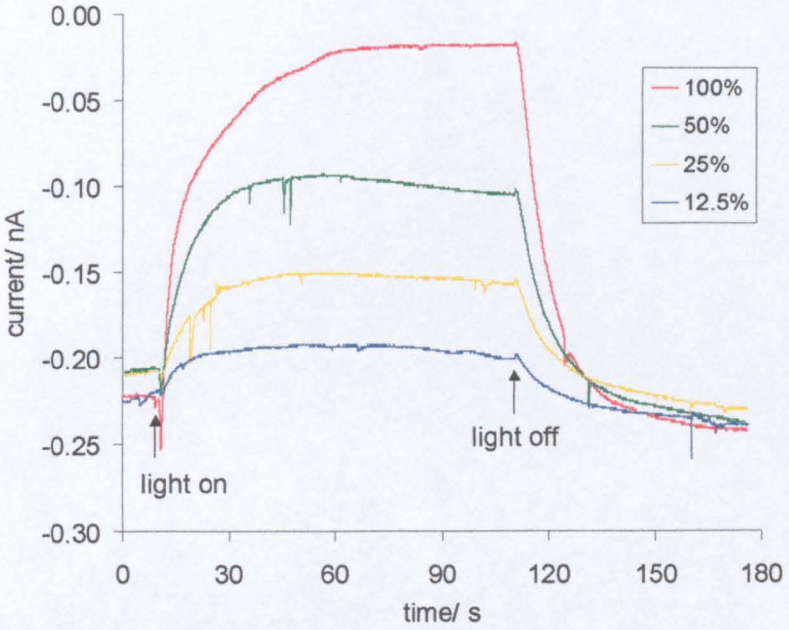

Figure 6.4 Phototransient responses at the Ag UME for the reduction of MV^{2+} in an aqueous deoxygenated 2.0×10^{-4} mol dm^{-3} MV^{2+} solution with 1.0 M sodium acetate. The tip-substrate distance was 24 ± 1 μm.

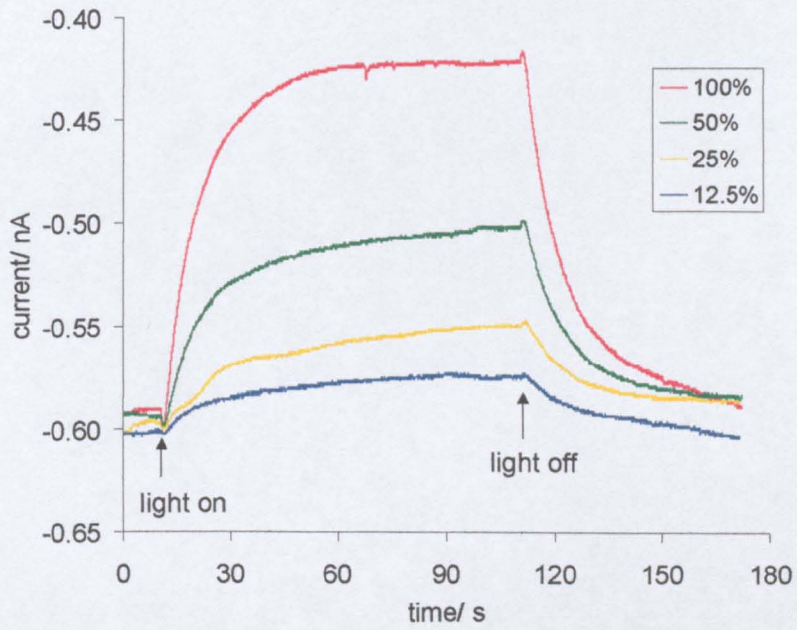

Figure 6.5 Phototransient responses at the Ag UME for the reduction of MV^{2+} in an aqueous deoxygenated 3.0×10^{-4} mol dm^{-3} MV^{2+} solution with 1.0 M sodium acetate. The tip-substrate distance was 24 ± 1 μm.

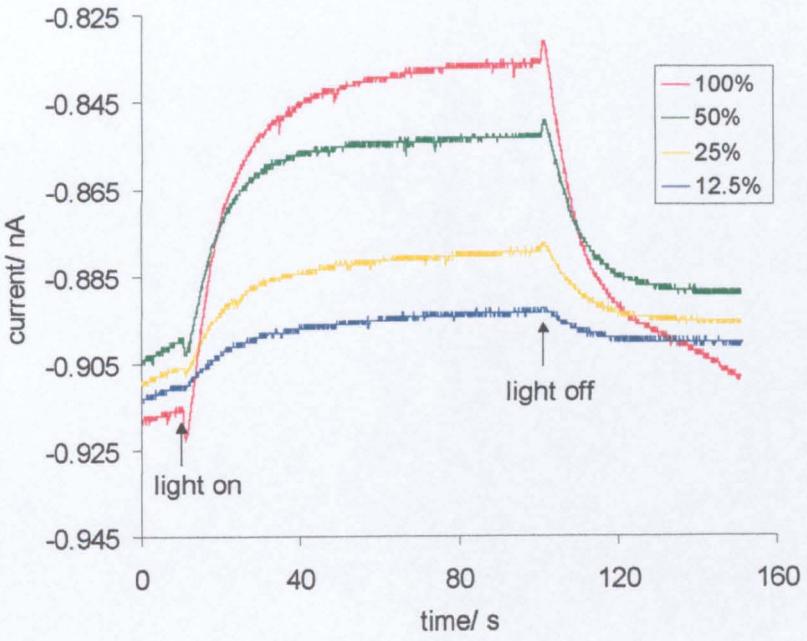

Figure 6.6 Phototransient responses at the Ag UME for the reduction of MV^{2+} in an aqueous deoxygenated 5.0×10^{-4} mol dm^{-3} MV^{2+} solution with 1.0 M sodium acetate. The tip-substrate distance was 24 ± 1 μm.

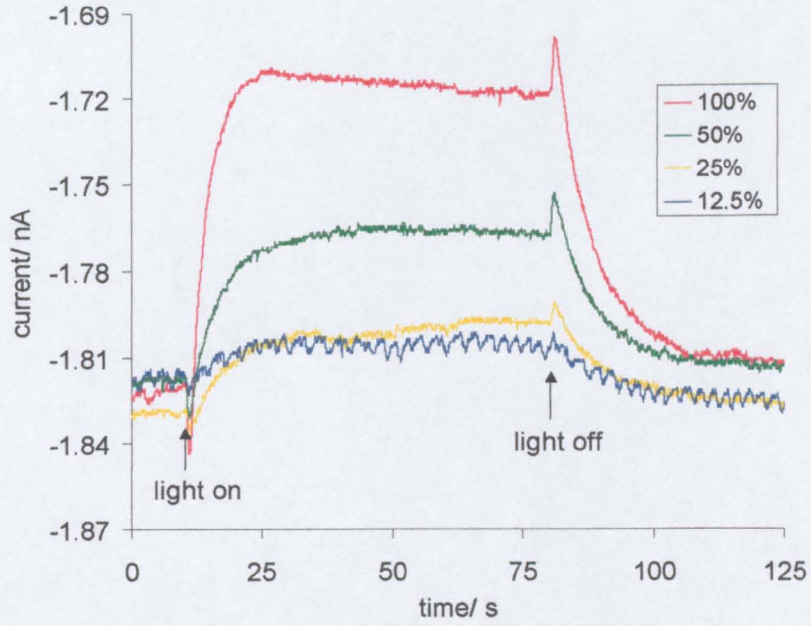

Figure 6.7 Phototransient responses at the Ag UME for the reduction of MV^{2+} in an aqueous deoxygenated 1.0×10^{-3} mol dm^{-3} MV^{2+} solution with 1.0 M sodium acetate. The tip-substrate distance was 24 ± 1 μm.

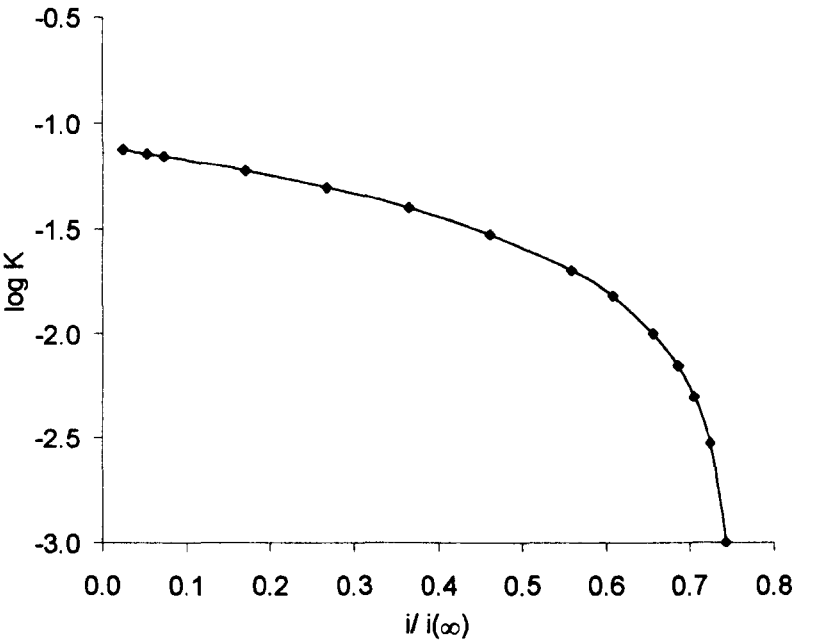

Figure 6.8 Plot of log K vs. $i/\ i(\infty)$ steady-state values obtained from a zero-order kinetics simulation, for $d = 24$ μm.

Table 6.1 Steady-state $i/\ i(\infty)$ values for the different MV^{2+} concentrations in the dark and at the different light intensities.

$[MV^{2+}]$ mol dm^{-3}	$i/\ i(\infty)$ dark	$i/\ i(\infty)$ 12.5%	$i/\ i(\infty)$ 25%	$i/\ i(\infty)$ 50%	$i/\ i(\infty)$ 100%
2.0×10^{-4}	0.145	0.130	0.101	0.0677	0.0103
3.0×10^{-4}	0.318	0.309	0.296	0.270	0.227
5.0×10^{-4}	0.394	0.384	0.378	0.367	0.360
1.0×10^{-3}	0.612	0.608	0.605	0.595	0.578

Table 6.2 Normalised rate constant values for the different MV^{2+} concentrations in the dark and at the different light intensities.

$[MV^{2+}]$ mol dm^{-3}	*K* dark	*K* 12.5%	*K* 25%	*K* 50%	*K* 100%
2.0×10^{-4}	0.0627	0.0638	0.0661	0.0702	0.0764
3.0×10^{-4}	0.0451	0.0459	0.0470	0.0494	0.0538
5.0×10^{-4}	0.0371	0.0383	0.0390	0.0402	0.0409
1.0×10^{-3}	0.0144	0.0149	0.0152	0.0163	0.0183

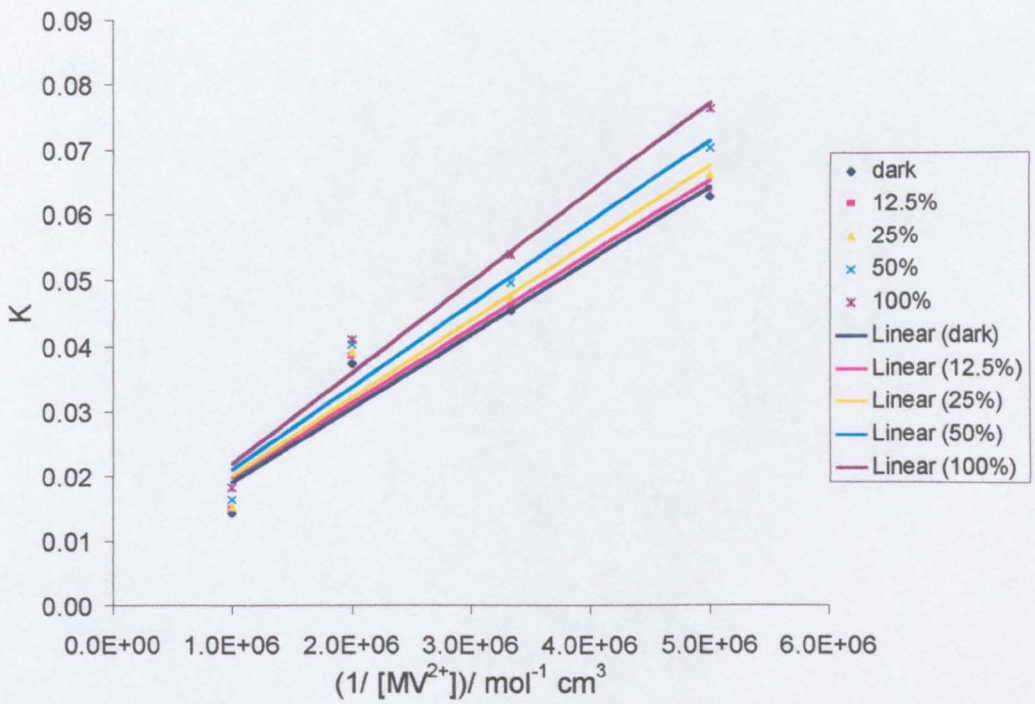

Figure 6.9 Plot of *K* vs. 1/ $[MV^{2+}]$ for the different light intensities and in the dark.

Table 6.3 Rate constants for the photoelectrochemical reduction of MV^{2+} in the dark and for the different light intensities.

I_0 (q cm^{-2} s^{-1})	k (mol cm^{-2} s^{-1})
Dark	8.65×10^{-11}
2.24×10^{15} (12.5%)	8.73×10^{-11}
4.48×10^{15} (25%)	9.11×10^{-11}
8.95×10^{15} (50%)	9.71×10^{-11}
1.79×10^{16} (100%)	1.07×10^{-10}

6.3.3 Estimating the Quantum Efficiency

The quantum efficiency for the photoelectrochemical reduction of MV^{2+} at TiO_2 films can be estimated from the following expression related to the zero-order kinetics model:

$$\phi = \frac{kN_A}{I_0} \tag{6.4}$$

where k is the rate constant for the photoelectrochemical reduction of MV^{2+}, N_A is the Avogadro's number and I_0 is the light flux intensity.

Table 6.4 shows the estimated quantum yields for the photoelectrochemical reduction of MV^{2+}. It was found that there was an increase in the quantum efficiency with a decrease in the light flux intensity. This

behaviour was also observed for the photoelectrochemical reduction of oxygen at TiO_2 films presented in chapter 4.

Table 6.4 Estimated quantum yields, related to the zero-order kinetics model, for the photoelectrochemical reduction of MV^{2+} at TiO_2 films.

I_0 (q cm^{-2} s^{-1})	ϕ
1.79×10^{16}	3.60×10^{-3}
8.95×10^{15}	6.53×10^{-3}
4.48×10^{15}	1.22×10^{-2}
2.24×10^{15}	2.35×10^{-2}

6.3.4 Substrate Generation/ Tip Collection Experiments

When monitoring the photoelectrochemical reduction of MV^{2+} at the TiO_2 film, the UME was held at – 0.9 V to effect the diffusion-limited reduction of MV^{2+}. However, by holding the UME at –0.2 V it should be possible to collect the $MV^{\bullet+}$ radical cation that is being generated at the illuminated TiO_2 surface. A schematic of this process is shown in Figure 6.10. Holding the tip at –0.2 V, transients were recorded in deoxygenated aqueous MV^{2+} solutions (2.0×10^{-4} mol dm^{-3}, 3.0×10^{-4} mol dm^{-3}, 5.0×10^{-4} mol dm^{-3} and 1.0×10^{-3} mol dm^{-3}) with 1.0 M sodium acetate. The transients obtained are shown in Figures 6.11 to 6.14. It was possible to detect the formation of $MV^{\bullet+}$, however, it took from 25 s to up to 100

s, after the illumination had been switched on, to start getting a response. Also, for the lower light intensities, $MV^{\bullet+}$ could not be detected at the UME. The solutions were thoroughly deoxygenated in the electrochemical cell, but since the experiments were not performed in a glove box, there is the possibility that oxygen might diffuse into the solution during the time course of a measurement. When oxygen is present it will compete with MV^{2+} for the photogenerated electrons and will also be reduced by any $MV^{\bullet+}$ that is formed. It has been shown in the literature that the presence of oxygen prevents the detection of $MV^{\bullet+}$ at a collector electrode (by being reduced by $MV^{\bullet+}$).[1] The presence of some residual oxygen in solution might explain the low collection current for $MV^{\bullet+}$ at the UME.

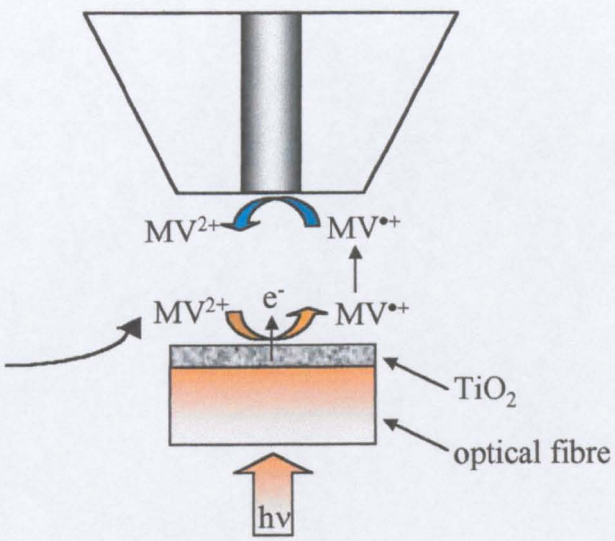

Figure 6.10 Schematic representation of the photogeneration of $MV^{\bullet+}$ at the TiO_2 surface and its collection at the UME. The electrode was held at –0.2 V to oxidise $MV^{\bullet+}$.

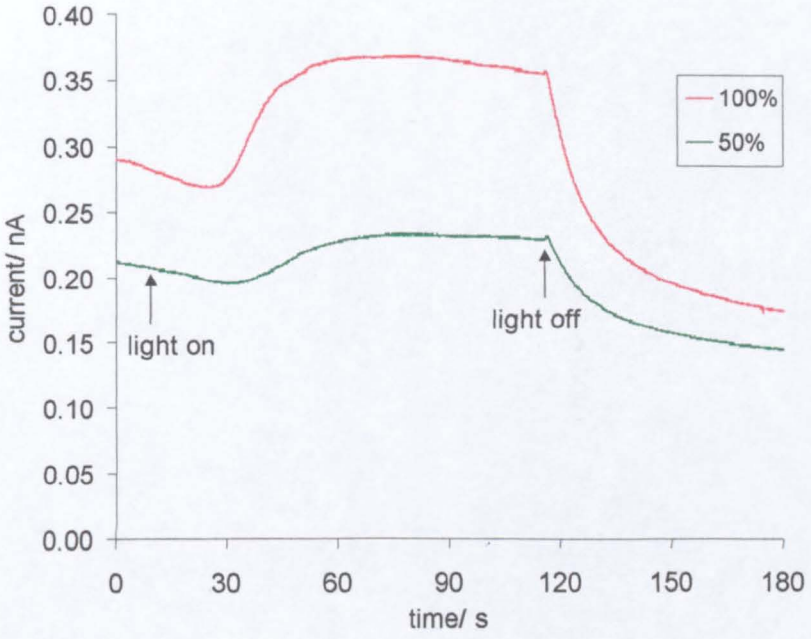

Figure 6.11 Phototransient responses for the collection of $MV^{\bullet+}$ at a Ag UME in an aqueous deoxygenated 2.0×10^{-4} mol dm^{-3} MV^{2+} solution with 1.0 M sodium acetate. The tip-substrate distance was 24 ± 1 μm.

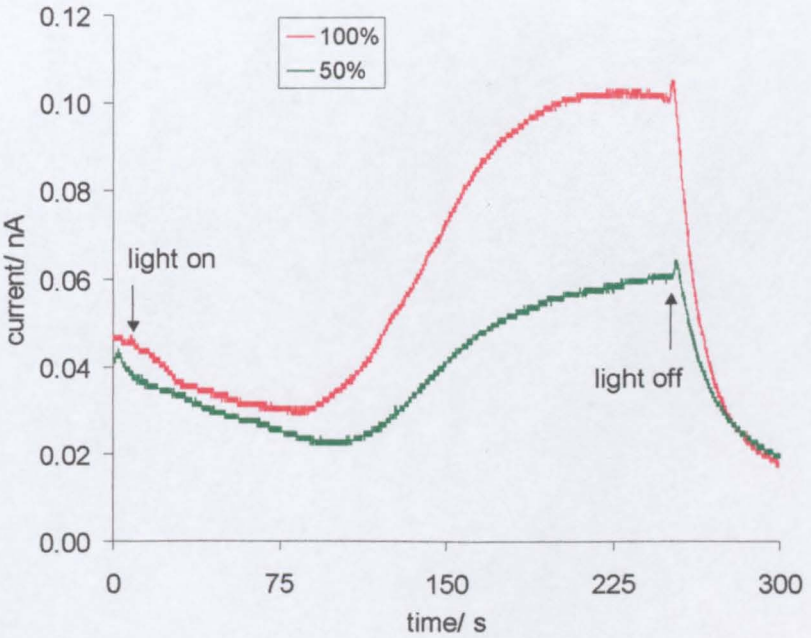

Figure 6.12 Phototransient responses for the collection of $MV^{\bullet+}$ at a Ag UME in an aqueous deoxygenated 3.0×10^{-4} mol dm^{-3} MV^{2+} solution with 1.0 M sodium acetate. The tip-substrate distance was 24 ± 1 μm.

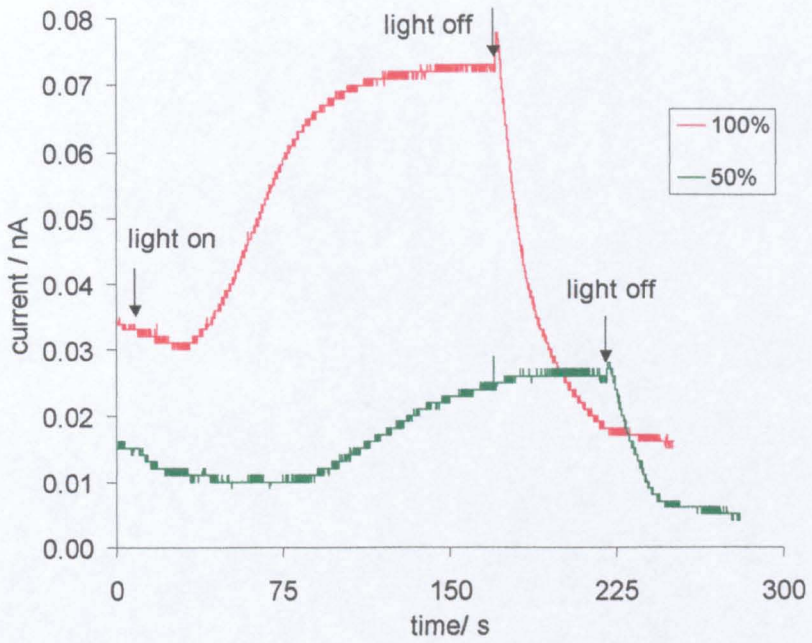

Figure 6.13 Phototransient responses for the collection of $MV^{\bullet+}$ at a Ag UME in an aqueous deoxygenated 5.0×10^{-4} mol dm^{-3} MV^{2+} solution with 1.0 M sodium acetate. The tip-substrate distance was 24 ± 1 μm.

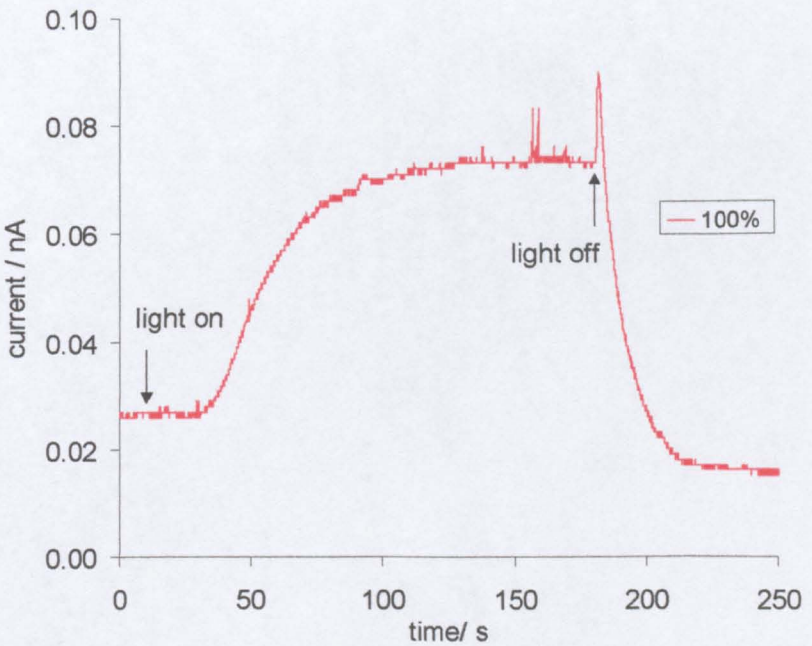

Figure 6.14 Phototransient responses for the collection of $MV^{\bullet+}$ at a Ag UME in an aqueous deoxygenated 1.0×10^{-3} mol dm^{-3} MV^{2+} solution with 1.0 M sodium acetate. The tip-substrate distance was 24 ± 1 μm.

6.4 Conclusions

SECM has been used to monitor the photoelectrochemical reduction of MV^{2+} at a TiO_2 film. The rate constants for the reduction process were determined using a theoretical model based on zero-order kinetics. The values of the rate constants obtained are comparable to those determined for oxygen reduction. It was found that the rate constants were not proportional to the light intensity and that even in the dark the depletion of MV^{2+} at the TiO_2 surface occurred. This might be due to room illumination and/ or to the fact that the TiO_2 surface might be poised at a potential to promote this reaction.

The substrate generation/ tip collection mode of the SECM was also used to detect the $MV^{\bullet+}$ radical cation at the UME tip. The collection currents for $MV^{\bullet+}$ at the UME were low, which might be explained by the presence of some residual oxygen in solution.

Overall, these initial studies of a reversible redox system illustrate the possibility of expanding significantly the range of species that might be detected using the SECM approaches outlined in this chapter, and throughout the thesis.

References

1. M. D. Ward, J. R. White and A. J. Bard, *J. Am. Chem. Soc.*, **1983**, 105, 27.

2. J. Moser and M. Grätzel, *J. Am. Chem. Soc.*, **1983**, 105, 6547.

3. M. Grätzel and A. J. Frank, *J. Phys. Chem.*, **1982**, 86, 2964.

4. G. T. Brown, J. R. Darwent and P. D. I. Fletcher, *J. Am. Chem. Soc.*, **1985**, 107, 6446.

5. D. Duonghong, J. Ramsden and M. Grätzel, *J. Am. Chem. Soc.*, **1982**, 104, 2977.

6. W. J. Albery, G. T. Brown, J. R. Darwent and E. Saievar-Iranizad, *J. Chem. Soc. Faraday Trans. 1*, **1985**, 81, 1999.

7. S. K. Haram and A. J. Bard, *J. Phys. Chem. B*, **2001**, 105, 8192.

CHAPTER 7

CONCLUSIONS

The work presented in this thesis has dealt with the development and application of SECM to investigate interfacial photoelectrochemical processes occurring at TiO_2 surfaces. SECM has been shown to be a successful new approach for quantitatively investigating the kinetics of interfacial photoprocesses at supported TiO_2 films. Since an accurate knowledge of the light flux initiating the photoprocess is required, a microelectrochemical actinometry approach was developed using the well-known liquid phase potassium ferrioxalate actinometer. The theoretical model developed in chapter 3 allowed the quantification of the light flux initiating the photoprocess.

In chapter 4 a new experimental approach to investigating the kinetics of the photoelectrochemical reduction of oxygen at UV-illuminated TiO_2 films was developed. The kinetics of the reduction process were interpreted through various theoretical models, but the Langmuir-Hinshelwood model provided the better agreement with experimental data. The experimental results demonstrated a significant depletion of the oxygen concentration at the illuminated TiO_2 surface. This observation provides a new insight into photomineralisation processes, showing the important role of oxygen in controlling the overall kinetics. It was also shown that adsorption is a major factor in the photoelectrochemical reduction of oxygen at TiO_2 surfaces.

The development of a potentiometric SECM approach in chapter 5 has allowed the investigation of the photomineralisation kinetics of a model organic pollutant, 4-CP, at supported TiO_2 films. A theoretical model, employing a

Langmuir-Hinshelwood type kinetic equation for O_2 and constant surface coverage of 4-CP, has been developed to interpret the kinetics of the photomineralisation process. It has been shown that the photomineralisation rate is closely proportional to the light flux intensity and that increasing the concentration of oxygen in solution from aerated to saturated conditions only slightly enhances the photomineralisation rate.

Comparison of the rate of Cl^- formation in the photomineralisation process with the rate of oxygen consumption at the illuminated TiO_2 surface, in 4-CP solutions, shows that there is a direct correlation between the loss of oxygen and the formation of Cl^-. This close correlation suggests that the photomineralisation process is ultimately an electrochemical process, in which the anodic (hole consumption) and cathodic (electron consumption) rates must balance.

In chapter 6, SECM has been used to monitor the photoelectrochemical transfer kinetics at the TiO_2/aqueous interface using a well-known electron scavenger, methyl viologen. The rate constants for the reduction process were determined using a theoretical model based on zero-order kinetics. The substrate generation/ tip collection mode of the SECM was also used to detect the $MV^{\bullet+}$ radical cation produced at the TiO_2 surface at the UME tip. In future work it would be interesting to examine the reactivity of other redox couples with different standard potentials.

Having shown that SECM is a powerful quantitative probe of interfacial photoelectrochemical processes, further developments could be explored, particularly:

(i) An optical micro-ring electrode,[1,2,3,4] in which the semiconductor surface is illuminated using an optical fibre surrounded by a ring UME, could be

employed to detect the reactants, intermediates and products of the photodegradation process. This would significantly enhance the temporal resolution, allowing the detection of short-lived photogenerated species. Electroactive species with lifetimes < 9×10^{-5} s have been detected with relatively large optical micro-ring electrodes (fibre-optic radius = 1.25×10^{-4} m, ring thickness = 600 nm),[1] suggesting that the study of photogenerated species with shorter lifetimes (10^{-6} s) may be feasible with smaller microelectrodes. Ring microelectrodes offer additional advantages over the more commonly used inlaid disc design, since the extra edge results in higher mass transport rate coefficients, leading to higher current densities, allowing the study of faster reactions.

(ii) Using sub-micrometer and nanometer-sized electrodes it may be possible to obtain specific information of heterogeneous photoelectrochemical reactions in even greater detail. The manufacture and use of electrodes with characteristic dimensions in the sub-micrometre to nanometre range[5,6,7] is becoming more widespread and common, however, there are no reports in the literature of its application to study heterogeneous photocatalysis. The advantages arising from these small-sized electrodes, including enhanced mass transport, reduced ohmic drop and double-layer charging effects, significantly enhance conventional UME behaviour. Also, it should be possible to achieve a significantly closer tip-substrate distance, which would be advantageous for the investigation of short-lived photogenerated species.

References

1. G. I. Pennarun, C. Boxall and D. O'Hare, *Analyst*, **1996**, 121, 1779.

2. N. Casillas, P. James and W. H. Smyrl, *J. Electrochem. Soc.*, **1995**, 142, L16.

3. P. James, N. Casillas and W. H. Smyrl, *J. Electrochem. Soc.*, **1996**, 143, 3853.

4. G. Shi, L. F. Garfias-Messias and W. H. Smyrl, *J. Electrochem. Soc.*, **1998**, 145, 2011.

5. R. M. Penner, M. J. Heben, T. L. Longin and N. S. Lewis, *Science*, **1990**, 250, 1118.

6. C. J. Slevin, N. J. Gray, J. V. Macpherson, M. A. Webb and P. R. Unwin, *Electrochem. Comm.*, **1999**, 1, 282.

7. N. J. Gray and P. R. Unwin, *Analyst*, **2000**, 125, 889.